MULTIPLEXED SENSING SYSTEM FOR BIOMOLECULES USING SURFACE ENHANCED RAMAN SPECTROSCOPY

A Dissertation

by

DANDAN TU

Submitted to the Graduate and Professional School of
Texas A&M University
in partial fulfillment of the requirements for the degree of

DOCTOR OF PHILOSOPHY

Chair of Committee,	Gerard L. Coté
Committee Members,	Michael McShane
	Kristen Maitland
	Jun Kameoka
Head of Department,	Michael McShane

December 2021

Major Subject: Biomedical Engineering

ABSTRACT

Myocardial infarction (MI) is a critical disease that affects a large population and has a high rate of mortality. Development of a point-of-care (POC) system for the detection of a biomarker panel composed of cardiac troponin I (cTnI), copeptin, and heart-type fatty acid-binding protein (h-FABP), is better than detection of a single biomarker because it can achieve an improved diagnosis of MI and a rapid rule-out of the non-MI patients in the field. Further, using a multiplex POC testing approach is more efficient for detecting a biomarker panel, because it requires a less total volume of sample, shorter analysis time, and lower total cost.

In this work, surface-enhanced Raman spectroscopy (SERS), a sensitive optical modality, was used as the transduction mechanism for the detection of the biomarkers for MI. Assays developed on paper-based microfluidic platforms were used to achieve the recognition of the biomarker and afforded the ability to be low cost and user-friendly. A silica shell nanoparticle was first developed to provide a stable and strong SERS signal. Using this SERS active particle, a single biomarker assay for the detection of cTnI was developed. To enhance the sensitivity, the paper-based microfluidic platform was improved by designing a localized dissolvable delay to tune the flow rate in the paper channel. In addition, a horizontal motion mechanical valve was designed to automatically finish the multiple steps in the assay. However, the sensitivity of the assay still needs to be improved. To overcome this, a new SERS active particle using a Raman reporter molecule (RRM) as a spacer to form a nanometer gap between a gold core and a gold shell

was developed. The nanometer gap largely enhanced the SERS signal; the gold shell protects the RRM and ensures a stable SERS signal. Using the improved SERS active particle, a multiplexed assay for detection of the biomarker panel (cTnI, copeptin, h-FABP) was developed. The signal from each biomarker on a single test line was resolved by using separate peaks from different RRMs in SERS active particles. The detection ranges of the assay successfully covered the clinically relevant range of the three biomarkers.

ACKNOWLEDGEMENTS

I would like to thank my committee chair, Dr. Coté, for his continuous support, great patience, and insightful guidance to my study at Texas A&M University. I would like to thank my committee members, Dr. McShane, Dr. Maitland, and Dr. Kameoka, for their support throughout the course of this research.

Thanks also go to current and past members of the Optical Bio-Sensing Lab for their encouragement and accompany during the years of study. In particular, I would like to thank Dr. Haley L. Marks for her passion and large help in teaching and guiding me when I first came to the lab. I would like to thank Dr. Javier T. Garza for the fruitful discussions on my research. I would like to thank Dr. Kokou Serge Dogbevi for providing suggestions about graduate school. I would like to thank Lydia E Colvin and Dr. Paul Gordon for their help and encouragement during my graduate life. Great thanks go to my parents for their encouragement and support to me. I also would like to thank Dexin Zhao for his patience and support to me.

I would like to thank Dr. Samuel Mabbott, Dr. Limei Tian, Dr. Paotai Lin, and Dr. Dino Di Carlo, and Dr. Alvin Yeh for their suggestions and help with my research and study. In addition, thanks also go to Dr. Kahlen Ouyang, Dr. Surreya Peterson, Dr. Yil-Hwan You, Dr. Sungyub Han, Dr. Dan Stoecklein, Megan Makela, Jacob Amos Hambalek, Ping Dong, Mehenur Sarwar, and Lin Tong, for their help to my graduate studies or my research. Thanks to all my friends, colleagues, the department faculty, and the staff for making my time at Texas A&M University a great experience.

CONTRIBUTORS AND FUNDING SOURCES

Contributors

This work was supervised by a dissertation committee consisting of Professor Gerard L. Coté (chair), Professor Michael McShane, Professor Kristen Maitland of the Department of Biomedical Engineering and Professor Jun Kameoka of the Department of Electrical Engineering.

All work for the dissertation was completed by the student, under the advisement of Professor Gerard L. Coté of the Department of Biomedical Engineering.

Funding Sources

This work was made possible in part by financial support of National Institutes of Health SBIR under Grant Number 1R43ES022303-01. This work was also made possible by financial support of National Science Foundation under Grant Number 1648451.

NOMENCLATURE

ESC	European Society of Cardiology
AHA	American Heart Association
ACC	American College of Cardiology
WHO	World Health Organization
NHANES	National Health and Nutrition Examination Survey
MI	Myocardial infarction
ACS/MI	Acute Coronary Syndrome/Myocardial Infarction
STEMI	ST-elevated Myocardial Infarction
NSTEMI	Non-ST-elevated Myocardial Infarction
NPV	Negative Predictive Value
ROC curve	Receiver Operating Characteristics Curve
URL	Upper Reference Limit
ECG	Electrocardiogram
PCI	Percutaneous Coronary Intervention
CABG	Coronary Artery Bypass Graft Surgery
AEDs	Automated External Defibrillators
CPR	Cardiopulmonary Resuscitation
POC	Point-of-care
POCT	Point-of-care Testing
xPOCT	Multiplexed Point-of-care Testing

AVP	Arginine Vasopressin
LDL	Low-density Lipoprotein
h-FABP	Heart-type Fatty Acid-binding Protein
cTnI	Cardiac Troponin I
cTnT	Cardiac Troponin T
CRP	C-reactive Protein
BNP	B-type Natriuretic Peptide
ELISA	Enzyme-linked Immunosorbent Assay
SERS	Surface-enhanced Raman Scattering
SERRS	Surface-enhanced Resonance Raman Scattering
EM	Electromagnetic
SPR	Surface Plasmon Resonance
LSPR	Localized Surface Plasmon Resonance
SELEX	Systematic Evolution of Ligands by Exponential Enrichment
μPAD	Microfluidic Paper-based Analytical Devices
TEM	Transmission Electron Microscopy
DLS	Dynamic Light Scattering
NTA	Nanosight Nanoparticle Tracking Analysis
SAM	Self-assembled Monolayer
LUMO	Lowest Unoccupied Molecular Orbital
HOMO	Highest Occupied Molecular Orbital
PBS	Phosphate-buffered Saline

Au	Gold
Ag	Silver
GeNP	Gap-enhanced Nanoparticle
BRIGHTs	Bilayered Raman-intense Gold Nanostructures with Hidden Tags
EDC-HCl	N-Ethyl-N'-(3-dimethylaminopropyl) Carbodiimide Hydrochloride
sulfo-NHS	N-Hydroxysulfosuccinimide Sodium Salt
BSA	Bovine Serum Albumin
PEG	Polyethylene Glycol
6-AHT	6-Amino-1-hexanethiol Hydrochloride
DNA	Deoxyribonucleic Acid
TEPSA	(3-Triethoxysilyl)propylsuccinic Anhydride
MPTMS	(3-Mercaptopropyl)trimethoxysilane
AuNPs	Gold Nanoparticles
$HAuCl_4 \cdot 3H_2O$	Gold (III) Chloride Trihydrate
CTAC	Cetyltrimethylammonium Chloride Solution
IgG	Immunoglobulin G
TEOS	Tetraethyl Orthosilicate
PVA	Poly(vinyl alcohol)
RRM	Raman Reporter Molecule
MGITC	Malachite Green Isothiocyanate
TFMBA	2,3,5,6-Tetrafluoro-4-mercaptobenzoic Acid
DTNB	5,5’-Dithiobis(2-nitrobenzoic acid)

MPAA	4-Mercaptophenylacetic Acid
BMBA	2-Bromo-4-mercaptobenzoic Acid
4-NTB	4-Nitrothiobenzoic Acid
PATP	p-Aminothiophenol
PNTP	p-Nitrothiophenol
4-MSTP	4-(Methylsulfanyl) Thiophenol
MMC	2,7-Mercapto-4-methylcoumarin
MMTAA	2-Mercapto-4-methyl-5-thiazoleacetic Acid
4-MBA	4-Mercaptobenzoic Acid
BDT	1,4-Benzenedithiol
BPDT	4,4'-Biphenyldithiol
TPDT	4,4'-Terphenyldithiol
ANOVA	Analysis of Variance
LOD	Limit of Detection
SD	Standard Deviation
RSD	Relative Standard Deviation
PDI	Polydispersity Index

TABLE OF CONTENTS

Page

LIST OF FIGURES

Page

LIST OF TABLES

Page

1. INTRODUCTION

1.1. Myocardial infarction

1.1.1. Mechanism

Atherosclerosis is a process related to plaque formation [1]. It tends to happen at the sites with low or oscillatory endothelial shear stress, located near branch points and along inner curvatures [2]. These sites usually show an adaptive intimal thickening with smooth muscle cell accumulation within the intima, which provides a soil for initial lesion development [2].

Generally, a plaque is formed by the following processes. In the beginning, the low-density lipoprotein (LDL) starts to accumulate in the arterial intima, relying on the good ability of LDL to infiltrate into the endothelium or to adhere to extracellular matrix components [3]. The LDL then undergoes oxidation and aggregation, which forms modified LDL and oxidized lipid moieties [2]. These factors stimulate the immune response and cause inflammation [2]. Specifically, these factors induce endothelial cells and smooth muscle cells to express adhesion molecules, chemoattractants, and growth factors that stimulate homing and migration of monocytes, and differentiation of the monocytes into macrophages and dendritic cells [2]. Lipids then deposit on the macrophages and dendritic cells and form foam cells [2]. After forming several layers of foam cells in the intima, a visible yellow-colored layer called xanthomas or fatty streaks forms [2]. Many fatty streaks do not progress further, but some progress into pathological

intimal thickening, which shows small lipid pools beneath the layers of foam cells [2]. In the position where has high apoptosis and necrosis of foam cells and smooth muscle cells but has an impaired removal of apoptotic remnants, the lipid pool further grows into a necrotic core [2]. Afterward, neovessels grow into the base of the plaque, which provides an alternative entry pathway for monocytes and immune cells. However, the plaque neovessels are fragile and leaky and easily lead to intraplaque bleedings, which may expand the necrotic core and promote inflammation [2]. During the formation of the necrotic core and plaque neovessels, the connective tissue of the plaque may undergo fibrosis. The connective tissue gradually changes to collagen-rich fibrous tissue [2]. On the luminal side of the vessel wall, the smooth muscle cells that migrate here synthesize extracellular matrix composed of collagen-rich fibrous tissues, and this process forms the fibrous cap [2, 3]. The necrotic core and surrounding tissue then may be calcified and it forms a fibrocalcific plaque [2, 4].

During the development of the plaque in the coronary artery, the artery lumen becomes narrow. The arterial remodeling increases the cross-sectional area of the artery to compensate for the narrowing of the lumen area [2, 5]. However, when the plaque is too large, it may restrict the coronary artery blood flow and lead to atherosclerosis caused luminal narrowing diseases (e.g. stable angina pectoris) [2]. In addition to luminal narrowing, atherosclerosis can lead to diseases through the caused thrombosis [2].

Thrombosis, a process related to forming a blood clot in a blood vessel, is usually caused by plaque rupture and plaque erosion[2, 4]. The fibrous cap of the plaque slowly

becomes thinner due to the gradual loss of smooth muscle cells from the fibrous cap and the degradation of the collagen-rich cap matrix by infiltrating macrophages [2, 5]. At the sites where the fibrous cap is thinnest, the plaque easily ruptures. Generally, the plaque rupture causes the formation of a gap in the fibrous cap that exposes the highly thrombogenic core to the blood in the arterial lumen [2]. A thrombus then starts to form. Initially, the thrombus forms within the plaque, and then it protrudes into the arterial lumen and its surface exposed to the blood will be covered by activated platelets [5]. The thrombus may further grow into a loose network of fibrin containing large numbers of entrapped red cells, and it may eventually occlude the artery [5]. In addition to plaque rupture, thrombus can also be formed by plaque erosion, which leads to loss of the antithrombotic properties of the plaque surface and exposure of a large area of the surface of the subendothelial connective tissue of the plaque [2, 5]. This erosion may be caused by the endothelial damage due to vasospasm, [2] endothelial cell loss due to macrophages, and the produced proteases loosening the endothelial cells from their adhesion to the vessel wall [5].

In most cases, part of the thrombus is removed by natural lysis. The exposed part of the thrombus becomes less active in causing platelet adhesion, the smooth muscle cells migrate into the area and produce new connective tissue, and the plaque integrity is restored [5]. However, in some cases, the thrombus can immediately narrow or block coronary arteries [6] and lead to a reduction in blood flow and reduction of nutrients and oxygen in cardiomyocytes, which leads to myocardial ischemia and myocardial necrosis [1, 6]. The myocardial necrosis due to extended ischemia in cardiomyocytes is called a

myocardial infarction (MI). Notably, most MI is caused by thrombosis that obstructs blood flow to the heart [2, 5].

Based on the changes in an ECG (electrocardiogram), MI can be classified into ST-elevated myocardial infarction (STEMI), non-ST-elevated myocardial infarction (NSTEMI) [7]. More recently, MI is classified into five more specific categories (Type 1 to Type 5), based on pathological, clinical and prognostic differences, along with different treatment strategies [8]. Type 1 MI refers to spontaneous myocardial infarction, which emphasize the MI related to plaque disruption and coronary athero-thrmbosis. Type 2 MI refers to myocardial infarction secondary to an ischemic imbalance, which emphasize the imbalance unrelated to acute coronary athero-thrombosis. Type 3 MI refers to myocardial infarction resulting in cardiac death when biomarker values are unavailable (before cardiac troponin values become available or become abnormal). Type 4a MI, Type 4b MI, and Type 4c MI, refer to myocardial infarction related to percutaneous coronary intervention, stent/scaffold thrombosis associated with percutaneous coronary intervention (PCI), and restenosis associated with percutaneous coronary intervention, respectively. Type 5 MI refers to myocardial infarction related to coronary artery bypass grafting (CABG) [8].

1.1.2. Prevalence, Incidence, and Mortality

The population affected by MI and the impact of MI are problematic. Specifically, the prevalence of MI, which refers to an estimate of how many people have MI at a given

point or period in time (including new and preexisting), is not low. According to data from NHANES (National Health and Nutrition Examination Survey) between 2011 and 2014, the overall prevalence for MI is 3% in US adults ≥20 years of age [9]. According to data from a self-reported national survey in the UK in 2014, there are about 915000 people have an MI in the UK [10]. MI also has a high incidence, which refers to the number of new cases of MI that develop in a population. It is reported that every 40 seconds, an American will have a MI [11]. From the 2005 to 2014 ARIC study of the NHLBI, the estimated incidence of new MI is 605000 per year in the US [11]. In addition, MI is a fatal disease; based on an AHA calculation, it is estimated that around 14% of the people who experience MI will die of it [9]. Moreover, mortality rate in MI poses serious problems. Based on a data from world health organization (WHO), 17.9 million people die from cardiovascular diseases in 2016 globally and 85% of the deaths are due to MI and strokes [12]. According to the US national Medicare data from 2015 to 2016, the median hospital risk-standardized mortality rate for MI was 13.1%, and the median risk-standardized 30-day readmission rate was 15.8% [11]. MI has posed a large economic burden to the US health system with annual costs estimated at $177.1 billion [13].

It worth to note that MI affects male and female differently. The prevalence of MI in males (4.0%) is higher than the prevalence in females (2.3%). From data in the UK in 2013, the prevalence of MI in males was about three times higher than in females [10]. In addition, the incidence of MI in males is higher than it in females in all age groups. The mortality of MI in males (57.9%) is also higher than it in females (42.1%) [11]. MI also

shows higher prevalence, incidence, and mortality in elder groups or populations than in younger groups of populations [10, 11].

The impact of MI on different ethnic groups are also different. Specifically, the prevalence of MI in US adults (≥20 years of age) is different in different ethnic groups; the prevalence of MI is similarly high in both non-Hispanic White and non-Hispanic Black, followed by Hispanic and non-Hispanic Asian [11]. In addition, Black has a higher incidence of MI in all age groups [11]. It is also reported that the median survival time after a first MI for blacks (7.0 years for males, 5.5 years for females) is shorter than that for whites (8.4 years for males, 5.6 years for females), in the patient group of ≥45 years of age [11]. Another study reports that survival and life expectancy after MI were higher in whites (7.4%) than in blacks (5.7%) [11].

In addition, several studies reports that socioeconomic status is related to recurrent MI, mortality, and MI incidence. In a study in central Israel, living in poor socioeconomic status neighborhoods was associated with greater risk for recurrent MI after the patients were discharged from hospitals after first MI [11]. A study of Finnish adults shows that income and education were associated with MI incidence, and low adult socioeconomic resources was a strong determinant of MI incidence and fatality [11]. In a study for US adults (45 - 74 years of age) in 2009 to 2013, economic/social conditions is a main factor accounting for the US county variation in cardiovascular disease mortality (32% of the variation in county cardiovascular disease), in addition to other factors including demographic composition (36%), healthcare utilization, features of the environment, and health indicators (the three cumulatively accounted for 6%) [14]. It was reported that there

is a higher mortality rate after MI in patients with characteristics like lower socioeconomic status, poorer social support, etc. [15]. In addition, differences in life expectancy between white and black patients were smaller in medium and low socioeconomic status areas, but were larger in high socioeconomic status areas [11]. In another study of MI mortality for the period 1999-2007 in the US, it shows that neighborhood with a high proportion of the population with low education (less than high school education) tended to have a higher MI mortality [13].

1.1.3. Treatment

For patients with chest pain and/or suspected MI, treatment can be started after onset of the symptom and before arriving the hospital [16]. Prehospital treatments, like cardiopulmonary resuscitation (CPR), early defibrillation using automated external defibrillators (AEDs), can be used immediately after the onset of the symptom [16]. Prehospital emergency medical system can administrate aspirin on the way transporting the patient to hospital [16].

After the patient arrives the emergency department, supplemental oxygen, nitroglycerin, analgesia, aspirin, beta-blockers, and reperfusions can be administrated. The supplemental oxygen may help to limit the ischemic myocardial injury. The nitroglycerin leads to peripheral arterial and venous dilation and helps to improve coronary flow. Analgesia (e.g. morphine sulfate) is used to relief the pain caused by MI [16]. Aspirin can produce antithrombotic effect and largely reduce the mortality risk [17]. Beta-blockers reduces myocardial oxygen demand by reducing heart rate, systemic arterial pressure, and

myocardial contractility, which eventually reduces magnitude of infarction, rate of reinfarction, and mortality [17].

Notably, reperfusion, which refers to the restoration of the blood flow in the obstructed infarct artery, is very important in the treatment of MI patients. Usually, reperfusion can be accomplished by fibrinolytic therapy (pharmacological approach) and primary percutaneous coronary intervention (catheter-based approach) [16].

In fibrinolytic therapy, plasminogen activators are used to expose the active enzymatic center of plasmin, which then cleaves the fibrin cross-links and breaks down the thrombus [17]. Some approved plasminogen activators include alteplase, reteplase, streptokinase, and tenecteplase-tPA [17]. These fibrinolytic agents are used via intravenous administration, and the cost per dose of these fibrinolytic agents ranges from $613 to $2974 [17].

Based on AHA guideline, percutaneous coronary intervention (PCI) refers to a group of technologies capable of relieving coronary narrowing. It includes percutaneous transluminal coronary angioplasty, rotational atherectomy, directional atherectomy, extraction atherectomy, laser angioplasty, and implantation of intracoronary stents and other catheter devices [18]. The cost for PCI is high, with the mean hospital charges of around $84813 in 2014 [11]. PCI is an invasive non-surgical procedure [19]. The most commonly used PCI is percutaneous transluminal coronary angioplasty or implantation of intracoronary stents [19]. In the procedure of percutaneous transluminal coronary angioplasty, a needle is first inserted into the femoral artery, followed by the insertion of a guidewire through the needle into the blood vessel [20]. A sheath is then placed over the

guide wire and into the femoral artery. A diagnostic catheter for imaging of the coronary artery can then be inserted through the sheath. To perform percutaneous transluminal coronary angioplasty, a guide catheter with a larger luminal diameter is inserted similarly to the diagnostic catheter, and it is placed in the ostium of the respective artery. A guidewire is then inserted through the catheter and across the blocked or narrowing area. A balloon wire is then guided to the blocked or narrowed site, and the balloon is then inflated and deflated repeatedly to widen the passage [20]. Intracoronary stents are usually used together with percutaneous transluminal coronary angioplasty to hold the artery open and improve clinical outcomes [19, 20]. To insert a stent, the balloon is deflated and the balloon wire is removed and exchanged for a stent. A collapsed stent is positioned in the initially narrowed site widen by the balloon. The collapsed stent is then expanded, and the stent stays in the position. After confirming that the blood flows well in the artery, the catheter is removed and the procedure is completed [20].

Selection of fibrinolytic therapy or PCI depends on time length from onset of symptoms, risk of mortality, risk of bleeding, and time required for transport to a skilled PCI lab [16]. The efficacy of fibrinolytic therapy is more depends on the time length from onset of symptoms, with the best efficacy with short time and worst efficacy with a long time [16]. It is reported that fibrinolytic therapy administrated within the first 2 hours may abort MI and largely reduces mortality [21, 22]. PCI is favored than the fibrinolytic therapy when the estimated mortality with fibrinolytic therapy is very high [16]. In addition, PCI is favored than the fibrinolytic therapy when the risk of bleeding with fibrinolytic therapy is high in the patient [16]. However, the interventional cardiology

facility for PCI is not always available, in contrast to the more available fibrinolytic therapy. According to the ACC/AHA guideline, fibrinolysis therapy should be administrated if the primary PCI cannot be administrated within 1.5 hours of first medical contact unless contraindicated [16].

In addition to PCI and fibrinolytic therapy, MI can be treated by coronary artery bypass graft (CABG), which requires an open-heart surgery. CABG can be useful as the primary reperfusion strategy in patients who have suitable anatomy and who are not candidates for fibrinolytic therapy or PCI [16]. In CABG, a healthy blood vessel from another part of the patient's body is used to connect the blood vessels above and below the narrowed artery. The used healthy blood vessel reroutes the blood and bypasses the narrowed or blocked coronary arteries [23]. The cost for CABG is much higher than PCI and fibrinolytic agents, with the mean hospital charges of around $168541 for CABG in 2014 [11].

Many factors play a role in the selection of CABG or PCI. In comparison to CABG, PCI is easier to use and requires shorter convalescence and lower cost [18, 20]. PCI is favored over CABG for critical coronary artery stenosis [19]. However, PCI often requires the blocked artery to meet some anatomical criteria, but CABG has less limitation on this [18]. CABG is favored than PCI in patients with diabetes with multivessel disease. In addition, SYNTAX score, which can estimate the complexity of coronary lesions, is used to help make the selection [19]. For example, CABG is favored over PCI in patients with two or three-vessel disease and high SYNTAX score. CABG is also favored over PCI in

patients with the left main disease or one or two-vessel disease and low SYNTAX score [19].

Ancillary therapy, such as antithrombins and low molecular weight heparin, can be used together with reperfusion therapy [17]. It can help to facilitate and maintain coronary reperfusion, limit the consequences of myocardial ischemia, enhance myocardial healing, and reduce the likelihood of recurrent events [17]. In clinical settings, multiple of the treatments mentioned above may be used together to further increase clinical outcomes.

After applying therapy on MI patients, the patients are continued to be monitored and managed in the hospital. During the hospital stay, patient education is provided; patient's level of activity and diet are managed; anxiety level is assessed and managed; medication administration is managed; infarct size is measured; hemodynamic disturbances are assessed, and if there are any complications, such as hypotension, low-output state, pulmonary congestion, cardiogenic shock, right ventricular infarction, the patient will undergo its corresponding treatment; the patient is evaluated to exclude arrhythmias after MI, recurrent chest pain after MI, ischemic strokes, deep venous thrombosis, and pulmonary embolism, and the patient will be treated if there are any of these symptoms; risk stratification is used to determine whether the patient is a candidate for discharge or needs a follow-up treatment. After the patient is discharged from the hospital, the patient may undergo cardiac rehabilitation and follow-up visit for long-term management of cardiac health [16].

CABG and PCI, the treatments that are more expensive than fibrinolytic therapy, are widely used because the efficacy of both methods depends less on the time length after the onset of MI symptoms. It is estimated that 371000 of CABG and 480000 of PCI, have been operated for inpatients in the US in 2014 [11]. The high costs of treatment together with other costs of medical care make MI 1 of the 10 most expensive conditions ($12.1 billion) treated in US hospitals in 2013 [11]. Because the efficacy of fibrinolytic therapy depends a lot on the short time length from the onset of symptoms, the time length is better to be controlled to be short. In addition, it is mentioned that the time to administrate the reperfusion therapy is a key determinant of short- and long-term outcomes of the MI patients [16]. It is emphasized the gains from reperfusion are greatest in the first few hours of symptom onset and rapidly decline afterwards [7]. Keeping the time between the onset of MI and PCI treatment within 2 hours to within 1.5 hours is recommended to maximize the benefits for reperfusion by PCI [16]. Morbidity and mortality of MI can be reduced significantly if patients and bystanders recognize symptoms early, activate the EMS system, and shorten the time to definitive treatment [16]. Therefore, achieving a short time length between treatment and onset of symptoms and administrating the treatment rapidly are important for MI patients.

1.2. Diagnosis of myocardial infarction

MI patients usually show the symptoms of chest pain, shortness of breath, weakness, nausea, vomiting, and/or fatigue [24]. These symptoms are also common in other health conditions, and thus MI may easily be confused with other diseases [25].

Thus, diagnosis of MI relies on other techniques in addition to the symptoms. The American Heart Association (AHA) and the American College of Cardiology (ACC) guidelines provide some recommended diagnostic procedures to decide on the need for hospitalization and assist in the selection of an optimal treatment for patients presenting with chest pain suspected to have a MI [7]. Specifically, diagnosis of MI relies on a combination of the patient's medical history and risk factors, a physical examination, ECG, and testing of cardiac biomarkers from blood [8]. In addition to ECG and blood biomarkers, imaging methods, such as chest X-ray, transthoracic echocardiography, transesophageal, and a contrast chest computed tomographic scan or a magnetic resonance imaging scan can be used to learn more about a patient's condition and rule out other causes of symptoms [7, 8, 16]. The results from diagnostic tests and risk stratification tools based on patient history can help clinicians decide on discharge or admission of the patient, guide the treatment, and help select the site of care (outpatient monitored unit, monitored step-down unit, or coronary care unit) [7].

In terms of the more specific MI categories (Type 1 to Type 5), the criteria for diagnosis of each category of MI are also slightly different. Specifically, the criteria for diagnosis of Type 1 and 2 MI include elevated cardiac troponin values above the 99th percentile upper reference limit (URL), detection of a raise and/or fall of cardiac troponin values, evidence of acute myocardial ischaemia, and at least one of the following: symptoms of myocardial ischaemia, new ischaemic ECG changes, development of pathological Q waves, imaging evidence of new loss of viable myocardium or new regional wall motion abnormality in a pattern consistent with an ischaemic aetiology, or

identification of a coronary thrombus by angiography or autopsy (not for Type 2 MI) [8]. Type 3 MI is determined if the patient has the symptom of myocardial ischaemia, and new ischaemic ECG changes or ventricular fibrillation, but die before blood samples for biomarker can be obtained or before the increase in cardiac biomarkers can be identified.

Type 4 and Type 5 MI are coronary procedure-related MI. The criteria for diagnosis of Type 4b and 4c MI are the same as the criteria for Type 1 MI [8]. The criterion for diagnosis of Type 4a is an elevation of cardiac troponin values >5 times of the 99th percentile URL in patients with normal baseline values (≤99th percentile URL) within 48 hours after the procedure. The criterion for diagnosis of Type 5 is an elevation of cardiac troponin values >10 times of the 99th percentile URL in patients with normal baseline values (≤99th percentile URL) within 48 hours after the procedure [8].

The length of time spent on the diagnosis of MI is important. Firstly, early diagnosis of MI is critical to ensure rapid treatment of the patients. It is mentioned that a rapid treatment usually requires a less invasive treatment and also leads to a much lower mortality [7, 26, 27]. As mentioned above, keeping the time between the onset of MI and PCI treatment within 2 hours to within 1.5 hours is recommended to maximize the benefits for reperfusion by PCI [16]. In addition, it is recommended to control the door-to-needle time within 30 min and door-to-balloon time within 90 min [16]. Secondly, early rule-out of non-MI patients and the consequent early discharge help to avoid the prolonged monitoring and the high cost of staying in the hospital [28].

There are several diagnostic protocols recommended in the guidelines for the diagnosis of MI [24]. To decrease the time for diagnosis of MI, accelerated diagnostic

protocols with less steps have been established in addition to the comprehensive protocols. In the accelerated diagnostic protocols, the minimum tests are ECG and troponin tests [7]. Because both ECG and troponin tests can be performed in an emergency department, a separate chest pain unit, or a telemetry unit [7], the accelerated diagnostic protocols largely increase the access to MI diagnosis in resource-limited settings.

In terms of ECG, it is recommended that an ECG should be obtained and interpreted as soon as possible within 10 minutes of arrival in the emergency department in all patients with suspected MI [25, 29]. Additional ECG is performed when there are recurrent symptoms or diagnostic uncertainty [25].

In terms of the troponin tests, serial measurements of troponin at different time points after a patient presents in the emergency department are usually used. Generally, a patient is very likely to have MI when a high 0-hour concentration of troponin or a high absolute change of troponin within 1h, 2h, or 3h during serial measurements is present [24]. Monitoring of dynamic changes of troponin in serial measurements is important, because it helps to distinguish MI from other non-MI cardiac diseases (e.g. valvular heart disease, heart failure, myocarditis) that can lead to a high troponin level at 0 hour [25]. Because the time points for monitoring of troponin are different in different diagnostic protocols, the lengths of time for the patients to stay for monitoring varies. Currently, the decision algorithms that require a relatively short length of time are 0/3h-ESC Algorithm, 2h-ADP Algorithm, 0/2h Algorithm, Alternative 1h Algorithm, 0/1h-ESC Algorithm, and Very Low cTn Algorithm [24]. Among the 6 algorithms, the Very Low cTn Algorithm, 0/3h-ESC Algorithm, and 2h-ADP, are only used for rule-out of MI. The Very Low cTn

Algorithm requires only one measurement of troponin at 0 hour after the patient presents in the emergency department. The 0/3h-ESC Algorithm and 2h-ADP require measurements of troponin at 0 hour and 3 hour and 0 hour and 2 hour, respectively. The 0/2h Algorithm, Alternative 1h Algorithm, and 0/1h-ESC Algorithm, can be used for both rule-in and rule-out of MI. The 0/1h-ESC Algorithm and the Alternative 1h Algorithm require measurements of troponin at 0 hour and/or 1 hour after the patient presents in the emergency department. The 0/2h Algorithm requires measurements of troponin at 0 hour and 2 hour [24]. The 0/1h-ESC Algorithm is the most rapid algorithm for both rule-out and rule-in of MI. Specifically, when using the ARCHITECT STAT high sensitive troponin I immunoassay, the 0/1h-ESC Algorithm rules in MI when cardiac troponin I level is higher than 0.052 ng/mL at 0 hour or the 1-hour change of cardiac troponin I is higher than 0.006 ng/mL. It also rules out MI when cardiac troponin I level at 0 hour are lower than 0.005 ng/mL at 0 hour and the 1-hour change of cardiac troponin I is lower than 0.002 ng/mL. In addition, the Very Low cTn Algorithm is the most rapid algorithm for rule-out MI. When using the ARCHITECT STAT high sensitive troponin I immunoassay, the Very Low cTn Algorithm rules out MI when cardiac troponin I level is lower than 0.002-0.005 ng/mL at 0 hour [24]. Therefore, in the most rapid scenario of using troponin tests, a patient with suspected MI can be ruled in or ruled out within 1 hour after presence in the emergency department.

1.3. Cardiac biomarkers for myocardial infarction

Cardiac biomarker testing is widely used in the emergency department. In a study of emergency department visits by adults (≥18 years old) selected from the 2009 and 2010 National Hospital Ambulatory Medical Care Survey, it is reported that biomarker testing occurred in 16.9% of the emergency department visits in the U.S. (28.6 million visits) [30]. In addition, cardiac biomarker testing is frequently used in emergency department visits, no matter the patient has clinically relevant symptoms or not [30]. In addition to diagnosis, serial cardiac biomarker measurements are also useful for monitoring and managing MI patients, such as offering supportive noninvasive evidence of reperfusion after administrating therapy [16].

Several parameters are often used in clinical studies to evaluate the performance of the cardiac biomarkers. Area under the curve refers to the area under the receiver operating characteristics (ROC) curve. A large area under the curve indicates a high probability of correct classification or prediction and a good diagnostic ability. Negative predictive value (NPV) refers to the percentage of patients with a negative test who do not have the disease. A high NPV value usually indicates a good ability of the biomarker for rule-out. Sensitivity refers to the percentage of persons with the disease who are correctly identified by the test. Specificity refers to the percentage of persons without the disease who are correctly excluded by the test [31].

Cardiac troponin is a well-established cardiac biomarker for MI. Cardiac troponin is a protein located on the actin-containing thin filament of the sarcomere of cardiac muscles [32]. Troponin attaches to tropomyosin and contains binding sites for calcium ions. When no calcium binds to troponin, the tropomyosin covers the myosin-binding sites

of actin. In this case, the interaction between myosin and actin is inhibited. When calcium ion binds to troponin, troponin pulls the tropomyosin away from the myosin binding sites and exposes the myosin-binding sites. Myosin head then attaches to the myosin-binding site of actin and pulls the actin filament. This process leads to the contractile movement of the cardiac muscle. After calcium becomes dissociated from troponin, muscle relaxation occurs [32]. In a healthy human, troponin circulating in the blood is low. When cardiomyocytes are damaged due to MI, more troponin is released into the circulation, and the concentration increases [32]. The troponin levels rise within a few hours of symptom onset and typically remain elevated for several days [7].

Troponin is a complex of three subtypes, troponin C, troponin T, and troponin I. Troponin C serves to bind four calcium ions, troponin T serves to bind to the tropomyosin, and troponin I serves to bind to actin and inhibit the interaction of actin with myosin [32, 33]. Because the troponin T and troponin I in cardiac muscle have different structures compared with the troponin T and troponin I in skeletal muscle, cardiac troponin T (cTnT) and cardiac troponin I (cTnI) can be used to specifically indicate cardiac muscle damage [34]. Guidelines from ACC and AHA have identified cTnI or cTnT as the preferred biomarker for MI and the evaluation of myocardial injury [26]. Early troponin measurement (within 6 hours of arrival) is recommended for all patients with acute NSTEMI [35].

Consensus has been reached that the cut-off value of cardiac troponin for MI is defined as the 99th percentile upper reference limit (URL). The 99the percentile URL is obtained by measuring the cardiac troponin levels in a healthy population using a cardiac

troponin assay. It should be noted that the cut-off values of cardiac troponin are population- and assay-dependent. The troponin concentration is affected by the sex and age of the population, and thus the cut-off value varies [24]. To reduce the sex and age factors, sex-specific and age-specific cut-off values of troponin have been used [36, 37]. However, more studies are still needed to elucidate the benefits and/or harms of using sex- and age-specific cut-off levels in the diagnosis of MI [24, 36]. In addition, because the 99th percentile value is assay-dependent, the specific cut-off values are different when using different troponin assays. For example, when using ARCHITECT i2000SR cTnI immunoassay (Abbott Diagnostics), the 99th percentile cut-off is 0.027 ng/mL [38]. When using the ADVIA Centaur cTnI assay (Siemens Healthcare Diagnostics), the 99th percentile cut-off is 0.04 ng/mL [39, 40]. Although the specific values vary, the 99th percentile cut-off values are mostly within the range of 0.01-0.1 ng/mL [39]. As mentioned in Section 1.2, in addition to the absolute concentration of cTnI at a time point, quantifying changes of troponin within 1h, 2h, or 3h during serial measurements is also important. Therefore, a quantitative assay for the detection of cTnI should cover 0.01-0.1 ng/mL for the diagnosis of MI.

Many other cardiac biomarkers have been mentioned in clinical studies for their values in the diagnosis or prognosis of MI. Copeptin and heart-type fatty acid-binding protein (h-FABP) are two cardiac biomarkers important for MI.

Arginine-vasopressin (AVP) is a hormone related to antidiuresis, vasoconstriction, and stress response [41, 42]. AVP originates from provasopressin and is mainly synthesized in the hypothalamus and released from the posterior pituitary [41, 43]. Some

studies show that AVP may also be synthesized by cardiac tissues and other tissues outside the hypothalamus, but more studies are needed to confirm these findings [41, 43]. When the presence of MI, homeostasis of the body is disturbed, which acts as a stress and thus activates the release of AVP [43]. Therefore, measurement of AVP can help to indicate MI. However, AVP has a short half-life (5-15 min) and is easily bound to the platelet. Due to this, direct detection of AVP is difficult [42]. Copeptin, the C-terminal segment of provasopressin, is a glycosylated 39 amino acid polypeptide and is stoichiometrically co-secreted with AVP [44]. Copeptin is better than AVP as a biomarker for measurement due to its longer half-life (82 min) in circulation and its good stability during days after blood withdrawal at room temperature [43, 44]. Copeptin is elevated 0-4 h after the onset of symptoms of acute MI [45]. In a healthy human, the copeptin concentration is in the range of 0.004-0.018 ng/mL (1-4.4 pM) [43]. The clinical cut-off value of copeptin to indicate MI is 0.056 ng/mL (14 pM) [43]. Therefore, a quantitative assay for the detection of copeptin should cover 0.004-0.056 ng/mL.

Copeptin has value in diagnosing MI, predicting infarct size, and predicting outcomes after MI [43]. In contrast to the standalone biomarker of MI like cardiac troponin, copeptin is more often used as an add-on biomarker. ESC guidelines mention that copeptin has clinical value for the diagnosis of MI when combined with troponin [46]. Several clinical studies demonstrate the additive value of copeptin on troponin for early rule-out of MI [47-49]. A rapid and reliable rule-out of MI may obviate the need for prolonged monitoring and serial blood sampling in the emergency department for the majority of patients, and thus reduce the cost and the time of their stay [42]. It is reported

that a dual-marker strategy combining normal levels of troponin together with low levels of copeptin at presentation shows a very high NPV for MI [46, 49]. Another study shows that combining copeptin and cTnI provides a high NPV of 98% among populations with a high prevalence of acute MI [50]. Adding copeptin to troponin also improves the sensitivity for the diagnosis of acute MI from 87% to 96% [47]. In another study, the combination of copeptin and cardiac troponin provides a high area under the ROC curve (0.97), a high sensitivity (98.8%), and a high NPV (99.7%) for acute MI [42]. Notably, the additive value of copeptin on cardiac troponin is especially important in the first 3 hours of symptom onset when the cardiac troponin levels have not increased a lot [43]. For acute MI within 3 hours after chest pain onset, the combination of copeptin and cTnT achieves a higher area under the ROC curve (0.9 vs. 0.77), sensitivity (85.1% vs. 43%), and NPV (92.4% vs. 82.4%) compared to cTnT alone [48]. ESC guidelines emphasize that the additive value of copeptin to conventional (less sensitive) troponin assays is substantial [46]. The routine use of copeptin as an additional biomarker for the early rule-out of MI is recommended especially when the very sensitive troponin assays are not available and only the less sensitive troponin assays are available [46]. When the very sensitive troponin assays are available, copeptin may still have some additive value in the early rule-out of MI [46].

Heart-type fatty acid-binding protein (h-FABP), is a cytosolic protein that is involved in the transportation of long-chain fatty acids [51]. In extracellular fluids, fatty acids can be transported by albumin. In the myocyte cytoplasm, h-FABP is the transporter that is bound to the long-chain fatty acids and transports them to the mitochondria outer

membrane [45, 52]. H-FABP mainly present in cardiac myocytes [45]. Although h-FABP also presents in skeletal muscle, brain, and kidney, the concentrations at these locations are very low [45]. When myocardial ischemia occurs, h-FABP leaks out of myocardial tissue leading to a concentration increase in blood [53]. Due to the smaller molecular weight (15 kDa) than cardiac troponin (23.9 kDa for cTnI) and the primarily cytosolic location, h-FABP reaches a high concentration in plasma or serum much earlier than cardiac troponin [52]. h-FABP can be detected as early as 1 h after the onset of acute MI [54]. Its plasma concentration reaches the peak value 8 h after onset of symptoms with a clearing time within 36 h of onset [53]. Due to the shorter clearing time of h-FABP, its concentration decreases and returns to baseline faster than cardiac troponin [45]. Thus, sustained high concentrations of h-FABP may indicate the presence of re-infarction, which may be missed if only using cardiac troponin [45]. However, renal diseases impair the clearing of h-FABP, which also causes a high concentration of h-FABP. In addition, h-FABP exhibits low specificity in the detection of MI in the presence of skeletal muscle injury and renal insufficiency [55]. The often-used clinical cut-off value of h-FABP is 6.2 ng/mL [56]. Other cut-off values within the range of 5-16.8 ng/mL are also used [57]. Thus, a quantitative assay for the detection of h-FABP should cover the 5-16.8 ng/mL range.

Instead of being used as a standalone biomarker [45], h-FABP is better to be used as an add-on biomarker, and its add-on value of h-FABP has been discussed in multiple studies [58-61]. The combination of h-FABP and cardiac troponin improves early rule-out of acute MI [58, 60] and helps early diagnosis of MI [60, 62, 63]. Specifically, the addition

of h-FABP to cardiac troponin improves the diagnostic sensitivity from 42–75% to 76–97% in the early hours of MI [62]. It is mentioned that combined measurement of an early biomarker such as h-FABP and a later biomarker such as cardiac troponins may provide the optimum diagnostic performance of MI [63].

In addition, the combination of h-FABP and cTnT provides a higher sensitivity (85%) compared to h-FABP alone (73%) or cTnT alone (55%), and improves NPV (91% combined vs 74% h-FABP or 81% cTnT) indicating a better ability to rule-out acute MI in patients presenting with acute chest pain [58]. In another study, the combination of cTnI and h-FABP shows a higher area under the ROC curve (0.868 vs. 0.762) and NPV (94% vs. 92%), compared to cTnI alone at 0-3 h after chest pain onset [60]. The combination also shows higher sensitivity (71.4%) than cTnI alone (50%) and h-FABP alone (64.3%) at 0-3 h after chest pain onset [60]. Combination of cTnI and h-FABP also shows higher sensitivity (88.2%) than cTnI alone (67.6 %) and h-FABP alone (85.3%) at 3-6 h after chest pain onset [60]. Moreover, the sensitivities of h-FABP + cTnI are higher than CK-MB + cTnI and myoglobin + cTnI at both 0-3 h and 3-6 h after chest pain onset [60].

In addition to the clinical values mentioned above, h-FABP provides incremental information in addition to cTnI for risk assessment [61]. Specifically, the elevation of h-FABP indicates a higher risk of heart failure, MI, death, or the composite of the three through 10 months after the measurement [61]. The three risk levels using h-FABP are defined as low (<8 ng/mL h-FABP), medium (8 to 16 ng/mL h-FABP), and high (>16 ng/mL h-FABP) [61]. Another study also shows the additive value of h-FABP for predicting adverse events (death or MI) in low- and intermediate-risk patients with

suspected acute coronary syndrome [59]. In summary, h-FABP has value in early diagnosis of MI, improving early rule-out of MI, indicating re-infarction, and risk assessment in MI.

In conclusion, cardiac troponin is a well-established cardiac biomarker recommended in guidelines as a diagnostic biomarker for MI. The development of cTnI assay will be useful and important for the assessment of patients with suspected MI. Compared to using a single-biomarker, using a panel of cardiac biomarkers can achieve a better clinical value for MI. Specifically, h-FABP and copeptin are good selections to add on cTnI as a cardiac biomarker panel. Adding h-FABP can help to achieve early diagnosis of MI, indicate re-infarction, and improve early rule-out of MI. The sensitivity and NPV when adding copeptin to cTnI is even higher than adding h-FABP to cTnI, thus copeptin helps to further improve sensitivity and improve early rule-out of MI. Using the panel consisting of cTnI, copeptin, and h-FABP ensures that the patients can be diagnosed with high sensitivity and high specificity, the clinical outcomes may be better predicted, and the non-MI patients can be ruled out rapidly. Moreover, when cTnI is multiplexed with the two add-on biomarkers, the need of detecting the very low concentration of cTnI (0.002 ng/mL) for early rule-out of MI may be obviated.

1.4. Multiplex point-of-care testing (xPOCT)

Measurement of cardiac biomarkers plays an important role in the diagnosis of MI. In addition, it has been mentioned that obtaining the measurement results of cardiac biomarkers within 60 minutes is recommended [25]. In a well-run hospital, measurements

of the cardiac biomarkers in blood rely on automated platforms in a central laboratory, which requires about 1-hour turnaround time [25]. At resource-limited clinical settings or remote clinical settings, the access to blood biomarker tests may be limited and the turnaround time of the measurements may be even longer. In addition, the automated platforms in a central laboratory are usually very expensive and need well-trained staff [64].

Point-of-care testing (POCT) is a technique to implement the traditional diagnostic tests normally finished in a central laboratory at near-patient settings [65]. In this way, the transportation of the blood sample from the patient to the central laboratory and the long turnaround time can be avoided. Because POCT can provide measurement results to a patient and a doctor on-site, it may accelerate the clinical management of the disease and may help to improve patient outcomes, especially at resource-limited settings [64]. World health organization (WHO) set up ASSURED criteria (Affordable, Sensitive, Specific, User-friendly, Rapid and robust, Equipment-free, Deliverable to end-users) for an ideal POCT [64, 66]. These criteria have been expanded to REASSURED criteria (addition of Real-time connectivity, Ease of specimen collection, and Environmentally friendliness) to guide the development of POCT in this growing field [67]. Specifically, Affordable refers to the cost-effectiveness of a test; Sensitive refers to few false-negatives when using the POCT for diagnosis of a disease; Specific refers to few false-positives when using the POCT for diagnosis of a disease; User-friendly refers to that the test should be easily performed, typically in two to three steps, and it requires minimal user training; Rapid refers to that the test can provide results within 15 to 60 minutes after sample collection;

Robust refers to that the test can withstand the condition and environment when it is transported and stored; Equipment-free emphasizes ideally no special equipment is needed, and if an equipment is needed, it should be simple; Deliverable to end-users refers to the test can reach the end-users, including users from resource-limited settings; Real-time connectivity refers to allowing for centralized and real-time result-analysis and decision-making; Ease of specimen collection refers to a simple procedure in sample collection; Environmentally friendliness refers to reducing or avoiding the usage of materials harmful to the environment [67].

Because POCT has features different from the traditional diagnostic tests normally finished in a central laboratory, it is suitable for applications in doctors' offices, emergency departments, ambulances, cares at home, remote health cares, and resource-limited settings. Especially, in resource-limited areas where usually have limited available laboratory testing, patients usually need to travel hours to access medical staff and supplies [64]. Thus, resource-limited settings particularly need POCT to improve patients' access to care and to avoid the failure of health services [64].

Multiplexed point-of-care testing (xPOCT) refers to POCT that can simultaneously detect multiple biomarkers from a single specimen [68]. xPOCT is more efficient to detect a biomarker panel, compared with using multiple single biomarker assays for each biomarker. Compared with using single biomarker assays for multiple biomarkers, xPOCT could reduce the total volume of sample, analysis time, and total cost [69].

Table 1.1 Commercial devices for multiplex detection of biomarkers for myocardial infarction. Adapted from "A Review of Biosensor Technologies for Blood Biomarkers Toward Monitoring Cardiovascular Diseases at the Point-of-care" by Ouyang, M.X., et al., Biosensors and Bioelectronics, 2021. 171: p. 112621.

Company	Devices	Reader	Sample Volume (µL)	Time (min)	Biomarkers	Detection Range (ng/mL)
Nano-Ditech	Nano-Check AMI 3 IN 1, ND-CD301S	Qualitative result without reader	200-250	15	cTnI CK-MB Myoglobin	0.5 5 80
Cortez Diagnostics	RapiCard InstaTest	Qualitative result without reader	300-800	15	cTnI CK-MB Myoglobin	1.5 7.0 100
Boditech	Ichroma II Cardiac Triple	Quantitative result with a reader.	75	12	cTnI CK-MB Myoglobin	0.01-15 3-100 5-500
Nano-Ditech	Fluoro-Check AMI 3 in 1	Quantitative result with a reader.	80	15	cTnI CK-MB Myoglobin	0.03 - 30 2 - 200 10 - 500
Nano-Ditech	Nano-Check AMI 3 IN 1, ND-CD302P	Quantitative result with a reader.	100-120	15	cTnI CK-MB Myoglobin	0.1 - 30 2 - 200 20 - 1,000
Nano-Ditech	Nano-Check AMI 4 IN 1, ND-CD402P	Quantitative result with a reader.	100-120	15	cTnI N-terminal propeptide B-type natriuretic peptide CK-MB Myoglobin	0.1 - 30 0.03 - 15 2 - 200 20 - 1,000
Princeton BioMeditech	LifeSign 3-in-1	Quantitative result with a reader.	120	15	cTnI CK-MB Myoglobin	1.5 5 50
Quidel	Triage Cardiac Panel	Quantitative result with a reader.	-	20	cTnI CK-MB Myoglobin	0.05 - 30 1 - 80 5 - 500
Quidel	Triage Cardio3 Panel	Quantitative result with a reader.	-	20	cTnI B-type natriuretic peptide CK-MB	0.01 - 10 0.005-5 1 - 80
Randox	Randox Biochip Cardiac Array	Quantitative result with a reader.	-	-	cTnI CK-MB Myoglobin h-FABP	0.18-50 0.4-100 1.8-700 0.15-100

Many devices for the multiplex detection of biomarkers for MI are commercially available [31]. As shown in Table 1.1, most of these current commercial devices are for conventional biomarker panels composed of cTn, CK-MB, and myoglobin. None of these devices is for detection of the panel composed of cTnI, copeptin, and h-FABP, which is a better biomarker panel for MI as mentioned in previous sections. In addition, the detection ranges for cTnI of some devices do not cover the 0.01-0.1 ng/mL range. Lastly, for all of these devices, the sample volumes are relatively large (>75 μL) and bulky readers are needed for quantitative results.

In addition to commercial devices, many research efforts have been made to develop xPOCT devices for the detection of cardiac biomarker panels [70-72]. However, a large part of these developed xPOCT devices achieved a multiplex detection using spatial separation of test zones at different wells, lines, or dots [73-78]. This type of multiplexing is actually parallel single biomarker detection [68]. Although these spatial separation methods could achieve multiplexed detection, there are limitations like spatial and physical limitations of the strip and the uncertainty of flow variations of sample solution when passing through multiple detection areas [69].

Compared with these designs using spatial separation, multiplexed detection in a single test zone could reduce assay time, manufacturing cost, signal reading time, and the accumulative nonspecific sticking issue that is encountered in multiple lines/dots [69]. To achieve multiplexed detection in a single test zone, multiple labels with differentiable signals for each biomarker are needed [72, 77, 79-82]. Labels with different colours [80],

surface-enhanced Raman peaks [72, 77, 82], fluorescent peaks [79], time windows for signal reading [79, 81], or electrochemical redox peaks [82] can be used. Different from using the labels based on the electrochemical method [83], localized surface plasmon resonance [84], fluorescence [80], and chemiluminescence [85], the labels based on surface-enhanced Raman spectroscopy can achieve resolving signal via peak analysis of a spectrum [86]. In addition, the labels with different surface-enhanced Raman peaks have the advantages of low photobleaching, rich fingerprints, and narrow characteristic peaks [72, 77]. Multiplexed detection in a single test zone using labels with different surface-enhanced Raman peaks have been developed for detection of cTnI/myoglobin/CK-MB [72], cTnI/CK-MB [70], and cTnI/N-terminal prohormone of brain natriuretic peptide/neutrophil gelatinase-associated lipocalin [71]. However, this type of platform for cTnI/h-FABP/copeptin has not been developed. One recent study achieves simultaneous detection of the three biomarkers using temporally resolved chemiluminescence as the transduction element and using Co(II) catalyst/antibody/luminol functionalized gold nanoparticles to amplify the signal [85]. However, it requires complicated assay steps, including adding sample, sample incubation, washing, adding Co(II) catalyst/antibody/luminol functionalized gold nanoparticles, another incubation, washing, adding a buffer, overlapping two paper layers, and adding hydrogen peroxide. The complicated procedure is not user-friendly and requires a lot of user training.

Therefore, it is of great need to develop a user-friendly and simple-to-use xPOCT sensing system for the detection of biomarker panel composed of cTnI, copeptin, and h-

FABP, aiming at improving the diagnosis of MI, especially at resources limited clinical settings.

1.5. Transduction element

1.5.1. Surface-enhanced Raman spectroscopy (SERS)

Raman spectroscopy is a vibrational spectroscopic technique that measures the inelastic light scattering that occurs after the light interacts with a given molecule. Specifically, when an incident light hits a molecule, the oscillating electric field of the incident light leads to polarization of the molecule and may cause scattered light with frequencies different from the incident light [87, 88]. The scattered light with a frequency that is different from that of the incident light is called inelastic scattering. Notably, Stokes scattering, which is the scattered light with a longer wavelength than the incident light, is more often used in Raman spectroscopy than anti-Stokes scattering, which is the scattered light with a shorter wavelength than the incident light.

The wavelength change in inelastic scattering is caused by the vibration of the molecule. In the case of Stokes scattering, the incident photon excites a molecule at the ground electronic state to reach a virtual energy state. In this process, the molecule vibrates, which transforms part of the energy into vibrational energy. The energy level of the molecule is relaxed from the virtual energy level to the vibrational energy level, and meanwhile, a photon with lower energy than the incident photon is emitted [88]. The energy difference between the emitted photon and the incident photon leads to the change of the wavelengths of the incident and emitted lights.

In a Raman spectrum, the difference of wavenumber (reciprocal of the wavelength) between the emitted photon and the incident photon is read as a Raman shift. Because different vibrational modes have their characteristic vibrational energy levels, a specific molecule has its characteristic Raman spectrum. Raman spectrum can provide information about the chemical composition and molecular structure. Because Raman spectroscopy uses the intrinsic vibrational signature of a molecule, it does not photobleach. In addition, the vibrational peak is narrow (10-100 times narrower than fluorescence bands), so Raman spectroscopy has the ability to be used to resolve multiple molecules in a mixture [86, 89]. However, due to the low cross-section of Raman scattering (around 10^{-30} cm^2), the intensity of the spontaneous Raman scattering is very low (10^{-6} -10^{-9} of the intensity of incident light) [90].

Surface-enhanced Raman scattering (SERS) is an enhanced form of the spontaneous Raman scattering. A metallic surface is used, and the molecules adsorbed on the metallic surface obtain a strong enhancement in signal [91]. Compared to the spontaneous Raman scattering, SERS has an enhanced signal intensity (enhancement factors of 10^6~10^{14}) [92]. The enhancement that occurred in SERS is attributed to both electromagnetic (EM) enhancement and chemical (CHEM) enhancement.

The EM enhancement of SERS is explained below using a metal nanosphere as an example. When an incident light hits on a metal sphere with a size smaller than the incident light wavelength, the oscillating electric field of the incident light interacts with the conduction electrons in the metal [93]. This excites collective oscillations of the free electron gas, which is also called surface plasmon [93]. The oscillating surface plasmon

generates an EM field around the metal nanosphere surface [87]. Moreover, when the frequency of incident light is in resonance with that of the electron oscillation of the metal nanosphere, surface plasmon resonance (SPR) occurs [87]. The generated EM field from SPR is stronger than that from non-resonant surface plasmon. In the case of a metal nanosphere, the generated SPR localized in the nanosphere is called localized surface plasmon resonance (LSPR) [94]. The intensity of the generated EM field is usually very strong and is much stronger than that of the incident light, which can then largely amplify the Raman scattering signal of the molecule absorbed on the nanosphere surface. The Raman scattering signal of vibrational modes of the molecule that is normal to the surface is the most strongly amplified [87]. The enhancement factor attributed to EM enhancement can achieve in the range of 10^4-10^{11} [87, 95].

In contrast to EM enhancement, CHEM enhancement has a lower enhancement factor in SERS (10^2-10^3) [95]. The CHEM enhancement in SRES may be from different mechanisms: formation of chemical bonds, charge transfer, and charge-transfer resonance [96]. Compared with a free molecule in Raman spectroscopy, the formation of chemical bonds between molecule and metal in SERS may lead to change in the Raman polarizability, spatial orientation, and symmetry of the adsorbed molecule, which could enhance the Raman scattering [87]. In terms of the charge transfer, an exchange of electrons between the Fermi level of the metal and the lowest unoccupied molecular orbital (LUMO) or highest occupied molecular orbital (HOMO) of the molecule may occur [87]. Moreover, when the incident light energy is resonant with the electronic

transitions of the molecule-metal complex, resonance Raman occurs and Raman scattering signal is enhanced [87].

1.5.2. SERS tags

To better apply SERS in transducing sensing signals, SERS tags have been developed and widely used. Generally, a SERS tag is created by attaching Raman reporter molecules (RRM) that have intrinsically strong Raman scattering to the surface of metallic nanostructures [97]. A well-designed SERS tag should have a strong signal, narrow characteristic peaks, and good stability [98].

Because the EM enhancement contributes the most to the enhancement of the SERS signal, strategies to increase the EM field around the metallic surface are often used. Gold (Au) and silver (Ag) are the metals most commonly used in preparing the SERS tags [99]. Compared to Ag, Au has much better chemical stability [87] and better biocompatibility [100]. In addition to the material, the size of the particle and morphology of the nanostructure are the main factors that affect the intensity and distribution of the EM field [101]. In terms of the size of the particle, a larger size usually leads to a larger EM field and thus a stronger SERS signal [100]. Particles with sizes range from 30 to 100 nm are the best to obtain a strong SERS signal [102]. Too small or too large particle size may lead to a diminished SERS effect [102]. In terms of morphology, different nanostructures, such as nanosphere, nanostar, nanocube, nanorod, nanoflower, core-shell nanoparticle, and nanocluster, have been used in SERS tags [97, 103]. It has been reported that elongated nanostructures or those with edges and/or corners (e.g. nanorods,

nanocubes, nanotriangles, and nanostars) can generate strong EM fields concentrated at the vertices [101]. Specifically, the nanostars can produce a higher EM field at their sharp tips due to the trapping of the oscillating metal charges within highly confined spaces [101].

In addition to the elongated nanostructures, nanostructures with nanogap inter-particles or interior of the particle also generate a strong EM field. When two nanostructures are very close to each other, their transient dipoles could couple with each other and the generated EM fields of the two particles interfere coherently [94]. This small gap between the two nanostructures has the ability to concentrate an incident EM field and effectively amplify the near field between and around the nanostructures [104]. The small gap between the nanostructures with a very strong EM field is called a "hot spot"[104]. The SERS signal of one molecule can be enhanced by as high as 10^9 to 10^{12} when it is placed in a 1 nm^3 volume of the hot spot [87].

In nanostructures with nanogaps, the EM field amplitude is inversely correlated with the gap distance: a high EM amplitude in a small gap distance; a low EM amplitude in a large gap distance [88]. Notably, quantum tunneling effects may present for 0.3-0.7 nm or smaller gaps, which could reduce the EM field inside the nanogap, and thus this situation should be avoided for a strong SERS signal [88]. Thus, forming a nanosize gap above 0.7 nm should be good to achieve a strong EM amplitude. Designs with interparticle nanogaps are studied earlier than nanogaps interior of the particle. Lithographic and self-assembly methods have been used to make multimeric ensembles of metal nanostructures with interparticle nanogaps [105]. Among the self-assembly methods, increasing salt

concentration in a gold nanoparticle solution, which causes shielding of interparticle charge repulsion at elevated ionic strength, is a simple method to form the interparticle nanogap [106]. However, the assembly happens in a random way when using this method. The number of nanoparticles assembled in one cluster varies, which results in a large variance in particle size, anisotropic signal, fluctuation in signal intensity, and batch-to-batch inconsistency. More recently, the nanostructure with the nanogap interior of the particle was developed and studied [105, 107-112]. This nanostructure can be called gap-enhanced Raman tag [107], bilayered Raman-intense gold nanostructures with hidden tags (BRIGHTs) [113], or gap-enhanced nanoparticle. In a gap-enhanced nanoparticle, the interior nanogap generates hot spots with a largely enhanced EM field and then causes a strong SERS signal [99]. Compared with the multimeric ensembles with interparticle nanogaps, gap-enhanced nanoparticle could achieve highly uniform SERS signal [105]. In addition, the gap-enhanced nanoparticle can also be synthesized to have multiple layers of shell and gaps with different RRMs inside each gap. This type of gap-enhanced nanoparticle is also called multi-shell nanomatryoshka SERS tags [108]. The multi-shell nanomatryoshka SERS tags are often used for applications demanding high encoding capability [108].

The distance from the RRM to the metallic surface also affects the SERS intensity. To get a strong SERS signal, the distance from the RRM to the metallic surface needs to be small [114]. Forming a self-assembled monolayer (SAM) of RRM on a metallic particle is a useful way to ensure the RRM is closely attached on the surface of the metallic

surface. Thus, mixing RRM with the nanostructures and incubating them to form a SAM layer of RRM are commonly used in synthesizing SERS tags.

When using an RRM with an absorption spectrum close to the incident light wavelength, the incident light energy is resonant with the transitions between ground and excited electronic states of the RRM. This leads to the occurrence of surface-enhanced resonance Raman scattering (SERRS) [88]. Because Raman cross-sections are much larger in the resonant condition (typically by a factor of 10^2-10^6) than in non-resonant conditions [88], the SERRS signal is much enhanced than the SERS signal. To generate the SERRS signal, RRM that has the frequency of the electronic transition close to the frequency of the excitation light is needed [115]. Malachite green isothiocyanate (MGITC), a molecule with electronic transitions near 638 nm [116], can be used to form a SERS tag to generate the SERRS signal when used in a reader with a 638 nm laser.

To achieve good signal stability, a protective shell outside of the SERS tag can be used. The protective shell can be incorporated on the outside of SERS tags to prevent the RRM from dissociating and to prevent interfering molecules in a sample matrix from adsorbing on the surface of the metallic nanostructures. Polymers [117], bovine serum albumin (BSA) [118, 119], and silica [120-122] have been used to create the protective shell. It has been demonstrated that the silica shell particles can exhibit high stability, good water solubility, low nonspecific binding, and straightforward surface modification [97]. Due to these advantages, silica shell is a good protective layer for SERS tags. Synthesis of a SERS active particle with a resonant RRM and with a silica protective shell helps to achieve both strong and stable SERS signals.

As mentioned above, the gap-enhanced nanoparticle has a built-in hot spot in the interior gaps between its core and shell, which generates a strong EM field and thus could achieve a strong SERS signal. In addition to the strong SERS signal, the outer shell of the gap-enhanced nanoparticle also functions as a protective shell similar to the silica shell. This outer shell helps to prevent the desorption of RRM, and to prevent interfering molecules in a sample matrix from adsorbing on the surface of the metallic nanostructures [108]. In addition, it also avoids signal fluctuation due to the random aggregation-induced hot spots [108]. Because of this, the gap-enhanced nanoparticle is able to generate stable and uniform SERS signal. Moreover, embedding RRM in the interior gap leaves the outer surface of the particle available for other functionalization in specific applications. For example, in biosensing applications, this design helps to avoid the competitive adsorption between RRM and the recognition elements if both need to be functionalized on the outer surface. Due to these advantages, the gap-enhanced particle has been used in biosensing and bioimaging field [105, 107-112, 123]. The strong signal and good stability of the gap-enhanced particle makes it especially good for the detection of biomarkers in a low concentration range, like the copeptin and cTnI mentioned above.

Gap-enhanced particles composed of gold core/gold shell and gold core/silver shell have been reported [99]. However, gold has much better chemical stability [87] and better biocompatibility [100]. Thus, a gap-enhanced particle with a gold core and gold shell is more preferred. Galvanic replacement reaction could be used to replace the silver on the gold core/silver shell particle; however, it makes the synthesis process more complicated [124]. Studies have achieved the formation of gap-enhanced particles with a gold core and

gold shell using different spacers to form the gap, including oligonucleotides [109, 125-127], polymers [105, 110, 111], cyclodextrin [128], silica dioxide [112], and small organic molecules [107, 108, 129-131]. When the amount of spacers reaches an effective coverage on the core surface, a gap layer is formed between the core and grown shell [108]. When using oligonucleotides [109], polymers [105, 110, 111], cyclodextrin [128], and silica dioxide [112], as the spacer, the spacer takes a large portion of the surface area on the metallic core, which leads to a smaller area available for RRM to be embedded. Because of this, a tradeoff between the amount of RRM embedded and the quality of the formed gap has to be made when using oligonucleotides, polymers, and silica dioxide as the spacer. In addition, using oligonucleotides in synthesizing particles is less economic, especially in mass production.

Different from DNA, polymer, cyclodextrin, and silica dioxide, some studies have reported using RRMs, usually small organic molecules, as the spacer [107, 108, 129-131]. In this case, RRMs not only provide a large Raman cross-section for higher SERS signal, but also act as an insulation layer to form the gap junctions [108]. This method avoids the tradeoff between amount of RRM and the amount of spacer, and thus more RRM are embedded in the nanogap of the gap-enhanced particle. Compared with RRMs with one thiol group, RRMs with dithiol groups could form the strong Au-S bond on both core and shell sides, which leads to a very stable structure and thus a robust SERS signal. 1,4-benzenedithiol (BDT), 4,4'-biphenyldithiol (BPDT), 4,4'-terphenyldithiol (TPDT) are the dithiol RRMs used in forming gap-enhanced particle [130]. However, the three RRMs share very similar characteristic peaks and limit the palette of RRM for highly multiplexed

analysis. Thus, a modified method to synthesize gap-enhanced particle using RRM-based spacer, which is suitable for the RRMs with very distinguishable peaks, are strongly needed.

As mentioned above, a good xPOCT sensing system could provide information about multiple biomarkers simultaneously with the measurement on one spot. Thus, SERS tags with differentiable peaks should be developed and used for the different biomarkers. The selected RRMs should have at least one characteristic peak with minimal peak overlap with subsequent peaks. RRMs with relatively fewer peaks, which are usually small aromatic molecules, may be better to avoid signal overlap among the SERS tags [99]. Currently, many small-molecule RRMs have been used to develop multiplexed detection systems [132-137]. For example, 4-mercaptobenzoic acid (4-MBA) and 5,5′-dithiobis(2-nitrobenzoic acid) (DTNB) are a set of RRMs that are commonly utilized in duplex detection [132]. Further, 2-bromo-4-mercaptobenzoic acid (BMBA) can be distinguished from 4-MBA and DTNB [133]. Also, 4-nitrothiobenzoic acid (4-NTB) shows a distinguishable peak from 4-MBA [135]. It has been reported that 4-MBA, p-aminothiophenol (PATP), p-nitrothiophenol (PNTP), and 4-(methylsulfanyl) thiophenol (4-MSTP) can be applied in the detection of four analytes [136]. In addition, 2,7-mercapto-4-methylcoumarin (MMC), 2-mercapto-4-methyl-5-thiazoleacetic acid (MMTAA), and 2,3,5,6-tetrafluoro-4-mercaptobenzoic acid (TFMBA) can be distinguishable from 4-MBA and DTNB [137]. All of these RRMs have one thiol group that could bind to gold core or shell in a gap-enhanced particle. Therefore, we have a large palette of RRMs to make the gap-enhanced particle for multiplex detection. Specifically, an xPOCT system

for a triplex biomarker panel for MI needs three RRMs with clearly distinguishable signals. Therefore, three RRMs from the palette that are convenient for making the gap-enhanced particle and provide a strong signal are used.

1.6. Biorecognition element

1.6.1. Antibodies

Biorecognition element is a component in a sensing system for specifically recognize a target biomarker in a sample mixture [138]. There are different types of biorecognition elements, such as antibodies, nucleic acids, peptides, molecularly imprinted polymers, enzymes, phages, and whole cells (bacteria, fungi, yeast, animal cell) [139, 140].

Most of the current assays used antibodies as the recognition element [139]. Antibody is also called immunoglobulin, which is a protein composed of two heavy chains (H) and two light chains (L) [141]. The two heavy chains link to each other by disulfide bonds. Each light chain links to one of the heavy chains by disulfide bonds. A Y-shaped structure is formed when the heavy chains and the light chains are linked [141]. Each chain contains one amine-terminated variable (V) domain and one or more carboxy-terminated constant (C) domains [141]. The V domains are located at the tips of two arms of the Y-shaped structure, where the biomarkers bind at. The two binding sites at the tips of two arms of the Y-shaped structure are identical. The features on the V domain decide the specificity of the antibody to a biomarker [142]. The C domains of the heavy chains decide the functional activity of the antibody and how it interacts with effector molecules and

cells [142]. There are different types of immunoglobulins and they are classified by their difference in the heavy chain C domains [142]. Specifically, there are immunoglobulin M (IgM), immunoglobulin D (IgD), immunoglobulin G (IgG), immunoglobulin A (IgA), and immunoglobulin E (IgE) [141].

IgG is the immunoglobulin most often used in developing assays [140]. It has three C domains in its heavy chains. IgG has a molecular weight of around 150 kDa. The trunk of the Y-shaped structure of an IgG is called fragment-crystallizable fragment (Fc Fragment) [142]. The two arms of the Y-shaped structure of an IgG are called fragment antigen-binding fragments (Fab fragments) [142]. Fab fragments can be divided into a constant fragment (Fb) and a variable fragment (Fv). The Fv fragment is composed of a V domain of a light chain and a V domain of a heavy chain. The Fb fragment is composed of a C domain of a light chain and a C domain of a heavy chain [141]. The site on the biomarker/antigen that binds with the IgG is called epitope. The binding site on the IgG is called paratope.

Antibodies secreted by a single clone of B lymphocytes are called monoclonal antibodies. Antibodies secreted by various B lymphocyte clones are called polyclonal antibodies [143]. The antibodies used for developing assays are produced using procedures involved with animals. Monoclonal antibodies and polyclonal antibodies are obtained in slightly different ways. To obtain polyclonal antibodies, animals are given injections of the target biomarker/antigen. The injected antigen evokes an immune response and leads to the production of antibodies. An antigen may present many epitopes and can be recognized by many different B lymphocytes. Each B lymphocyte is activated

and produces antibodies [144]. Then, the blood of the animal is collected and purified to obtain the polyclonal antibodies [143]. Rabbit, mouse, goat, and sheep are often used in producing polyclonal antibodies [143]. To produce monoclonal antibodies, antigen-specific B lymphocytes are firstly generated by injection of the target biomarker/antigen in an animal. The generated B lymphocytes can be collected from the spleen. The generated B lymphocytes are then fused with myeloma cells to form hybridoma cells. The produced hybridoma cells are then cloned and selected. The selected hybridoma cells are then injected into the abdominal cavity of mice. The produced ascites are collected and purified to obtain the monoclonal antibodies [143]. Alternatively, cell culture of the hybridomas in vitro can also produce the monoclonal antibody [143]. The monoclonal antibody is more specific, homogeneous, and consistent, but is much more expensive and time-consuming. On contrary, the polyclonal antibody is less expensive and less time-consuming, but the specificity is poorer [144].

In an assay using a sandwich binding scheme, a pair of antibodies that bind to different epitopes of the biomarker is needed. Specifically, the antibody immobilized on a paper substrate is usually called a primary antibody. The antibody conjugated on the labels is usually called a secondary antibody. When there is a biomarker in a sample, a sandwich structure is formed after the primary antibody and the secondary antibody bind to the different epitopes of a biomarker molecule.

Antibody pairs have been used to develop sandwich assays for the detection of cTnI [145, 146], copeptin [147], and h-FABP [148, 149]. Antibodies have many advantages as a biorecognition element, such as a high affinity and high specificity to the

target biomarker [139]. For example, some antibodies for cTnI can reach low dissociation constants (K_d) ranging from 10 pM to 200 pM, which are suitable for high sensitivity assays [150]. Despite these advantages and the success of antibody in developing assays, antibodies have many limitations. Antibodies have limitations like low thermal stability, batch-to-batch variation, high cost, difficulty in engineering the sensitivity and specificity, long production time, using animals in production, poor reusability, and poor solubility [139, 140].

1.6.2. Aptamers

Nucleic acid, usually a single-stranded DNA (Deoxyribonucleic acid), can be used as the biorecognition element to detect a DNA or RNA (Ribonucleic acid) strand because of the natural affinity of the single-stranded DNA to its complementary strand [139]. Nucleic acid can also form a special secondary or tertiary structure due to its self-annealing properties [139]. The formed structure enables it to bind various types of biomarkers, such as proteins and small molecules. A nucleic acid ligand (single-stranded DNA or RNA) that can fold into a secondary or a tertiary structure and have a specific affinity to a target molecule is called aptamer [151].

Aptamer specific to a target biomarker is selected using systematic evolution of ligands by exponential enrichment (SELEX) [152], which is an in-vitro process. In a typical SELEX process, a library of oligonucleotides with various sequences are firstly mixed with target biomarkers functionalized magnetic beads. The oligonucleotides bound with the magnetic beads are collected. The oligonucleotides unbound or loosely bound

with the magnetic beads, which may have a low affinity to the target, are washed away [139]. The oligonucleotides bound with the magnetic beads are then eluted and amplified by polymerase chain reaction (PCR). The oligonucleotides product obtained in the first cycle is mixed with the target biomarker functionalized magnetic beads again. The second cycle repeats the same process as the first cycle. The cycle is continued to find a group of oligonucleotides with a high affinity to the target biomarker. Some counter selection cycles can be used to remove the low-specificity oligonucleotides. In counter selection steps, the obtained group of oligonucleotides is mixed with magnetic beads functionalized with some molecules that have a similar structure to the target biomarker. The oligonucleotides bound with the magnetic beads, indicating they have high affinity to other molecules, are removed. The rest oligonucleotides are collected and amplified. The counter selection steps can be repeated to ensure a good specificity of the oligonucleotides. Finally, the best oligonucleotide with high-affinity and high-specificity are selected as the aptamer for the target molecule [139]. Various aptamers have been discovered to recognize small molecules, proteins, and intact cells, with dissociation constants ranging from nanomolar to picomolar levels [153, 154]. Some aptamers have shown very good affinities to their target biomarkers, with dissociation constants ranging from picomolar to nanomolar [139].

Compared with antibodies, aptamers have several advantages. Aptamer has good thermal stability, good stability in a wide PH range, long shelf life, low-cost, efficient in-vitro screening, in-vitro automated synthesis, low batch-to-batch variation, and flexibility of direct modifications of functional groups and fluorophores on it [151, 155]. In addition,

aptamer, which is usually tens or close to a hundred bases, has a smaller size than antibodies. The smaller size of DNA largely avoids the steric problems for assays that require a close distance between the analyte and the sensor surface and largely increases the max density of recognition elements on a sensor surface[151]. In addition, aptamer has a better ability to be used in reusable sensors because it can be regenerated multiple times without loss of its binding affinity [151]. The good stability of aptamer is beneficial to reduce the cost of transportation and storage because it may not need to be transported and stored at a low temperature [139]. However, aptamers are vulnerable to nuclease, thus [139], extra cares to avoid exposure to nuclease should be taken when using aptamers.

Aptamers for detection of cTnI [156, 157]and h-FABP [158], have been reported in many studies. Aptamer for copeptin is lacking. In addition, there is a lack of pairs of aptamers for developing sandwich binding assays for h-FABP. One pair or aptamer are reported and used for the detection of cTnI [157]. The pair of aptamers for cTnI has dissociation constants (K_d) of 270 pM and 317 pM, indicating a strong binding affinity to cTnI. Thus, this aptamer pair can be used to develop a sensitive sandwich binding assay for cTnI.

1.7. Paper based microfluidic device

A POCT sensing system for the detection of cardiac biomarkers for MI could make the diagnosis of MI more feasible on-site, especially for resources-limited settings. To develop a POCT sensing system, a platform that holds the sample and allows the reagents to react with the sample is needed. As mentioned in the REASSURED criteria, user-

friendliness, environmentally friendliness, and affordability are important for an ideal POCT. An appropriate platform is needed to achieve these criteria.

Within the past decades, microfluidic technology has been widely used in different assays because of its potential for miniaturization, integration, and automation [159]. Compared with microfluidic devices based on polydimethylsiloxane, silicon, glass, or other polymers [160], paper-based microfluidic device is good for POCT because it has the following advantages: (1) it is made from ubiquitous, lightweight, and cheap cellulosic material; (2) paper material is more environmentally friendly than other materials, like plastic; (3) it can be used as a disposable platform due to their low cost; (4) it allows reagents to be stored in an active form within the fiber network; and (5) liquids are transported using capillary forces without the need for external forces [159-161].

Lateral flow assay strip is one type of paper-based microfluidic devices. It has been widely studied in the research field and is used in many commercially available rapid diagnostic tests [69, 162-165]. Lateral flow assay strip has several advantages, such as its simplicity of the device preparation, cost-effectiveness, small sample volume, and simple operational steps [166]. Generally, a lateral flow assay strip is composed of a sample pad, a conjugate pad, a nitrocellulose paper with a test line and a control line, and a waste pad (as shown in Figure 1.1). The sample pad can hold the input samples, prevent sample flooding, and release the sample in a consistent and even way. The sample pad can also act as a filter or be combined with another paper-based filter to remove unwanted components in the sample (such as red blood cells in the whole blood). In addition, some reagents to improve sample flow or reduce non-specific binding can be dry-stored in the

sample pad. The conjugate pad is usually stored with labels functionalized with recognition elements, like gold nanoparticles functionalized with antibodies. Some additional reagents to preserve the antibodies, improve sample flow, and/or reduce non-specific binding are dry-stored in the conjugate pad. The nitrocellulose paper is often dispensed with two lines of recognition elements. One line is a test line, which has the recognition element that specifically binds to the target biomarker. The other line is a control line, which has the recognition element that binds to the functionalized labels. The waste pad, or called adsorption pad, is used to wick waste solution, drive the sample to flow, and prevent contaminant of the test line due to back-flow of the waste solution.

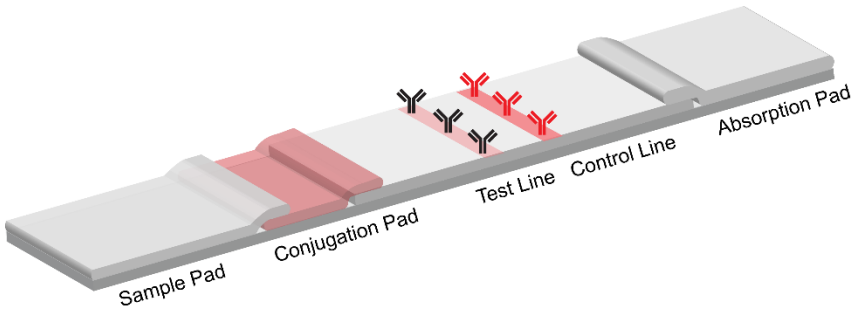

Figure 1.1 Lateral flow assay strip structure.

When introducing a sample, it is firstly absorbed by the sample pad. The sample keeps flowing into the conjugate pad, where it resuspends the functionalized labels. If the sample has target biomarkers, the target biomarkers will react and bind with the recognition elements on the functionalized labels. The mixture of the sample and the labels

then flows into the nitrocellulose paper. On the test line, the labels bound with the target biomarker are captured by the recognition elements on the line. The more target biomarkers present in the sample, the more labels are captured on the test line. Labels not bound with the target biomarker flow to the control line and are captured on the control line. Finally, the absorption pad absorbed the excess fluid. The concentration of the target biomarker is correlated to the number of labels captured on the test line.

In conventional lateral flow assays, the test line is usually read as a visible line or an invisible line by the naked eye for qualitative results [165]. Nowadays, semi-quantitative or quantitative lateral flow assay strips read by additional readers have been developed to detect different biomarkers [165]. Labels and readers based on electrochemical (amperometry, cyclic voltammetry, impedimetry, electro-chemiluminescence), optical (colorimetric, fluorescence, SERS, chemiluminescence), magnetic, and thermal (thermal imaging, photoacoustic, speckle imaging) modalities, have been designed [165]. Because of the strong enhancement in the SERS signal, the SERS modality is suitable for high-sensitivity assays without using additional amplification steps [165].

Notably, in most lateral flow assay strips, samples flow continuously in a straight channel with the original permeability, porosity, pore size, width, thickness of the paper [167-175]. The well-defined structure of a lateral flow assay strip (a sample pad, a conjugate pad, a nitrocellulose paper, and a waste pad) makes the development of assays for new biomarkers simple and easy. Despite the advantages and the achievements of

lateral flow assays, lateral flow assays show large limitations in implementing complicated operations and multiple reaction steps, and controlling flow rate.

Microfluidic paper-based analytical devices (μPADs) is a platform comprised of hydrophilic and hydrophobic channel networks in papers [176, 177]. In 2007, the first microfluidic paper-based analytical device (μPAD) for chemical analysis was reported [178]. Since then, μPAD have become an important area and shown large potential to connect the microfluidic technology with the needs of a real-world product. Customized microfluidic channels can be designed on a paper substrate for complicated function [166]. Various operations normally used in assays in wells, such as mixing, sequential addition, splitting, separation, and filtration, can be achieved [68]. Thus, using μPAD as a platform has a better flexibility than lateral flow assays in transforming high-performance assays that used to be reserved at laboratory settings into point-of-care settings.

In high-performance assays, it is desired that the incubation time/reaction time can be tuned depending on the specific biomarkers. For instance, a longer reaction time may be used for a high-sensitivity assay; a shorter reaction may be used for a time-sensitive biomarker. Different methods can be used to increase the reaction time to achieve high-sensitivity assays. One simple method is to change the geometries of the channel, such as lengths, widths, or thickness [179-184]. However, decreasing flow rate in these systems requires a long, wide, or thick channel, which requires a large volume of sample. To decrease the flow rate more efficiently, permeability in papers can be tuned using materials, such as wax [185-187], agarose [188], sucrose [189, 190], and trehalose [191],

or varying the UV exposure time on TiO_2-coated paper [192], or carving channels on a paper surface [193], or covering a paper with PET sheets with triboelectric charges [194].

In addition, sequential addition samples or reagents in multiple steps is very often used in high-performance laboratory assays. To achieve these multi-step assays at POC, μPADs with different designs have been developed. In some designs, fluidic flow is paused or started by manually separate or connect two channels by sliding a layer [195], rotating a layer in μPADs [196, 197], adding solvent to dissolve a wax valve [198], and folding or unfolding papers [199, 200]. In contrast to these designs need manual activation [195-204], an automatic system is easier to use especially for untrained users [205, 206] and works better for high-throughput analysis with limited personnel. Different automatic systems for multi-step assays have been achieved by using electroosmotic pumping [207], using electrowetting layers [208, 209], melting wax blocks [210], actuating a magnetized cantilever [205, 211], or heating hexadecyltrimethylammonium bromide [212]. However, auxiliary instruments are needed in these methods to apply the pressure, voltage, electromagnetic force, or heat. These auxiliary instruments add more cost on the expense per test, which contradicts the affordability criterion of an ideal POCT.

To achieve automatic multi-step assays without using auxiliary instruments, designs to create temporal differences of different fluids in reaching the reaction area have been developed. Specifically, multiple fluids (e.g. sample, washing buffer, enzyme solution, labeling solution) are loaded in different channels [181, 182]. These paper channels have different lengths, widths, or thicknesses, and thus the flow rates in each channel are different. The fluid that firstly reaches the reaction zone reacts with the

recognition elements. When the second fluid reaches the reaction zone, it reacts with the chemicals already in the reaction zone. Similar processes are repeated for the followed fluids. However, as mentioned above, controlling flow rate by geometry needs a tradeoff between available sample volumes and the temporal differences between steps.

Dissolvable materials can be used to increase the efficiency of generating temporal difference while retaining channel geometry [190, 191, 213-215], but the dissolvable materials themselves may contaminate the samples. More attempts to achieve automatic multi-step assays without using dissolvable materials have been made. For example, paraffin wax [216], pressurized papers [217], papers with carved channels on their surface [193], and folded paper actuators [218], can be used. However, these designs show a limited capability to achieve automatic multi-step high-sensitivity assays in an efficient and robust way. Therefore, a new μPAD design that is robust and efficient and can achieve automatic multi-step high-sensitivity assays for the detection of biomarkers, like cTnI, copeptin, and h-FABP, is highly needed.

Among the three biomarkers for MI, cTnI is the one with the lowest molar concentrations in human blood. Thus, the development of a high-sensitivity assay for the detection of cTnI is the most challenging. Table 1.2 summarizes some recent high-sensitivity research platforms for the detection of cTnI for POCT applications. As shown in Table 1.2, non-paper-based platforms and multiple manual processes are still needed in these reported platforms. Therefore, a high-sensitivity and automatic microfluidic paper-based assay for the detection of cTnI is still needed, and using aptamer as the recognition element is of great interest.

Table 1.2 Research platforms for detection of cardiac troponin I

No.	Limit of Detection (ng/mL)	Paper Based Platform? (Y/N)	Steps in assay	Detail of the steps	Methods to finish multiple steps	References
1	0.01	Y	4	mix sample with gold nanoparticle conjugated magnetic bead, incubate, magnetic separation, adding PBS, load sample in paper strip	Manual operation	[219]
3	0.001	N	3	mix antibody with sample, incubate, load in device and react with microbeads, incubate, wash	Use voltage source to control the fluid in the device, and need manual operation	[220]
4	0.000394	N	5	load sample, incubate, add elution buffer, wash 3 times	Use a controller to control the fluid in the microfluidic channel	[221]

1.8. Summary

Myocardial infarction (MI) is related to myocardial necrosis due to extended ischemia in cardiomyocytes. It is often caused by thrombosis that obstructs blood flow to the heart. The population affected by MI and the impact of MI are problematic. Specifically, the prevalence and incidence of MI are not low and the mortality of MI is

high. Notably, MI affects males more than females, affects elder groups more than younger groups, and affects some ethnic groups more than others. In addition, socioeconomic status is also related to recurrent MI, mortality, and MI incidence. CABG, PCI, and pharmacological approach, ranked from more costly to less costly, are the treatments often used in MI. A short time length between the onset of symptoms and treatment is desired to make more therapy strategies feasible and to increase the clinical outcomes. Timely diagnosis of MI is essential for determining and implementing the treatment in a timely manner. In addition, early rule-out of non-MI patients and the consequent early discharge help to avoid the prolonged monitoring and the high cost of staying in hospitals.

Cardiac biomarker tests are important for the diagnosis of MI. cTnI is a well-established cardiac biomarker for MI. Addition of h-FABP and copeptin to cTnI forms a good biomarker panel for improved performance in the diagnosis of MI and a rapid rule-out of the non-MI patients. Quantitative assays for these biomarkers are important. Successful assays should cover 5-16.8 ng/mL range for the detection of h-FABP, cover 0.004-0.056 ng/mL for the detection of copeptin, and cover 0.01-0.1 ng/mL for the detection of cTnI. The detection time of the assay should be within 60 minutes. To improve patients' access to diagnostic tests, especially in resource-limited settings, it is of great need to develop a cost-effective, user-friendly, and simple-to-use xPOCT sensing system for the biomarker panel. An assay that meets the above requirements is lacking and thus it is of great importance to develop one.

This work describes the development of a multiplex assay for the detection of a biomarker panel composed of cTnI, copeptin, and h-FABP. A sensitive optical modality, SERS, was used to transduce the sensing signal. SERS tags, composed of RRM and metallic nanostructure, were designed and used to generate strong and stable SERS signals with narrow characteristic peaks. Nanostructures, like silica-shell encapsulated gold nanosphere and gold-core gold-shell gap-enhanced particle, were developed. The protective shell, either the silica-shell or the gold-shell, could improve SERS signal stability because it prevented the RRM from dissociating and prevented interfering molecules in a sample matrix from adsorbing on the surface of the metallic nanostructures. MGITC, a molecule with electronic transitions near 638 nm, was used as an RRM to achieve the resonance condition and generate a strong SERS signal. Alternatively, the nanogap interior of gap-enhanced particles could also largely enhance the SERS signal of any RRMs embedded. To overcome the limitation of currently reported methods in the synthesis of gap-enhanced particles, a modified method to synthesize gap-enhanced particles using an RRM-based spacer was developed.

To achieve multiplex detection, instead of using spatial separation, resolving peaks from different biomarkers in a single test line was used because it could reduce assay time, manufacturing cost, and signal reading time. Because an xPOCT system for a cTnI, copeptin, and h-FABP, needs three RRMs with clearly distinguishable peaks, three SERS tags with differentiable peaks were synthesized. Three RRMs that have at least one characteristic peak with minimal peak overlapping with subsequent peaks were selected.

The synthesized three SERS tags were then used in the multiplex detection to resolve the signal from each biomarker in a single test line.

Aptamers were used as the recognition element for the detection of the target biomarker. Aptamers have advantages, such as good thermal stability, good stability in a wide PH range, long shelf life, low-cost, efficient in-vitro screening, in-vitro automated synthesis, low batch-to-batch variation, and flexibility of direct modifications of functional groups and fluorophores on it. Alternatively, antibodies, which usually have a high affinity and high specificity to the target biomarker and are more commercially available, could also be used as the recognition element.

Paper-based microfluidic devices were used to ensure the assays are cost-effective, user-friendly, and simple to use. μPADs have a good ability in transforming high-performance assays that used to be reserved at laboratory settings into point-of-care settings. A μPAD was designed to achieve automatic multi-step assays without using auxiliary instruments. In addition, a localized dissolvable delay was designed and added in the μPAD to decrease fluid flow rate and improve assay performance. Alternatively, a lateral flow assay strip, which is simple to prepare and is easy for mass production, could be used to implement the assay.

2. APTAMER-BASED SURFACE ENHANCED RESONANCE RAMAN SCATTERING ASSAY ON A PAPER FLUIDIC PLATFORM FOR DETECTION OF CARDIAC TROPONIN I *

2.1. Introduction

Myocardial infarction (MI) is a cardiovascular disease related to myocardial necrosis due to a reduction of blood supply to the heart [222]. MI affects a large population, and the overall prevalence for MI is 3% in US for adults ≥20 years of age between 2011 and 2014 [223]. Moreover, mortality rate from MI is a problem and it is estimated that ~14% of the people who experience an MI will die of it [223]. Cardiac troponin I (cTnI) is a primary biomarker for diagnosis of MI [224, 225] and the clinical cut-off of cTnI for diagnosis of MI is determined by the 99th percentile concentration [226]. Specifically, it was reported that the range of clinically acceptable concentrations of the cTnI was 0.01–0.1 ng/mL [227, 228]. Compared with the conventional method of sending samples to a central lab, point-of-care (POC) testing for cTnI can help diagnosis of MI in the field [229, 230], which allows high-risk patients to be treated more rapidly and low-risk patients to be released in a more timely fashion [231]. This enables the health care provider to apply treatment rapidly, which requires a less invasive intervention procedure and also leads to much lower mortality [232-234]. Thus, it is of great interest to develop a sensitive POC method for detection of cTnI in the clinically relevant range.

---

*Reprinted with permission from Dandan Tu, Allison Holderby, Gerard L. Coté, "Aptamer-based surface-enhanced resonance Raman scattering assay on a paper fluidic platform for detection of cardiac troponin I," Journal of Biomedical Optics, 25(9), 097001 (2020). https://doi.org/10.1117/1.JBO.25.9.097001.

Recently, various POC testing systems for cTnI have been developed [70, 71, 74, 83, 123, 235-246], however these systems have limitations in cost-effectiveness (especially in the cost of the disposable cartridges), poor sensitivity, or limited stability of the recognition element. Paper-based sensing systems have demonstrated potential as a POC platform to implement assays due to the merits of paper (e.g. abundance, low-cost, ease of disposability) [169, 247]. Surface enhanced Raman spectroscopy (SERS), a sensitive optical method that provides good performance for detection of trace analytes in a sample [248], has been used for developing assays for detection of cTnI [70, 71, 237-239]. Paper-based SERS assays, in particular, have been developed for sensitive detection of cTnI [74, 123, 236, 240, 241]. However, these assays use antibodies as the recognition element [70, 71, 123, 237-241], which has limitations due to selection difficulties, high costs of production, and stability issues [249]. Aptamers, on the other hand, can be used as the recognition element for low-cost POC testing due to their nontoxicity, thermal stability, tolerance to a range of pH levels, and long shelf life [155, 250]. Moreover, compared with SERS, surface enhanced resonance Raman scattering (SERRS) can provide a 10~100 fold higher signal [251], which can enhance the transduction signal received from low quantities of an analyte. To synthesize a SERRS active particle, a Raman reporter molecule (RRM) that has the frequency of the electronic transition close to the frequency of the excitation light is needed [115]. Malachite green isothiocyanate (MGITC), a molecule with electronic transitions near 638 nm [116], was thus chosen as a good RRM to provide the SERRS signal.

In this paper, an aptamer-based assay on paper platform using SERRS active particles for detection of cTnI was developed. The hydrodynamic size distribution and the zeta potential of synthesized particles were characterized, and characteristic peaks of the SERRS spectrum were demonstrated. The performance of the developed aptamer-based assay on a paper platform using SERRS active particles for the quantitative detection of cTnI was evaluated. Selectivity of the assay against interfering molecules, stability of the assay over 10 days, and the performance of the assay in human serum were also evaluated.

2.2. Materials and methods

2.2.1. Combined system configuration

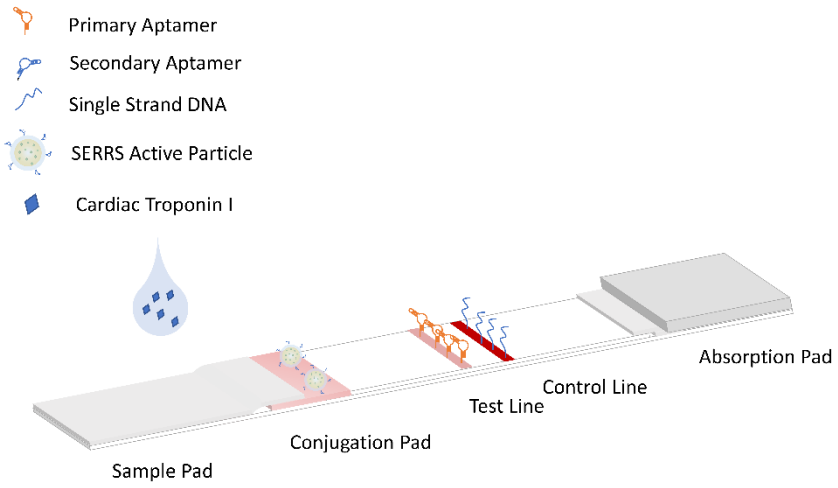

Figure 2.1 Schematic of the aptamer-based assay on a paper platform using SERRS active particles for detection of cTnI.

Configuration of the developed aptamer-based assay on a paper platform using SERRS active particles for detection of cTnI is shown in Figure 2.1. SERRS active particles functionalized with a secondary aptamer of cTnI was stored in a conjugation pad. To measure a sample with cTnI, the sample was introduced onto the sample pad followed by introduction of a running buffer. The sample resuspended the SERRS active particles and flowed to test line region. The cTnI formed a sandwich binding of the SERRS active particle, the cTnI protein, and the aptamer on the test line. Excess SERRS active particles flowed to the control line region and bound with DNA on the control line. In this configuration, the SERRS signal would increase with the amount of SERRS active particle bound on the test line, which is a direct result of an increase in the concentration of cTnI in the sample.

2.2.2. Materials and instruments

Cardiac troponin I was purchased from GenScript (Piscataway, New Jersey, USA). The sequence of aptamers for the cTnI assay was reported in previous journal papers [156, 157]. In this work, the primary aptamer of cTnI is 5'-biotin-TTTTTTCGTGCAGTACGCCAACCTTTCTCATGCGCTGCCCCTCTTA-3'. The secondary aptamer of cTnI is 5'-amine-spacer 18-spacer 18-CGCATGCCAAACGTTGCCTCATAGTTCCCTCCCCGTGTCC-3'. The sequence of the DNA strand on the control line is 5'-biotin-TTTTTTGGACACGGGGAGGGAACTATGAGGCAACGTTTGGCATGCG-3'. The DNA strands for cTnI assay were purchased from Integrated DNA Technologies (Iowa,

USA). Whatman grade 1 chromatography paper and Immunopore FP nitrocellulose paper were purchased from Cytiva (Formerly GE Healthcare Life Sciences, Marlborough, Massachusetts, USA). Glass fiber (GFCP000800) was purchased from EMD Millipore (Burlington, Massachusetts, USA). Thick blot filter paper was purchased from Bio-Rad (Hercules, California, USA). The mounting adhesive card was purchased from Michaels (Irving, Texas, USA). Milli-Q ultrapure water (18.2 MΩ cm^{-1}) was used in all the procedures. (3-triethoxysilyl)propylsuccinic anhydride (TEPSA) was purchased from Gelest (Morrisville, Pennsylvania, USA). N-hydroxysulfosuccinimide sodium salt (Sulfo-NHS) and N-ethyl-N'-(3-dimethylaminopropyl) carbodiimide hydrochloride (EDC) were purchased from CovaChem (Loves Park, Illinois, USA). Malachite green isothiocyanate was purchased from Thermo Fisher Scientific (Waltham, Massachusetts, USA), and methoxy-poly(ethylene glycol)-thiol (mPEG-SH, 10 kDa) was purchased from Nanocs (New York City, New York, USA). Human serum was purchased from Innovative Research (Novi, Michigan, USA). Other chemicals were purchased from Sigma Aldrich (St. Louis, Missouri, USA).

Absorbance spectra of particles were measured on a Tecan Infinite 200 Pro (Tecan, Switzerland) microplate reader. Transmission electron microscopy (TEM) images were acquired on a JEOL JEM-2010 (JEOL, Japan). The zeta potential and hydrodynamic size of the particle were measured on a Zetasizer Nano ZS90 (Malvern, U.K.). All SERRS spectra were collected using an Ocean Optics portable Raman spectrometer (IDR-MINI) with a 638 nm laser (40 mW laser and 3 s exposure time). Three measurements were taken on one test line, moving from the left side to the right side, and the SERRS signal of the

test line on this strip was the average of the intensity from these spectra. All spectra were baseline corrected.

2.2.3. Nanoparticle synthesis

A seed-mediated synthesis method was used to synthesize the gold nanoparticles (AuNPs) with a size of around 60 nm [252]. Firstly, 75 mL of 2.2 mM sodium citrate in water was heated until boiled. Secondly, 0.5 mL of 25 mM chloroauric acid solution was injected. The mixture was stirred for 30 min, followed by adjusting the temperature to 90 °C. Thirdly, 0.5 mL of 25 mM chloroauric acid solution was injected, and the mixture was stirred for 30 min. This step was repeated one time, and then the particle solution was diluted by extracting 27.5 mL of solution and adding 26.5 mL of water and 1 mL of 60 mM sodium citrate. Fourthly, 0.5 mL of 25 mM chloroauric acid solution was injected, and the mixture was stirred for 30 min. Steps two through four were repeated until the size of the particle reached the target size and the particle solution was cooled down before using.

Following AuNPs synthesis, MGITC was functionalized on AuNPs as a RRM, and the MGITC modified AuNP (MGITC/AuNP) was then encapsulated in a silica shell. The process is shown in Figure 2.2. Specifically, 50 μL of 20 μM MGITC solution was mixed with 10 mL of AuNPs in a glass vial and the mixture was kept shaking for 15 min. As a stabilizing component, 12.4 μL of 1 mM mPEG-SH was then added and the mixture was kept shaking for 15 min. After centrifuging (1500 rcf, 20 min), the particle was

resuspended in 1 mL of 2-propanol. To begin the silica shell formation, 3.6 mL of water and 19.7 µL of 0.1 mM (3-mercaptopropyl)trimethoxysilane (MPTMS) solution was added to the particle solution. After shaking for 15 min, 9 mL of 2-propanol and 250 µL of ammonium hydroxide were added. Then, 100 µL of tetraethyl orthosilicate (TEOS) solution (1% in 2-propanol) was added and was kept rotating. After 30 min, another 100 µL of TEOS was added, and the mixture was kept rotating overnight. The resulting solution was centrifuged (1000 rcf, 20 min) and washed three times with ethanol. Finally, the synthesized silica shell MGITC modified AuNP (silica/MGITC/AuNP) were resuspended in ethanol.

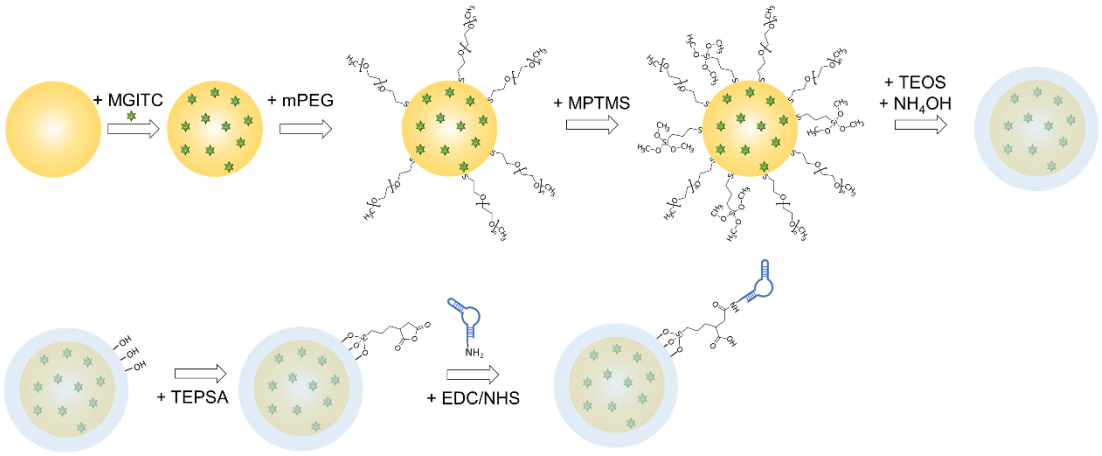

Figure 2.2 Process to synthesize the aptamer/silica/MGITC/AuNPs.

2.2.4. Nanoparticle functionalization with aptamer

As shown in Figure 2.2, a secondary aptamer was covalently bound on the surface of the silica/MGITC/AuNP to form an aptamer functionalized silica shell MGITC modified AuNP (aptamer/silica/MGITC/AuNP). Before functionalization, the secondary aptamers were heated to 85℃ for 5 min and slowly cooled to room temperature. Then, 1 mL of silica/MGITC/AuNP was mixed with 0.3 mL of water and 0.2 mL of 0.2 M TEPSA, followed by shaking overnight. The mixture was then centrifuged (1500 rcf, 15 min) and resuspended in 0.2 mL of phosphate buffer (PH 7.4) followed by mixing with 75 µL of 50 mM Sulfo-NHS, 75 µL of 200 mM EDC, and 80 µL of 10 µM amine functionalized aptamer. The mixture was sonicated and left shaking for 1 hour followed by addition of 150 µL of 0.2 M ethanolamine (PH 8.6). The mixture was kept shaking for 1 hour and the formed aptamer/silica/MGITC/AuNP was sonicated, centrifuged (1000 rcf, 15 min), and washed with phosphate buffer (PH 7.4).

2.2.5. Preparation of an aptamer-based paper strip

As shown in Figure 2.1, the aptamer-based paper strip is composed of a sample pad, a conjugation pad, a nitrocellulose paper with a test line and a control line, and an absorption pad. The sample pad was prepared by cutting a Whatman grade 1 chromatography paper into a strip with a width of 15 mm, soaking it in 0.05 M Tris buffer (PH 7.6, 0.15 M NaCl) with 0.25% Triton X-100, and drying it at 45 °C for 1 hour. The conjugation pad was prepared by soaking the glass fiber (8 mm width) in a buffer (1%

bovine serum albumin, 0.5% tween, and 5% sucrose), drying it at 45 °C for 1 hour, soaking the aptamer/silica/MGITC/AuNP solution, and drying it at 45 °C for 1 hour.

A primary aptamer of cTnI and a single strand DNA, which was the reverse complimentary DNA strand of the secondary aptamer of cTnI, were immobilized on the nitrocellulose paper to form a test line and a control line, respectively. Biotin-streptavidin interaction was used to immobilize the aptamer and the single strand DNA on the nitrocellulose paper. Before immobilization, the primary aptamers were heated to 85°C for 5 min and slowly cooled to room temperature. Then, 1 mL of 10 μM biotinylated primary aptamer was mixed with 40 μL of 2.5 mg/mL streptavidin, and the mixture was kept shaking for 1 hour. The aptamers unbound to streptavidin were then washed by centrifugation (4300 rcf, 20 min) using a Nanosep (30kDa). The produced primary aptamer/streptavidin conjugate was resuspended in 400 μL of phosphate buffered saline (PBS). The same process was repeated to form the single strand DNA/streptavidin conjugate. The nitrocellulose paper was cut into a strip with a width of 22 mm and was dispensed with the primary aptamer/streptavidin and the single strand DNA/streptavidin to form the test line and control line, respectively. The nitrocellulose paper was dried at room temperature overnight. To block the remaining adsorption sites on the nitrocellulose paper, the nitrocellulose paper was immersed in 1% poly(vinyl alcohol) (PVA, molecular weight of 9000-10000) aqueous solution for 30 min and dried at 45 °C for 30 min.

The absorption pad is composed of a Whatman grade 1 paper (5 mm width) and a thick blot filter paper (25 mm width). The grade 1 paper is softer than the thick blot paper and it has the ability to wick fluid laterally. The thick blot filter paper can absorb large

volumes of liquid. In this design, the grade 1 paper was added to provide good contact between the nitrocellulose paper and the thick blot paper and ensure good wicking of waste solution. The sample pad, conjugation pad, functionalized nitrocellulose paper, and absorption pad were assembled on an adhesive card with 2 mm overlap between the pads. Finally, the assembled paper was cut into paper strips with a width of 4 mm and stored in a petridish sealed with parafilm.

2.2.6. Response of the assay

Different concentrations of cTnI (0, 0.01, 0.03, 0.05, 0.1 ng/mL) in PBS (PH 7.4) were measured using the developed aptamer-based paper strip. To test a sample, 25 μL of the sample was dropped on the sample pad, and then 50 μL of running buffer (PBS with 0.25% tween) was deposited on the sample pad after positioning the paper strip vertically. After all solution flowed to the end of the paper and was wicked by the absorption pad, a portable Raman spectrometer was used to measure the SERRS signal on the test line. To collect the SERRS signal, the paper strip was put in a strip holder (shown in Figure 2.3). The control line was aligned with an indicator on the strip holder. After positioning the strip holder on the platform, SERRS signal was collected using the Raman spectrometer. Tests for each concentration were performed in triplicate.

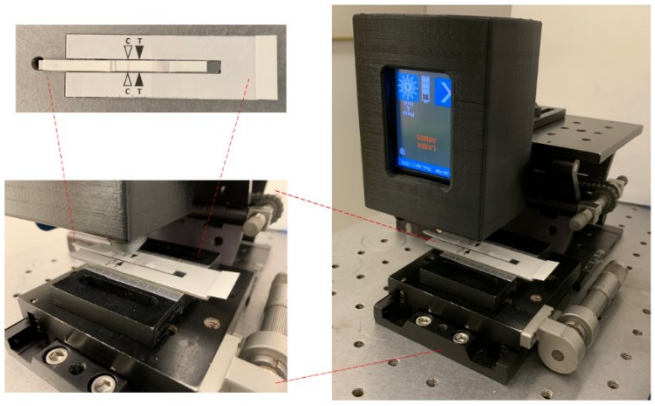

Figure 2.3 Setup of the portable Raman spectrometer to measure SERRS signal from a paper strip.

2.2.7. Selectivity of the assay

Selectivity of the aptamer-based paper strip was evaluated by comparing the SERRS signal to 0.1 ng/mL of cTnI, and potential confounders namely: c-reactive protein (CRP), heart-type fatty acid-binding protein (h-FABP), and B-type natriuretic peptide (BNP). The 25 µL sample of either 0.1 ng/mL of cTnI, CRP, h-FABP, or BNP was dropped on the sample pad, and then 50 µL of running buffer (PBS with 0.25% tween) was applied on the sample pad after positioning the paper strip vertically. The paper strip wicked the samples and the solution flowed down the paper and was wicked by the absorption pad. The portable Raman spectrometer was then used to measure the SERRS signal on the test lines. Tests for each sample were performed in triplicate. One-way analysis of variance (ANOVA) was performed in OriginLab to determine whether the response to cTnI were significantly different from the response to these potential confounders.

2.2.8. Stability of the assay

The paper strip was stored in a petridish sealed with parafilm at room temperature. Stability of the aptamer-based paper strip was evaluated by recording the response of the paper strip to 0.03 ng/mL of cTnI over 10 days. Specifically, the response at Day 1, Day 2, Day 4, Day 7, and Day 10 were collected. Tests for each day were performed in triplicate.

2.2.9. Application for the analysis of the serum sample

The following test was implemented to evaluate the performance of the aptamer-based paper strip for detection of cTnI in a complex biological sample matrix. Without any pre-treatment, human serum was spiked with cTnI to reach a concentration of 0.03 ng/mL and 0.05 ng/mL of cTnI. The cTnI spiked serum samples were then used to test the developed aptamer-based paper strip. Specifically, 25 μL of sample was dropped on the sample pad, and then 50 μL of running buffer was applied on the sample pad after positioning the paper strip vertically. The paper strip wicked the samples and the solution flowed down the paper and was wicked by the absorption pad. The portable Raman spectrometer was then used to measure the SERRS signal on the test lines. Tests for each sample were performed in triplicate.

2.3. Results and discussion

2.3.1. Characterization of particle

Absorbance spectrum was used to confirm the synthesis and AuNPs. Figure 2.4(a) shows the absorbance spectrum of the synthesized AuNPs, in which the surface plasmon resonance peak was shown around 536 nm. The RRM MGITC, with electronic transitions near 638 nm [116], was used to provide the SERRS signal. Adsorption of MGITC reduced the electrostatic stability of the MGITC/AuNP particle, which could lead to aggregation of the particles during the processing steps, thus mPEG-SH was used to stabilize the particle. In addition, the binding force in Au-isothiocyanate interaction when adsorbing the MGITC to AuNP is weak, which can lead to fluctuations in the signal [253]. Encapsulation of a silica shell was an efficient way to prevent reporter molecules from desorption from the particle surface [254]. Thus, the MGITC/AuNP was encapsulated in a silica shell to produce a stable and reproducible SERRS signal. MPTMS was used to functionalize the surface of the MGITC/AuNP with an ethoxy group to facilitate the adsorption of TEOS [255]. TEOS and ammonium hydroxide were added to form a silica shell. As shown in Figure 2.4(a), there was a red shift of the absorbance peak of the synthesized silica/MGITC/AuNP compared with AuNPs, indicating the modification of MGITC and silica shell.

The overall morphology of synthesized silica/MGITC/AuNP was observed from the TEM image shown in Figure 2.4(b). A clear silica shell encapsulating the gold core in the synthesized silica/MGITC/AuNP particles could be observed. It is also seen that almost all particles had an individual RRM functionalized gold nanoparticle encapsulated

in a silica shell, confirming the effect of mPEG-SH used to stabilize the particle and to prevent the particle from aggregating during the process used for particle encapsulation.

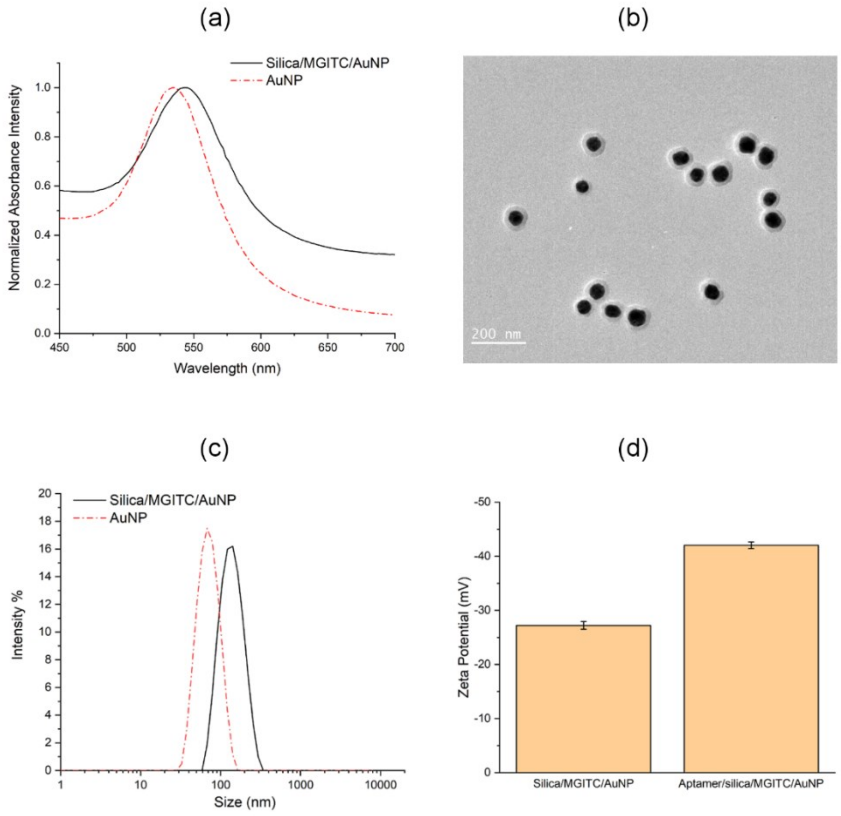

Figure 2.4 (a) Absorbance spectrum of synthesized AuNPs. (b) TEM image of silica/MGITC/AuNPs. (c) Size distribution of AuNPs and silica/MGITC/AuNPs. (d) Zeta potential of silica/MGITC/AuNPs before and after functionalization of the secondary aptamer.

Figure 2.4(c) shows the hydrodynamic size distribution of the synthesized AuNPs and silica/MGITC/AuNP particles. As can be seen, the synthesized AuNPs have a mean size of 64 nm. Compared to a small size AuNP, a large size AuNP was used here to provide better efficiency for SERS with excitations at 630-650nm [116]. As shown in Figure 2.4(c), after functionalizing MGITC and growing a silica shell, the size of the particle increased to around 129 nm. Moreover, the uniformity in size distribution of silica/MGITC/AuNP particles were close to that of the bare AuNPs, indicating the thickness of the formed silica shell was consistent.

To form an aptamer/silica/MGITC/AuNP, TEPSA was modified on the surface of the silica/MGITC/AuNP particle. The succinic anhydride group of TEPSA was hydrolyzed into two carboxyl groups, which was then activated by EDC and Sulfo-NHS and reacted with the amine group of the secondary aptamer. After this process, the secondary aptamer was functionalized on the silica/MGITC/AuNP particle by an amide bond. Figure 2.4(d) shows the zeta potential change before and after functionalization of the secondary aptamer. After the functionalization, the zeta potential of the particles remained negative and had an increase in value, which was due to the strong negative charge of the aptamer.

The SERRS spectrum of the synthesized aptamer/silica/MGITC/AuNP particle was measured and is shown in Figure 2.5, and its characteristic peaks were from the vibrational modes of MGITC. The three strong characteristic peaks of the aptamer/silica/MGITC/AuNP particle were 1173 cm^{-1},1368 cm^{-1}, and 1617 cm^{-1}.

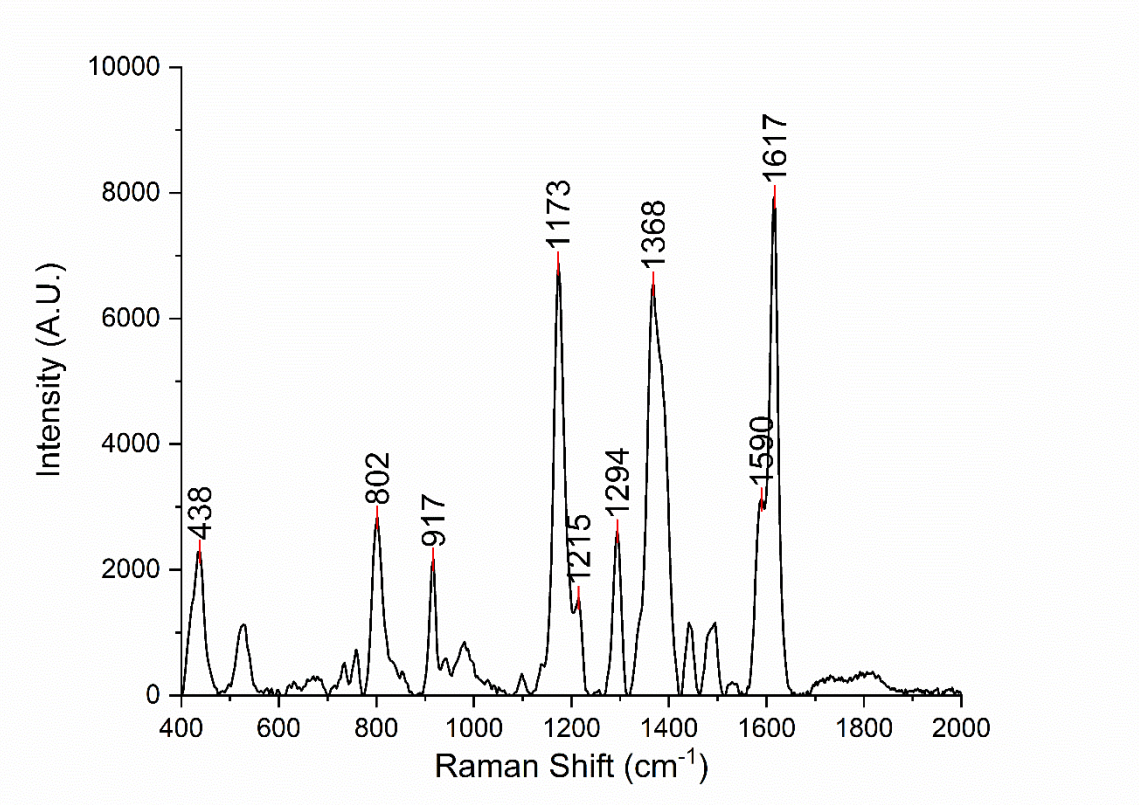

Figure 2.5 SERRS spectrum of the aptamer/silica/MGITC/AuNPs.

2.3.2. Response of the assay

The developed aptamer-based paper strip was used to measure different concentrations of cTnI. To measure a sample with cTnI, 25 µL of the sample was introduced onto the sample pad of the paper strip. The sample resuspended the aptamer/silica/MGITC/AuNPs and the cTnI started to bind with the NPs. Then, 50 µL of the running buffer was introduced to drive the cTnI and the particle to flow to the end of the paper. The paper strip was positioned vertically when wicking the running buffer to

achieve a low flow rate, which provided a longer reaction time for cTnI, the aptamer/silica/MGITC/AuNPs, and the primary aptamer on the test line. When cTnI was captured by the primary aptamer on the test line, a sandwich binding of the aptamer/silica/MGITC/AuNPs, the cTnI protein, and the primary aptamer was formed. The free aptamer/silica/MGITC/AuNPs not bound with cTnI passed the test line, flowed to the control line, and bound with the single strand DNA on the control line. The more cTnI present in the solution, the more aptamer/silica/MGITC/AuNPs were captured on the test line, and thus there was a stronger SERRS signal. By measuring the SERRS signal, the concentration of target molecule was quantitatively determined. It took around 10 minutes for the sample to initially flow down the paper and, in order to increase the sensitivity by allowing more particles and sample to interact, around 40 mins for the paper strip to wick both the sample and the running buffer to the absorption pad.

Images of the paper strips after loading different concentrations of cTnI are shown in Figure 2.6(a). It can be seen that the control line was easy to see with one's bare eyes. The test line was not as strong nor as easy to read as the control line, especially at the lower concentrations. However, using a portable Raman spectrometer to measure the signal from the test line quantitative results could be obtained. The distribution of the signal on the test line is shown Figure A1 in Appendix A. The SERRS spectra of the test line of the paper strips are shown in Figure 2.6(b). Among the three strong characteristic peaks (1173 cm^{-1},1368 cm^{-1}, and 1617 cm^{-1}), 1617 cm^{-1} was chosen as the best peak due to the nitrocellulose paper having a low background at this peak. By comparing the SERRS

intensity at 1617 cm^{-1} from the test lines, the signal was shown to increase with an increasing concentration of cTnI.

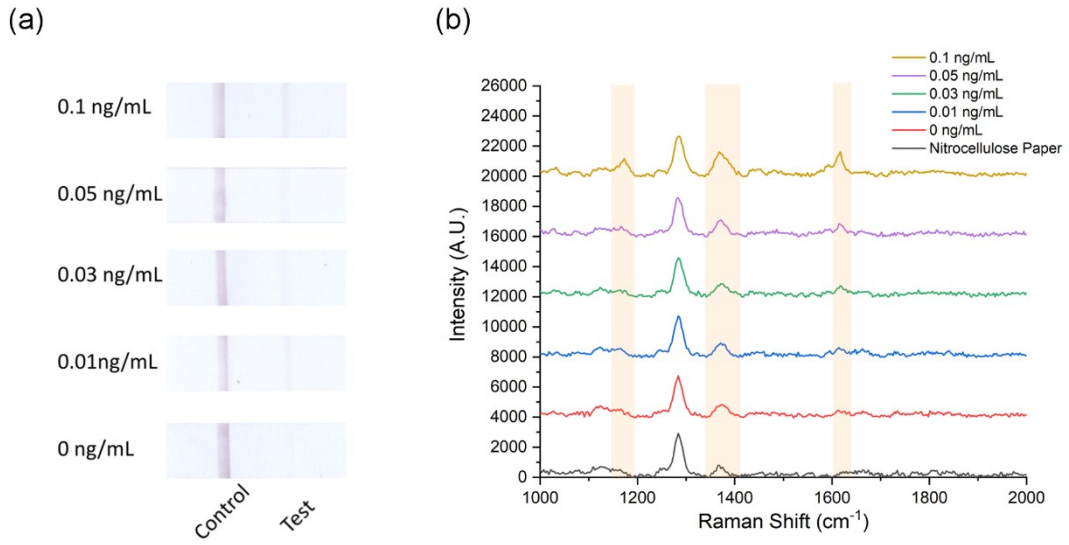

Figure 2.6 (a) Images of paper strips and (b) SERRS spectra from the test line on a blank nitrocellulose paper and the paper strips after loading different concentrations of cTnI.

The correlation of the SERRS peak intensity at 1617 cm^{-1} with the cTnI concentration (0- 0.1 ng/mL) is shown in Figure 2.7. The SERRS signal observed for 0 ng/mL of cTnI could be due to some non-specific binding of the secondary aptamer functionalized silica particle with the primary aptamer/streptavidin on nitrocellulose paper. The results show that SERRS intensity was linearly correlated with the concentration of cTnI, and the limit of detection (LOD) was calculated to be 0.016 ng/mL.

The dynamic range of the developed aptamer-based paper strip for cTnI was 0.016 - 0.1 ng/mL, which is close to the physiological relevant range of cTnI (0.01–0.1 ng/mL). This result indicates that the developed aptamer-based paper strip has a potential to be used to quantitatively detect cTnI at the point-of-care. The comparison of the developed aptamer-based paper strip with previously reported assays for detection of cTnI is shown in Table A1 in Appendix A. Compared with other paper-based assays[236, 242, 243], the developed paper strip used an aptamer, which is more thermally stable, has better tolerance to wide range of pH, and is a lower cost recognition element (>50 times lower cost compared to the cost of cTnl antibodies purchased on-line) [155, 250]. In addition, using a portable reader, it showed good sensitivity close to the lower end of physiological range and required a shorter detection time than the other assays based on aptamers [245, 246].

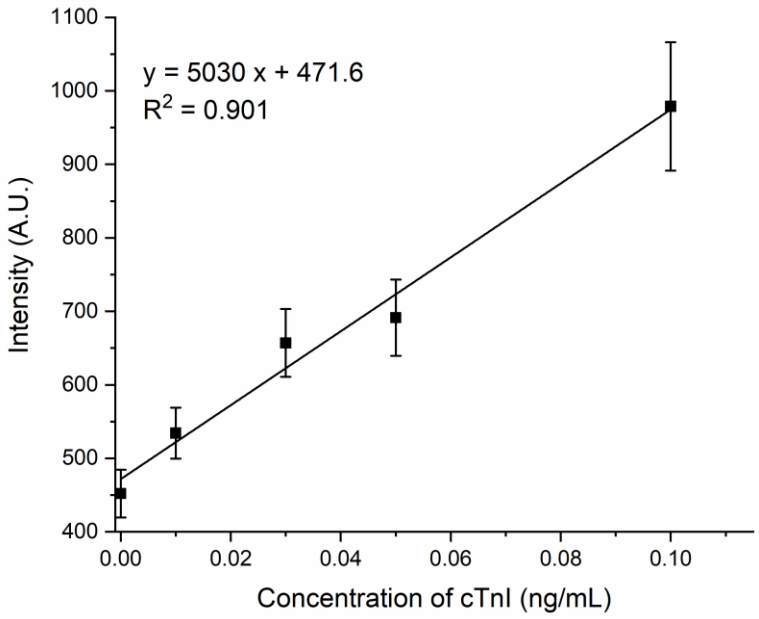

Figure 2.7 SERRS intensity at peak 1617 cm^{-1} of the test line of the aptamer-based paper strip to different concentrations of cTnI (n=3).

2.3.3. Selectivity of the assay

To evaluate the selectivity of the developed aptamer-based paper strip, potential interferents were tested all at the mid-level concentration of 0.1 ng/mL. CRP is an inflammatory biomarker and is used in risk stratification in cardiac diseases [256]. h-FABP is a protein and its concentration would increase after MI [257]. BNP is a neurohormone released from the cardiac cells and the increase in its concentration would indicate heart failure [257]. Thus, CRP, h-FABP, and BNP were used to show the specificity to these potential interferents. These interferents were tested under the same experimental conditions as cTnI. Tests for each sample were performed in triplicate. Figure 2.8 shows the SERRS intensity at peak 1617 cm^{-1} measured from test lines of these

samples. It is shown that the aptamer-based paper strip had low response to CRP and BNP. The signal intensity of h-FABP was higher than CRP and BNP, but as shown in Figure 2.8 all three signals were statistically lower than cTnI. All three components were in the same range as the background (i.e. zero concentration of cTnI), indicating these interferents had a negligible change on the spectra from non-specific binding. These results indicate the aptamer-based paper strip had a good selectivity to cTnI.

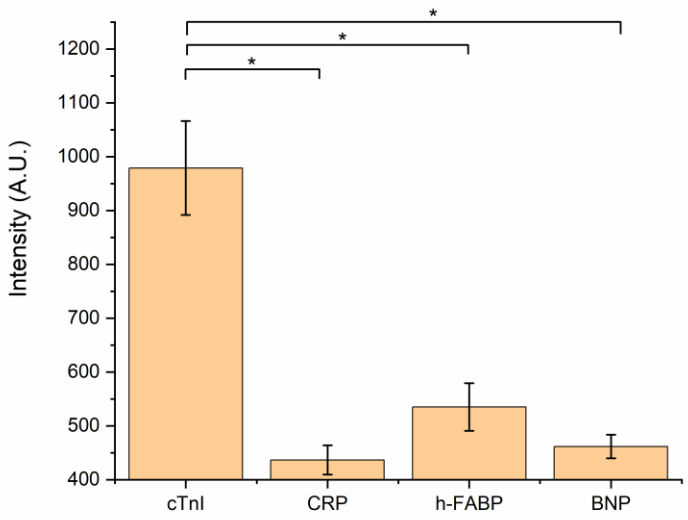

Figure 2.8 SERRS intensity at 1617 cm^{-1} of cTnI, CRP, h-FABP, and BNP, demonstrating the selectivity of the aptamer-based paper strip. *Significantly different ($p<0.05$).

2.3.4. Stability of the assay

To evaluate the stability of developed aptamer-based paper strip, the paper strip was stored in a sealed container at room temperature and its response to 0.03 ng/mL cTnI over 10 days was tested. As shown in Figure 2.9, the SERRS signal changes over 10 days were within 8% of the initial response on day 1. On Day 10, the signal retained 96.5% of the initial response on Day 1. These results indicate that the developed aptamer-based paper strip had reasonable stability when stored at room temperature over 10 days.

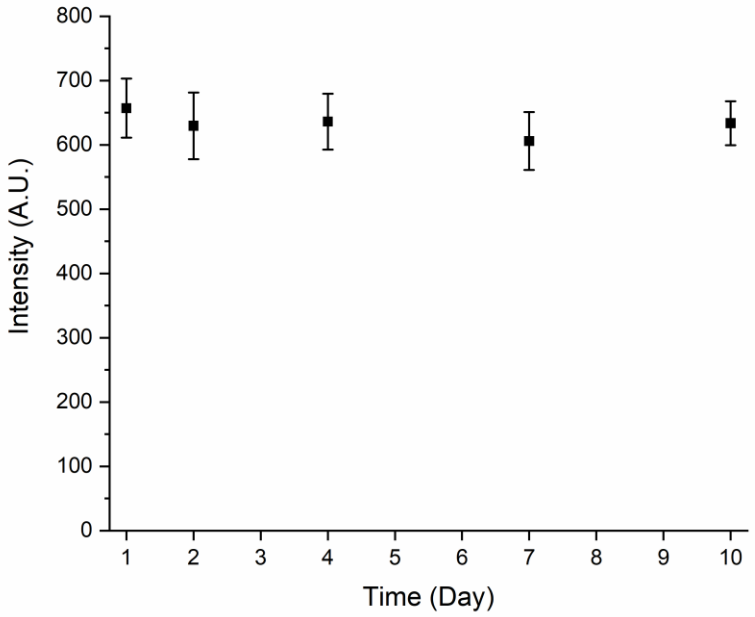

Figure 2.9 Stability of the aptamer-based paper strip stored at room temperature over 10 days.

2.3.5. Analysis of cTnI in serum

To evaluate the performance of the aptamer-based paper strip for detection of cTnI in a complex biological sample matrix, a standard addition method was used to detect the recoveries of different concentrations of cTnI in human serum. The result is shown in Table 2.1. It can be observed that the recovery rate was in the range of 93.8% - 95.8% indicating the serum matrix had a low effect on the assay. No dilution of serum sample was needed in this assay due to the use of 50 μL running buffer, which helped the serum to flow and reduced the effect of higher viscosity of the serum. Therefore, the developed aptamer-based paper strip was shown to have the potential to be applied for the clinical determination of cTnI in a more complex medium.

Table 2.1 Test for the detection of cTnI in serum samples (n=3).

Sample	Added (ng/mL)	Found (ng/mL)	Recovery (%)	RSD (n=3, %)
1	0.03	0.0285	93.83%	4.99%
2	0.05	0.0479	95.83%	3.52%

2.4. Conclusion

In this work, an aptamer-based SERRS assay on a paper strip for detection of cTnI was developed and characterized. The developed assay used aptamer rather than

antibodies as the recognition element, due to its low relative cost, good thermal stability, tolerance to a range of pH levels, and long shelf life. The assay used silica/MGITC/AuNPs to provide a strong and stable SERRS signal at a 638 nm excitation wavelength. A handheld Raman spectrometer was used to measure the SERRS signal. A lateral flow strip design was used to build the paper fluidic strip. The particles were stored in the paper strip and ensured a simple operation for end users. After introducing the sample with cTnI in the sample pad, a sandwich binding of the aptamer/silica/MGITC/AuNPs, the cTnI, and the aptamer on test line formed when cTnI was present. The SERRS signal on the test line increased with the concentration of cTnI. The developed assay for cTnI had a detection range of 0.016-0.1 ng/mL, with a LOD of 0.016 ng/mL. The developed assay also showed good selectivity to cTnI compared with other potential interferents. In addition, the developed assay showed stability over ten days and good performance in spiked serum samples. To increase the sensitivity in the low concentration range, a larger sample volume or a particle that produces a higher SERRS signal (e.g. nanostars, nanoshells, etc.) could be used in future tests. In addition, the assay time could be decreased by using a nitrocellulose paper with a faster flow rate. Overall, this work showed that the aptamer-based SERRS assay on a paper platform has the potential to provide a sensitive, selective, stable, repeatable and cost-effective platform for the detection of cTnI, toward eventual use in diagnosis of MI at the point-of-care.

3. PAPER MICROFLUIDIC DEVICE WITH A HORIZONTAL MOTION VALVE AND A LOCALIZED DELAY FOR AUTOMATIC CONTROL OF A MULTISTEP ASSAY *

3.1. Introduction

A microfluidic paper-based analytical device (μPAD) is a platform comprised of hydrophilic and hydrophobic channel networks in paper [176, 177]. Paper has the merits of abundance, low-cost, ease of disposability, ease of manipulation, being environmentally friendly, and having compatibility with biological samples [247]. Due to these advantages, paper-based devices have demonstrated their capability for being used in implementing assays, especially in point-of-care testing (POCT) [167, 174, 258-260]. However, most of these paper-based devices perform assays without controlling the fluid[167-175]. Fluidic control in a μPAD is important in implementing high-performance assays. For instance, controlling the fluid to flow at a slower flow rate in paper-based devices can improve the sensitivity of the assay [186, 188, 191]. A fluidic control valve can also be used to implement multi-step assays, such as those that include sequential loading, incubation, and washing [205, 206, 213, 214, 261]. Thus, μPADs capable of implementing a multi-step protocol would help to translate high-performance assays into point-of-care settings.

Efforts to control flow rate have included several designs such as changing the geometries of the channel [179-184] or altering the permeability of the paper by using

* Reprinted with permission from Dandan Tu, Allison Holderby, John Dean, Samuel Mabbott, Gerard L. Coté, "Paper Microfluidic Device with a Horizontal Motion Valve and a Localized Delay for Automatic Control of a Multistep Assay," *Anal. Chem.* 2021, 93, 10, 4497−4505. https://dx.doi.org/10.1021/acs.analchem.0c04706.

materials including wax [185-187], agarose [188], sucrose[189, 190], and trehalose[191]. Sucrose is a popular permeability altering material since it is a water-dissolvable, abundant and low-cost material. It is also currently used in the preservation of reagents in many paper-based analytical devices and has minimal effect on many assay chemistries [190]. A wide range of time delays have been achieved by using a sucrose-based dissolvable delay [190]. However, the dissolvable delay using sucrose typically covers the whole channel and the method used makes it difficult to quantify the sucrose applied on the channel. This type of dissolvable delay is not suitable for the localization of sucrose in a specific position in the channel. In one study, a sucrose-based dissolvable barrier was fabricated by depositing a sucrose solution on paper using a modified craft-cutting instrument [189]. Using this method, the position and volume of the localized sugar delay are well controlled. However, 5 drawings on a Whatman grade 1 chromatography paper only provided a delay time of around 48 s, which is enough for this application but may be too short for POC applications that often require more time [189]. Therefore, a simple one-step method to precisely make a localized dissolvable sugar delay, which efficiently increases the flow time and decreases the flow rate would be desirable.

To achieve multi-step processes using μPADs, various methods have been developed [181, 182, 190, 191, 193, 205, 206, 213-216, 218]. Automatic systems are easier to use especially for untrained users [205, 206]. To retain the cost-effectiveness of μPADs, eliminating the dependence on auxiliary instruments for automatic multi-step processes is desired. With no auxiliary instruments, multi-step processes can be achieved by controlling the fluid flow in different channels such that the fluid arrives at the reaction

point at different times. Perturbation of fluid flow speeds in μPADs may occur using the following techniques: channel geometry variations [181, 182], dissolvable materials [190, 191, 213-215], variation in paper wettability [213, 214, 216], and carving channels on paper [193]. Limitations in these methods include loss of effective fluid volume, which can affect the assay reaction and fluid mixing with the dissolvable materials leading to a change in assay chemistries. Designs using folded paper actuators [218] and compressed cellulose sponges [206] have the potential to overcome these limitations as each method utilizes valve actuation for multi-step processes. In the two designs, the connection or separation of channels for fluid of different steps are controlled by vertical movements generated by a sponge or a folded paper actuator. However, the channels that are designed to stay spatially separated at different heights have the potential to become falsely connected before actuation. To ensure its performance, extra care is needed to prevent false actuations between channels. Developing a μPAD that uses horizontal movement of the actuator could largely avoid this problem.

In this paper, a simple and robust system that includes a mechanical valve using horizontal movement to implement a multi-step process in a μPAD along with a localized dissolvable delay to control flow rate and enhance assay sensitivity is described. This study was the first demonstration of using a mixture of fructose and sucrose in a dissolvable delay. The effect of the ratio of fructose to sucrose, the volume of the mixture, and the position of the dissolvable delay were analyzed. A one-step method using pipetting and wax-printed scale lines was used to make the dissolvable delay in a localized region. In addition, a horizontal motion mechanical valve, a paper arm and a compressed sponge

was used to achieve a multi-step process. The paper arm uniquely transformed the vertical movement of the compressed sponge into a horizontal movement. The developed μPAD, that included the localized dissolvable delay and the mechanical valve, was initially characterized with dye solutions and then tested on a model assay namely; a surface-enhanced Raman scattering (SERS) assay developed to target cardiac troponin I (cTnI), a clinically validated biomarker for myocardial infarction.

3.2. Materials and methods

3.2.1. Materials

Whatman Grade 1 chromatography paper was purchased from GE Healthcare (IL, USA). Glass fiber pad (GFCP000800) was from EMD Millipore (MA, USA). Thick blot filter paper (#1703932) was purchased from Bio-Rad (CA, USA). The compressed rectangular sponge (43CC) was purchased from Sponge Producers Company (MO, USA). The mounting adhesive sheets were purchased from Michaels (TX, USA). Transparent sealing film (UC-500) was from Axygen (CA, USA). Food dye (red) were purchased from a local supermarket (TX, USA). Sucrose, D-(-)-fructose, sodium citrate tribasic dihydrate, gold(III) chloride trihydrate, (3-mercaptopropyl)trimethoxysilane (MPTMS), 2-propanol, tetraethyl orthosilicate (TEOS), ammonium hydroxide (28%), ethanol, sodium cyanoborohydride ($NaBH_3CN$), and sodium periodate ($NaIO_4$) were purchased from Sigma Aldrich (MO, USA). Malachite green isothiocyanate (MGITC) and green fluorescent particles (G0100) were purchased from Thermo Fisher Scientific (MA, USA). Carboxy-poly(ethylene glycol)-thiol (SH-PEG-COOH, Mw 10 kDa) was purchased from

Nanocs (NY, USA). N-hydroxysulfosuccinimide sodium salt (Sulfo-NHS) and N-ethyl-N'-(3-dimethylaminopropyl)carbodiimide hydrochloride (EDC-HCl) were from CovaChem (IL, USA). (3-triethoxysilyl)propylsuccinic anhydride (TEPSA) was purchased from Gelest (PA, USA). Cardiac Troponin I (cTnI) was purchased from GenScript (NJ, USA). The sequence of aptamers for cTnI assay was reported previously [156, 157]. In this work, aptamer 1 (5'-amine-2 hexa-ethyleneglycol spacers-CGTGC AGTAC GCCAA CCTTT CTCAT GCGCT GCCCC TCTTA -3') and aptamer 2 (5'-amine-2 hexa-ethyleneglycol spacers-CGCAT GCCAA ACGTT GCCTC ATAGT TCCCT CCCCG TGTCC-3') were used. Both aptamers and the control line DNA strand (5'-amine–hexa-ethyleneglycol spacer-GGACA CGGGG AGGGA ACTAT GAGGC AACGT TTGGC ATGCG- 3') were from Integrated DNA Technologies (IA, USA). Milli-Q ultrapure water (18.2 MΩ cm^{-1}) was used in all the procedures.

3.2.2. Instrumentation

The wax was printed on the paper using a ColorQube 8570 wax printer (Xerox, USA). The fluid flow on the paper was recorded using a webcam (Logitech Webcam c922). The fluorescent images and videos were recorded using a benchtop Nikon Eclipse Ti2-U fluorescence microscope (Nikon, Japan). Scanning electron microscope (SEM) images were acquired on a JEOL JSM-7500F (JEOL, Japan). Transmission electron microscopy (TEM) images were acquired on a JEOL JEM-2010 (JEOL, Japan). All SERS spectra were collected using a Thermo Scientific DXR Raman confocal microscope with a 780 nm laser. The magnification and numerical aperture of the objective were 10× and

0.25, respectively. The spectral range was from 200 cm^{-1} to 1800 cm^{-1}, and the spectral resolution was 3.0-4.1 cm^{-1}. Samples were excited with a 24 mW laser using 2-sec exposure per reading. All spectra were baseline corrected.

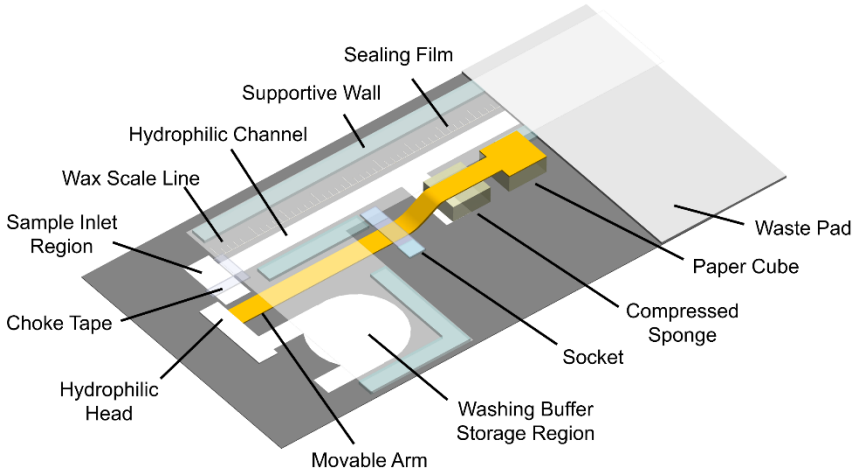

Figure 3.1 Schematic representation of a µPAD with a horizontal motion mechanical valve.

3.2.3. Preparation of paper substrates

Hydrophobic wax barriers and wax scale lines were patterned on Whatman grade 1 chromatography paper. The paper with wax patterns was then heated in an oven at 120 °C for 2 min to melt the wax and form the hydrophobic boundary. An adhesive backing sheet was taped on the bottom of the paper. Two pieces of hydrophobic tape, labeled as "choke tape" in Figure 3.1, were used to form a sample inlet region at the beginning of the

hydrophilic channel. The choke tape was used to direct fluid samples into the porous paper matrix and to prevent them from flowing onto the surface of the paper.

3.2.4. Horizontal motion mechanical valve

Figure 3.1 shows the design of the lateral motion mechanical valve in the μPAD. A compressed sponge (6mm × 6 mm × 2.5 mm) was fixed to the paper using adhesive tapes. The overlapping region between the sponge and the hydrophilic channel was 6 mm × 3 mm. The movable arm is composed of a hydrophobic wax body and a hydrophilic head. A socket to guide the horizontal movement of the arm was made using paper and adhesive tape. The arm went through the socket, and the end the hydrophobic body was taped on a paper cube with a height of 2.5 mm. The paper cube, which was taped on the wax region, was used to keep the end of the arm high and reduce the downward pressure applied on the compressed sponge. A transparent sealing film was covered on top of the hydrophilic region with a 0.5 mm gap between the sealing film and the paper. Adhesive sheets with a thickness of 0.5 mm were used as a supportive wall to form the gap. The fabricated paper was then stored in a sealed container before use. The detailed information of the dimensions and positions of components of the horizontal motion mechanical valve is shown in Figure B1 in Appendix B.

Performance of the mechanical valve was characterized using red and blue food colorings, diluted in PBS. 150 μL of the blue solution was loaded in the washing solution storage area, followed by loading 75 μL of the red fluid into the inlet of the μPADs. Movement of the two fluids was recorded using a webcam. Height change of the compressed sponge was measured using a digital caliper.

3.2.5. Localized dissolvable delay

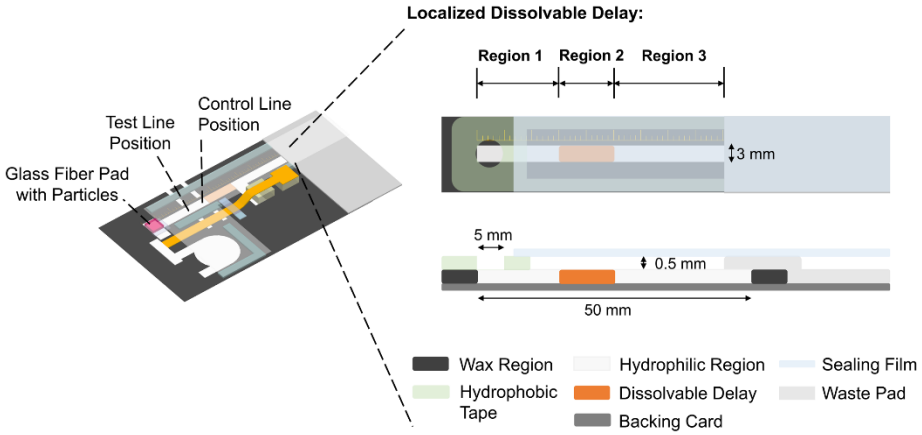

Figure 3.2 Schematic representation of the µPAD with a mechanical valve and a localized dissolvable delay for a multi-step assay. Components and dimensions of the localized dissolvable delay portion of the µPAD are shown in the blow-up detail on the right.

Figure 3.2 shows the overall design of the µPAD with mechanical valve and the localized dissolvable delay for a multi-step assay. The dissolvable delay portion was initially fabricated and tested before adding the mechanical valve. To make the dissolvable delay region, the following process was used. Sucrose was mixed with water at room temperature for 2 days to yield a saturated sucrose solution (concentration of ~2 g/mL at 20 °C) [190]. Concentrations of 0.2 g/mL, 0.6 g/mL, 1 g/mL, 1.4 g/mL, and 1.8 g/mL of sucrose solutions were made by adding different volumes of water into the saturated sucrose solution. To make sucrose/fructose mixtures, 0.5 g, 1 g, 1.5 g, and 2 g fructose

was added into 1 mL of the sucrose solutions to get sucrose solutions with 0.5 g/mL, 1.0 g/mL, 1.5 g/mL, and 2.0 g/mL fructose, respectively. Full details of the sucrose solution and sucrose/fructose mixture compositions are shown in Table B1 in Appendix B. Solutions were agitated for 2 hours to aid dissolution.

The mixture was deposited on the hydrophilic channel of the paper using reverse pipetting, meanwhile, the wax scale lines were used to indicate the position of the drop. The paper containing the sucrose/fructose mixture solution was left at room temperature with 55% humidity until the solution is fully dispersed across the paper. The paper was then dried in an oven at 45 °C for 12 hours. After drying the mixture, a dissolvable delay was formed in a small localized area. The hydrophilic region was then covered with a sealing film using adhesive sheets (thickness of 0.5 mm) as a supportive wall. The μPAD was then stored in a sealed container with desiccant before use.

The dissolvable delay was characterized using a webcam to record movement of the fluid front in the hydrophilic channel after loading 50 μL of PBS containing red dye. Characterization of the particle count of 1.1 μm green fluorescent particles in the hydrophilic channel with and without a localized dissolvable delay was measured using a fluorescent microscope. Specifically, movement of the fluorescent particles at 10 mm down the channel in the μPADs was recorded at 300 s, 600 s, 900 s, 1200 s, 1440 s, and 1680 s, after loading the fluorescent particles in 50 μL of water. The particle count was obtained using a Lagrangian particle tracking algorithm [262, 263]. One-way analysis of variance (ANOVA) in OriginLab was used to determine whether the flow times were

significantly different when using different dissolvable delays. A theoretical analysis and discussion regarding the dissolvable delay are given in Appendix B.

3.2.6. Aptamer based SERS assay using μPAD

As shown in Figure 3.2, a test line and a control line were formed on the μPAD for the multi-step assay. To develop the test line and the control line, aptamer 1 and the control line DNA strand were immobilized on the hydrophilic channel of cellulose paper using a modified process based on the Schiff base plus reduction method [264]. The detailed process is described in Appendix B. After immobilization of aptamer 1 on the μPAD, the localized dissolvable delay and the mechanical valve was fabricated using the processes mentioned in the previous section.

SERS-active silica shell particles functionalized with MGITC as the Raman reporter molecule were synthesized. Aptamer 2 was then attached to the synthesized silica shell particle using TEPSA as a linker. The synthesized aptamer functionalized SERS active particles were then dried on the glass fiber pad and cut into 4 mm × 4 mm squares. The glass fiber pad with the particles was put at the inlet of the μPAD, as shown in Figure 3.2. The detailed process to synthesize the silica shell particles and dry them on the glass fiber pads is described in Appendix B.

To test the performance of the developed μPAD, we developed a model assay for the detection of cTnI solutions. Specifically different concentrations of cTnI (0, 0.01, 0.05, 0.1, 0.2, 0.5, 1 ng/mL) were prepared in PBS (PH 7.4). The assay was implemented by loading 150 μL of wash-ing buffer (PBS with 0.25% Tween 20) in the washing solution

storage area and loading 75 μL of the cTnI solution in the sample inlet. After loading the solutions, the μPAD automatically com-pleted the steps of wicking the sample to the reaction region and washing excess reagents. After the washing solution was completely wicked, the SERS signal of the test line in the μPAD was measured using a Raman microscope.

3.3. Results and discussion

3.3.1. Measuring the delay time with the localized dissolvable delay

The dissolvable delay portion of the μPAD (Figure 3.2) was first tested before introducing the mechanical valve. The delay was positioned in the middle (Region 2) of a 50 mm hydrophilic channel. Region 1 and Region 3 represent the areas before and after the localized delay, respectively. Evaporation, which could cause loss of sample solution and change in flow rate, cannot be neglected in a long-time reaction. Thus, a sealing film was used to cover the hydrophilic region in the μPAD. The evaporation test, depicted in Figure B3 in Appendix B, shows a significant reduction in the percent of mass loss with time when the sealing film was used indicating reduced evaporation.

Fructose, a monosaccharide, that combines with glucose to form sucrose, has been used to slow down crystallization of sucrose because fructose attaches on the major growing face of a sugar crystal and inhibits the incorporation of the sucrose [265]. Here, fructose and mixtures of fructose and sucrose were evaluated for their performance in providing a localized dissolvable delay. We tested our flow delay by measuring the time the fluid front took to reach the location in Region 3 (40 mm). Based on results contained

within Appendix B including Figure B4, 0.6 g/mL sucrose and 1.0 g/mL fructose were selected and combined to form the optimal sucrose/fructose mixture that provided a long delay time. Further, the flow time of the solution through the μPAD with a localized delay composed of the fructose/sucrose mixture was compared with a blank μPAD and one with localized delays made of just 0.6 g/mL sucrose. As shown in Figure 3.3(a), the localized sucrose/fructose delay provided a flow time of 661 s, close to 2 times the flow time in a μPAD without a dissolvable delay (348 s), and was better than only sucrose. The longer flow time of the sucrose/fructose mixture may be attributed to the higher-viscosity mixture dispersing slower across the paper, with the slower speed in forming sucrose crystals, and/or could be the better penetration in the paper pores of fructose. Due to these effects, less pores present after drying (Figure B5(c) in Appendix B). More effectively filled pores possibly decreased the cylindrical pore radius, which increased flow time and reduced flow rate. Moreover, as the sugar was effectively dissolved, both fructose and sucrose increased fluid viscosity and the fluid was effectively slowed down due to the higher viscosity.

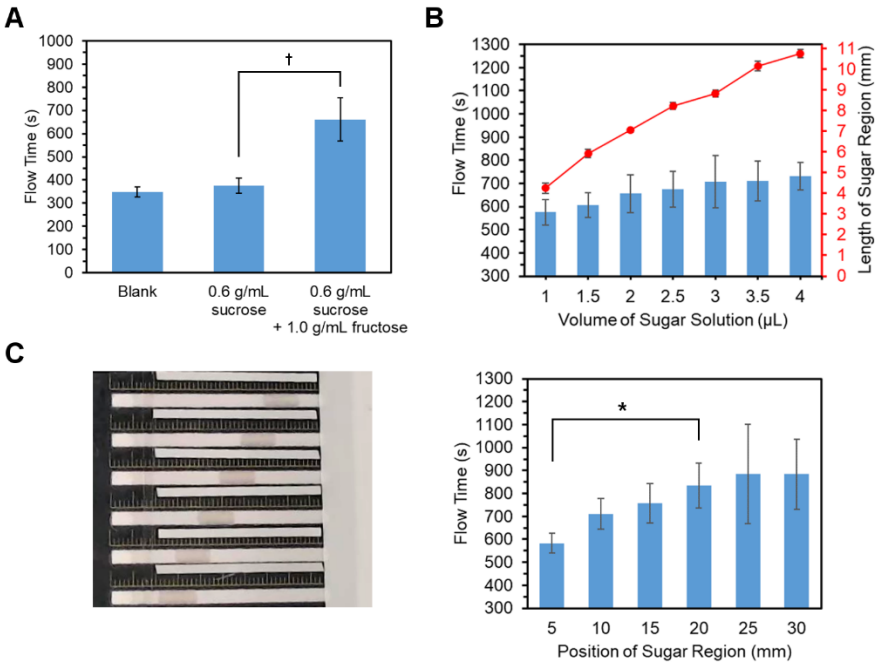

Figure 3.3 (a) Comparison of the flow time of the fluid front to reach 40 mm on a µPAD without a dissolvable delay, a µPAD with a localized dissolvable delay made of 3 µL of 0.6 g/mL sucrose, and a µPAD with a localized dissolvable delay made of 3 µL of 0.6 g/mL sucrose with 1.0 g/mL fructose. All the localized dissolvable delays were located at the 10 mm position. †Significantly different ($p<0.05$). (b) The column data is the flow time on the µPADs with localized dissolvable delays made of different volumes of 0.6 g/mL sucrose with 1.0 g/mL fructose, and the scatter data is the length of the sugar region. All the localized dissolvable delays were located at the 10 mm position. (c) Left: Image of the µPADs with localized dissolvable delays made with 2.5 µL of 0.6 g/mL sucrose and 1.0 g/mL fructose at different positions (light grey area shifted from left to right as you go from bottom to top). Right: Flow time for the fluid front to reach 40 mm on the hydrophilic channel of the µPADs. *Significantly different compared with delays located at different positions ($p<0.05$).

3.3.2. The effect of dissolvable delay region width and distance from the inlet

In our work, the dissolvable delay is in a localized region in the µPAD and this limited length of the sugar region enables a flexible position for the assay design in µPADs. The lengths of the sugar region were affected by the volume of the

sucrose/fructose mixture dried on the channel. Figure 3.3(b) shows that the larger the volume of sugar solution, the longer the length of the sugar region. Dissolvable delays with lengths ranging from 4.3 mm to 10.8 mm were achieved. Figure 3.3(b) also shows that the longer length of the sugar region, the longer the flow time, but the flow time was effectively constant after the length of the sugar region reached 8.2 mm (i.e. 2.5 μL of sugar solution).

The increase in flow time with the increased volume of sugar solution could be attributed to a longer Region 2 with a small cylindrical pore size, and a higher fluid viscosity in both Region 2 and Region 3. Based on Figure 3.3(b), because the increase of flow time slowed down at 2.5 μL, 2.5 μL of 0.6 g/mL sucrose with 1.0 g/mL fructose was selected for the following experiments due to its short length and long delay time.

The effect of the position of the sugar region was characterized, and Figure 3.3(c) shows the μPAD with sucrose/fructose delays made at different positions down the channel and their different flow times. As discussed in the theoretical analysis in Appendix B, for a longer Region 1, the start of Region 2 that contains the sugar mixture is further away, which causes a slower dissolution. This slower dissolution allows the pore sizes to stay small and the paper to exhibit low porosity (i.e., the sugar mixture does not dissolve as quickly and so there is a smaller cylindrical pore radius) but also yields a lower viscosity (i.e. there is less material dissolved in the solution and traveling to Region 3). Notably, these two factors affect the flow time in opposite directions according to Equation 1 in Appendix B. From the result shown in Figure 3.3(c), the flow time was longer the farther the sugar region was from the inlet (5 mm to 20 mm). This suggests that the effect of the

location on the sugar mixture region on keeping the cylindrical pore radius small was larger than the lower fluid viscosity. In addition, the figure showed that the flow time reached a plateau when the dissolvable sugar mixture region was further than 20 mm. At 15 mm an effective delay in flow was depicted with a flow time of 756 s, which was 2 times greater in the μPAD without a dissolvable delay. As a result, the 15 mm position was selected as the position for the localized dissolvable delay.

To use the μPAD for an assay, a test line with recognition elements was immobilized to capture target analytes and particles and a control line was created to capture excess particles and ensure the assay was working correctly. The test line and control line were designed to be located in Region 1 (before the delay) instead of Region 3 (after the delay) in order for the assay to avoid interaction with the dissolved sugar. Given the dissolved sugar mixture region starts at 15 mm from the inlet, the control line was located at 14mm and the test line at 10 mm from the inlet. The flow at the 10 mm test line position was characterized using fluorescent particles (see details in Appendix B). As shown in Figure B6 in Appendix B, the localized delay decreased the particle flow at the 10 mm test line position. This result validated that the localized dissolvable delay effectively decreased flow rate and extended time for the assay to react.

3.3.3. Mechanical valve using a two-step design

A novel mechanical valve using horizontal movement was developed using a paper arm and a compressed sponge. The two-step process is shown in Figure 3.4(a). For Step 1, a red solution was loaded at the inlet and flowed down the hydrophilic channel. When the solution reached the compressed sponge, the sponge increased in height after it absorbed the sample solution. A paper arm and socket were used to transfer the vertical movement of the compressed sponge into a horizontal movement. When the paper arm moved, the hydrophilic head connected the washing buffer storage region with the hydrophilic channel, which then initiated Step 2, and the blue solution started to flow in the hydrophilic channel.

Figure 3.4(b) shows the height change of the compressed sponge (actuator) related to the volume of the red solution loaded in the sample inlet. The larger the volume of the red solution, the larger the height change and, correspondingly, the larger the horizontal movement. Figure 3.4(b) shows the height increased from 0.8 mm to 6.2 mm as the solution volume increased from 25 μL to 225 μL. However, the increase was much slower after the volume reached 125 μL and effectively stopped after the volume reached 175 μL. The reduced slope after 125 μL was primarily because the compressed sponge enlarged, became softer, and leaned to one side. Similarly, the horizontal movement of the hydrophilic head, depicted in Figure 3.4(c), showed a slowdown in the change after 125 μL. The slight leaning of the enlarged sponge also resulted in the moveable arm shifting to an angle, which contributed to the larger standard deviation in the horizontal movement. Thus, before initiating Step 2, the total volume of solution in Step 1 was kept smaller than

125 µL. Within this range, the horizontal movement allowed for a variation from 0.4 mm to 3.4 mm.

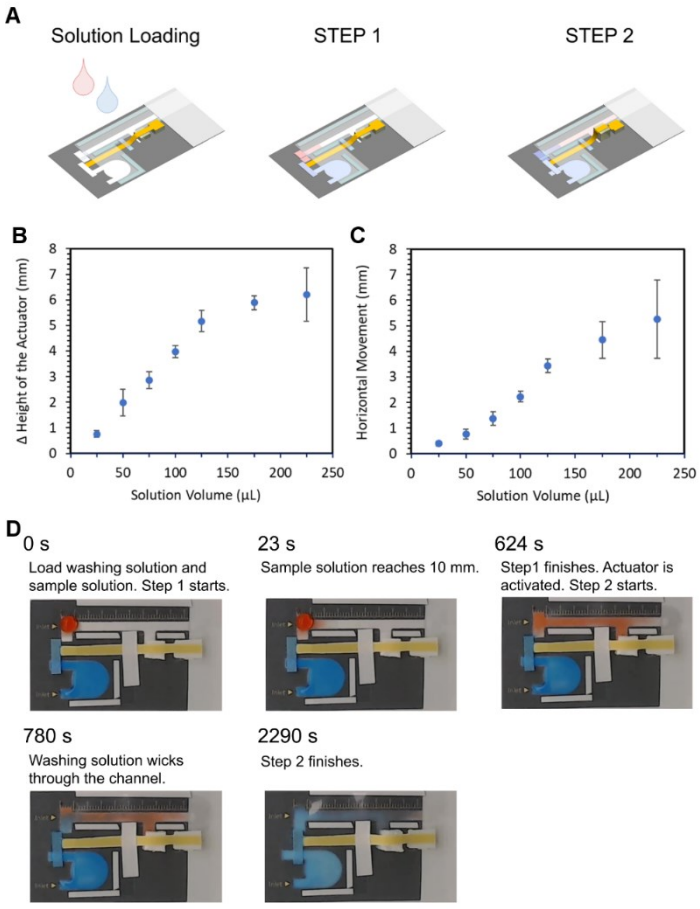

Figure 3.4 (a) Schematic representation of using the µPADs with a mechanical valve to finish a two-step process automatically. (b) Height change of the actuator (c) Horizontal movement of the arm in a µPAD with a mechanical valve when adding different volumes of the red solution. (d) Time-lapsed images of loading solutions at the beginning and finishing the two steps automatically on a µPAD with the mechanical valve.

The time-lapsed images of the flow on the μPAD with the mechanical valve are shown in Figure 3.4(d). At 0 s, the washing buffer storage region was loaded with 150 μL blue solution. The hydrophilic head was also wetted because wetting the hydrophilic head kept it in good contact with the paper surface and ensured a successful connection of the hydrophilic channel and the washing buffer storage region after actuation of the mechanical valve. 75 μL red solution was also loaded and began to travel down the channel reaching the mechanical valve sponge actuator after 624 s. The mechanical valve then automatically initiated Step 2, and the blue solution began loading and finished flowing at roughly 2290 s. Figure B7 in Appendix B shows the repeatability of the flow time in the μPAD with the mechanical valve. It can be observed that the design provided a consistent control in the time to open the valve and initiate Step 2.

3.3.4. Mechanical valve using a four-step design

In addition to the two-step process, the mechanical valve was modified to achieve a four-step process as characterized in Figure 3.5. The modified μPAD was tested using PBS with four different colored solutions. Initially, 50 μL of the green, red, and blue solutions were loaded in the solution storage areas and then 50 μL of the yellow solution was loaded in the inlet of the μPAD. After loading the four solutions, the μPAD automatically finished the four-step process. As depicted in Figure 3.5, the yellow solution starts to flow in the channel after 0 s and is absorbed by the sponge. The valve is actuated and the green solution starts to flow at roughly 316 s, is absorbed by the sponge, causing the valve to open further and the red solution starts to flow at roughly 641 s. The red

solution is absorbed by the sponge, opening the valve further allowing the blue solution to flow at roughly 1095 s. Compared to previous literature designs using a compressed sponge[206], this design uses horizontal movement instead of vertical movement to achieve the multi-step procedure. In this way, false actuations between the channels, that are designed to stay spatially separated at different heights before actuation, can be avoided.

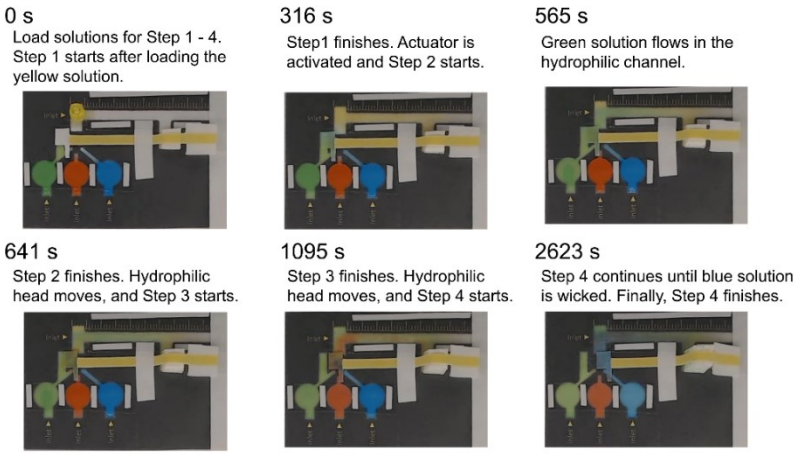

Figure 3.5 Time-lapsed images of the addition of solutions at the beginning and end of an automated four-step µPAD with a horizontal mechanical valve.

3.3.5. Aptamer based SERS assay design and results using the µPAD

A high sensitivity cTnl assay at the POC and outside the central lab, for example in an ambulance, is important to help the diagnosis and early treatment of MI [229]. Toward that goal, a two-step aptamer-based SERS assay for cTnI was developed using the

μPAD with a localized dissolvable delay and a mechanical valve. Figure B10 in Appendix B shows the schematic plot of the assay. In the assay, aptamers were used as the recognition element and SERS-active silica shell particles were used to transduce the signal (Figure B9 in Appendix B shows the TEM image of the silica shell SERS active particle). Aptamer 1 was immobilized on the hydrophilic channel of the μPAD. Figure B8 in Appendix B shows a strong fluorescent intensity observed on the test line region confirming the successful immobilization of aptamer 1 on the paper. Aptamer 2 functionalized SERS active particles were stored in the glass fiber inlet pad. To initiate the automatic two-step assay, the washing buffer and sample solution were loaded in the washing buffer storage region and sample inlet, respectively. After loading, the sample resuspended the aptamer 2 functionalized particles and they started to flow in the channel. When cTnI was present in a sample, it bound with aptamer 2 functionalized particles, which were then captured by aptamer 1 on the test line. The unbound aptamer 2 functionalized particles with no cTnI were captured on the control line. When the solution reached the delay region, the dissolvable delay slowed down the flow. After the sample solution dissolved the sugar, the fluid passed through and actuated the mechanical valve. The washing buffer was released and automatically flowed in the channel and washed off excess chemicals and unbound particles. The SERS signal of the test line was measured to determine the concentration of cTnI in the sample.

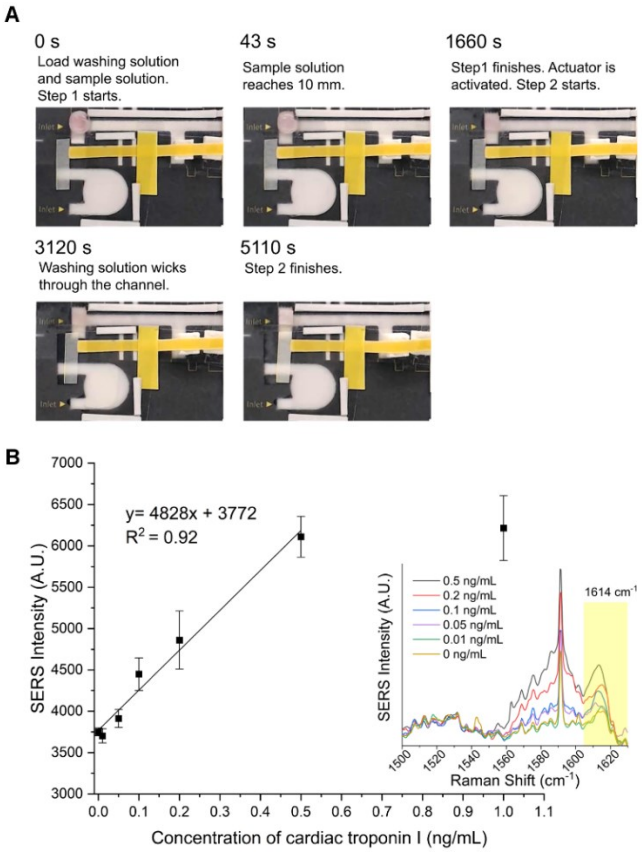

Figure 3.6 (a) Time-lapse images of fluid flow in a µPAD with a localized dissolvable delay and a mechani-cal valve. (b) SERS response of the µPAD to different concentrations of cTnI in a PBS solution. The inset is the SERS spectra for 0 ng/mL to 0.5ng/mL of cTnI. The peak intensity at around 1614 cm^{-1} (C-C and N-phenyl ring stretches in MGITC) is used. The SERS intensity value in the response curve represents the summed value of the peak intensities in a 2.9 mm × 0.9 mm area on the test line. Each concentration was tested using three replicates.

Figure 3.6(a) shows the time-lapse images of fluid flow in the µPAD. The contrast is lower here because nanoparticles with Raman reporters and a washing buffer were used instead of food dye solution. The SERS response to different concentrations of cTnI was acquired after the washing buffer finished flowing, and the results were shown in Figure

3.6(b). Details about the SERS signal measurement and data processing are described in Appendix B. Figure 3.6(b) shows the SERS intensity on the test line was linearly correlated with the concentration of the cTnI from 0 ng/mL to 0.5 ng/mL. The limit of detection (LOD) was 0.02 ng/mL. The focus for using this model assay was to show that the two-step SERS assay on the μPAD, with a localized dissolvable delay and a mechanical valve, could quantitatively determine the concentration of cTnI in a PBS buffer. Moreover, the assay response and the flow time in μPADs with and without the delay were compared in Figure B13 and Figure B14 in Appendix B. It was shown that, compared with the μPAD without the delay, the flow time in the μPAD with the dissolvable delay in step 1 was longer and the assay was more sensitive in the low concentration range, validating the slowing effect from the delay, which was designed to allow for more time for the assay components to react.

3.4. Conclusion

In this paper, a novel μPAD with a localized dissolvable delay and a horizontal motion mechanical valve was developed. A simple one-step method was used to fabricate the localized dissolvable delay region. A mixture of fructose and sucrose was shown to form an effective delay gate. Ratios of fructose to sucrose, volumes of the mixture, and positions of the delay were optimized. The localized dissolvable delay made of 2.5 μL of 0.6 g/mL sucrose with 1.0 g/mL fructose at 15 mm was determined to provide an effective increase of flow time to allow the assay to interact. A two-step and four-step process were successfully implemented using the horizontal mechanical valve with a paper arm and a

compressed sponge. Because the paper arm in the mechanical valve moved in a horizontal direction, it prevented problems often encountered in vertical direction valves and provided robust activation. The developed μPAD was successfully used to automate an aptamer-based SERS assay for the quantitative detection of cTnI. In the assay, the localized dissolvable delay increased reaction time to ensure good detection sensitivity and the mechanical valve automatically actuated the washing step. The assay performance can be further improved if particles with stronger SERS signal were used and the μPAD production was automated. The developed μPAD was shown to provide a useful way to implement high-performance multi-step assays automatically and has the potential to play a role in converting current multi-step laboratory assays into simple point-of-care devices that have high performance yet remain easy to use.

4. SPECTRALLY MULTIPLEXED ASSAY USING GAP ENHANCED NANOPARTICLE FOR DETECTION OF A MYOCARDIAL INFARCTION BIOMARKER PANEL

4.1. Introduction

Myocardial infarction (MI) is a cardiac disease which manifests as myocardial necrosis due to extended ischemia in cardiomyocytes.[1, 6] Detection of cardiac biomarkers in blood is indispensable in the diagnosis of MI.[8] Cardiac troponin I (cTnI) has been demonstrated to have high specificity for MI diagnosis, and is a well-established biomarker according to American Heart Association and American College of Cardiology guidelines.[26] The clinically relevant cut-off values of cTnI are within the 0.01-0.1 ng mL^{-1} range.[39] Compared with detecting of cTnI alone, using a multiple biomarker panel has shown better performance in clinical studies.[47-49, 58, 59] Copeptin is a biomarker that can indicate the onset of MI,[45] with a clinical cut-off value of 0.056 ng mL^{-1}.[43] Several clinical studies demonstrate the additive value of copeptin on troponin for early rule-out of MI.[47-49] Heart-type fatty acid-binding protein (h-FABP) is another biomarker elevated in concentration after onset of MI.[53] The clinical relevant cut-off values of h-FABP are within the range of 5-16.8 ng mL^{-1}.[56, 57] Adding h-FABP on troponin can help to improve sensitivity in diagnosis of MI and help in early diagnosis of MI.[58, 60, 62, 63] Thus, detection of the biomarker panel composed of cTnI, copeptin, and h-FABP, will help improve MI diagnostic performance.

Development of a point-of-care (POC) testing for detection of the cardiac biomarkers could make the onsite diagnosis of MI more feasible, especially in limited resource settings. In addition, POC testing is capable of achieving short result turnaround times compared to samples measured in a central laboratory [68]. A multiplexed assay is more efficient to detect a biomarker panel than a single-biomarker assay, because the multiplexed assay usually needs less total volume of sample, shorter analysis time, and lower total cost.[69] In a recent study, a signal amplified chemiluminescence assay incorporating Co(II) catalyst/antibody/luminol functionalized gold nanoparticles was used for the simultaneous detection of the three biomarkers.[85] In another study, a signal amplified duplex assay for cTnI and h-FABP was developed using metal ion functionalized titanium phosphate nanospheres as electrochemical labels.[266] However, these assays require complicated assay steps, including several washing steps, several incubation steps, and manual operations to add labels and overlap layers during assay. The complicated procedure is not user-friendly at the POC and requires specialized user training. Lateral flow assay strip is widely used at the POC due to test simplicity, rapidity, low cost, and user-friendliness.[69, 162-164] A common way to achieve multiplexed detection on a lateral flow assay strip, is through spatial separation of test zones using different lines [73-76] or dots [77, 78]. However, multiplexed detection in a single test zone could enable shorter manufacturing time, reduced reagent consumption, decreased manufacturing cost, shorter assay time, and reduced signal evaluation time.[69, 72] Labels with different colors,[80] Raman peaks,[72, 77, 82] fluorescent peaks,[79] time windows

for signal reading,[79, 81] or electrochemical redox peaks,[82] can be used to differentiate the signals from different analytes in a single test zone.

Recently, gap-enhanced nanoparticles (GeNPs), also called gap-enhanced Raman tags [107] or bilayered Raman-intense gold nanostructures with hidden tags (BRIGHTs) [113], have been developed to provide strong and stable surface-enhanced Raman scattering (SERS) signal. The morphologically advanced particles have demonstrated high performance in imaging and biosensing [107, 113, 123]. GeNP is composed of a metal core, a metal shell, an interior nanogap between the core and the shell, and the Raman reporter molecules (RRM) embedded in the nanogap. GeNP has advantages of encapsulation of RRM inside a protective shell which prevents signal fluctuation due to desorption of RRM,[97] avoiding the competitive adsorption between RRM and recognition elements of a sensor when both are functionalized on the surface of the nanostructure, as well as the high enhancement factor attributed to the inner nanogap between core and shell.[267] Because gold has a good chemical stability [87] and good biocompatibility [100], a GeNP with a gold core and gold shell is preferred. Studies have detailed the formulation of GeNPs with a gold core and gold shell using different spacers to form the gap.[105, 109-112, 128] When the amount of spacers reaches an effective coverage on the core surface, a gap layer is formed between the core and grown shell.[108] When using oligonucleotides,[109] polymers,[105, 110, 111] cyclodextrin,[128] and silica dioxide,[112] as the spacer, the spacer takes a large portion of the surface area on the metallic core, which leads to a smaller area for RRM. Some studies have reported to use RRMs, usually small organic molecules with a thiol group, as the spacer.[107, 108, 129-

131] Because the RRM itself is capable of forming a gap,[108] the whole surface of the metallic core is available for the RRM attachment. Compared with RRMs with one thiol group, RRMs with dithiol groups are capable of forming strong attachments to both core and shell, leading to very stable GeNP capable of generating significant SERS signals. However, limited dithiol RRMs are available and most exhibit very similar vibrational peaks, which limiting their capacity for multiplexed analysis.[130] Thus, it is important to develop a new method to synthesize a set of GeNPs, which use RRMs as the spacer, forms strong Au-S bond on both core and shell side, and use RRMs with distinguishable peaks.

Here we have developed a multiplex assay using a single test line for the simultaneous detection of three biomarkers: cTnI, copeptin, and h-FABP. Due to the low circulating concentrations of the three biomarkers in human body, we have opted to generate a novel set of GeNPs for high SERS signal and discriminative vibrational peaks. Different RRMs were used in the GeNPs, including 4-mercaptophenylacetic acid (MPAA), 5,5′-dithiobis(2-nitrobenzoic acid) (DTNB), and 2,3,5,6-tetrafluoro-4-mercaptobenzoic acid (TFMBA). Additionally, 6-amino-1-hexanethiol (6-AHT) was used together with these monothiol RRMs to enable formation of Au-S bond on both core and shell side in the GeNPs. From the best of our knowledge, it is the first time to use this strategy for formation of a set of GeNPs. Assays for the detection of the three biomarkers were developed using the GeNPs. Paper-based lateral flow assay strip was used as the platform to ensure the simplicity, cost-effectiveness, and user-friendliness of the assay. The assay was tested in buffer solutions and serum samples, and the cross interference among the three biomarkers was also evaluated.

4.2. Experimental section

4.2.1. Materials and chemicals

Human cardiac troponin I was purchased from Abcam (Cambridge, UK). Human heart fatty acid binding protein was purchased from Hytest (Turku, Finland). Human copeptin was purchased from Phoenix Pharmaceuticals (CA, USA). Monoclonal mouse anti-cardiac troponin I (19C7cc and 560cc) and monoclonal mouse anti-human fatty acid binding protein (10E1 and 28) were purchased from Hytest (Turku, Finland). Monoclonal anti-human copeptin (4801 and 4804) were purchased from Medix Biochemica (Espoo, Finland). Monoclonal anti-mouse IgG (M8642) were purchased from Sigma (MO, USA). Troponin I free serum was purchased from Hytest (Turku, Finland). Human cardiac troponin I ELISA kit (ab200016) was purchased from Abcam (Cambridge, UK). ELISA kit for copeptin (CPP) was purchased from Cloud-Clone Corp. (TX, USA). Human heart fatty acid-binding protein ELISA kit was purchased from Sigma (MO, USA). Whatman grade 1 chromatography paper and Whatman FF120HP nitrocellulose paper were purchased from Cytiva (MA, USA). Glass fiber (GFCP000800) was purchased from EMD Millipore (MA, USA). Thick blot filter paper was purchased from Bio-Rad (CA, USA). *N*-ethyl-*N*'-(3-dimethylaminopropyl) carbodiimide hydrochloride (EDC-HCl) and N-hydroxysulfosuccinimide sodium salt (sulfo-NHS) were purchased from CovaChem (IL, USA). Thiol-poly(ethylene glycol)-acid (SH-PEG-COOH, 2 kDa) was purchased from Nanocs (NY, USA). Bovine serum albumin (BSA), 6-amino-1-hexanethiol hydrochloride (6-AHT), L-ascorbic acid, sodium citrate tribasic dihydrate, gold (III) chloride trihydrate

($HAuCl_4 \cdot 3H_2O$), cetyltrimethylammonium chloride solution (CTAC), 4-mercaptophenylacetic acid (MPAA), and 5,5′-dithiobis(2-nitrobenzoic acid) (DTNB) were purchased from Sigma Aldrich (MO, USA). 2,3,5,6-tetrafluoro-4-mercaptobenzoic acid (TFMBA) was purchased from Tokyo Chemical Industry (Tokyo, Japan). Milli-Q ultrapure water (18.2 MΩ cm^{-1}) was used in all the procedures.

4.2.2. Instrumentation

The test line and control line were dispensed on the lateral flow paper strip using a dispenser (ClaremontBio Solutions, USA). Extinction spectra of particles were measured on a Tecan Infinite 200 Pro (Tecan, Switzerland) microplate reader. Transmission electron microscopy (TEM) images were acquired on a JEOL JEM-2010 (JEOL, Japan). The zeta potential and hydrodynamic size of the particle were measured on a Zetasizer Nano ZS90 (Malvern, UK). The concentration of particles was measured on a Nanosight Nanoparticle Tracking Analysis (NTA) system (Malvern, UK). The SERS spectra were collected using a Thermo Scientific DXR Raman confocal microscope with a 780 nm laser and were baseline corrected prior to analysis. The magnification of the objective was 10× and the numerical aperture of the objective was 0.25. The spectral range was from 200 cm^{-1} to 1800 cm^{-1}, and the spectral resolution was 3.0-4.1 cm^{-1}. EM field distributions of Au_{core} and GeNP were calculated using Ansys Lumerical.[268]

4.2.3. Synthesis of gold-core gold-shell gap-enhanced nanoparticle

The gold core nanoparticle (Au_{core}) was synthesized using a seed-mediated synthesis method.[252] The detailed process to synthesize Au_{core} is in the supporting information. The gold-core gold-shell (Au_{core}/RRM/Au_{shell}) GeNP was synthesized using RRM as the spacer and 6-AHT as the linker to form the nanogap. Figure 4.1 shows the process used to synthesize the Au_{core}/TFMBA/Au_{shell} GeNP. The method was also used in the Au_{core}/DTNB/Au_{shell} and the Au_{core}/MPAA/Au_{shell} GeNPs. The general procedure is as-follows: 50 µL of TFMBA dissolved in ethanol (10 mM) was added to 1 mL of the Au_{core} solution (around 240 pM). The mixture was allowed to react on a shaker (400 rpm speed) at room temperature for overnight. The obtained Au_{core} /TFMBA particle was centrifuged (1500 rcf, 15 min) and resuspended in 1 mL of phosphate buffer (PH 7.4). Similarly, 50 µL of DTNB (10 mM) was added to 1 mL of the Au_{core} solution, which was allowed to incubate overnight. The formed Au_{core}/DTNB particle was centrifuged and resuspended in 100 µL DMSO and 900 µL of phosphate buffer. To form Au_{core}/MPAA particle, 50 µL of MPAA (10 mM) was added to 1 mL of the Au_{core} solution, which was incubated for 30 min, centrifuged, and resuspended in 100 µL DMSO and 900 µL of phosphate buffer.

Next, 2 µL of EDC-HCl (16 mM) and 1 µL of 6-AHT (10 mM) were added to the Au_{core}/MPAA. Similarly, 2 µL of EDC-HCl (16 mM) and 100 µL of 6-AHT (0.01 mM) were added to the Au_{core}/DTNB and the Au_{core}/TFMBA. The particle solutions were sonicated for 30 min, centrifuged, and resuspended in 1 mL of CTAC solution (0.1 M). Each obtained particle solution was then added into a mixture composed of 6 mL of 0.1 M

CTAC solution, 270 µL of $HAuCl_4$ (4.65 mM), and 111.2 µL of ascorbic acid (40 mM). After 30 min of sonication, the solution was centrifuged (1000 rcf, 15 min) and washed with 0.1 M CTAC solution. Finally, the synthesized gold-core gold-shell GeNP was resuspended in 1 mL of water and stored in a fridge before using.

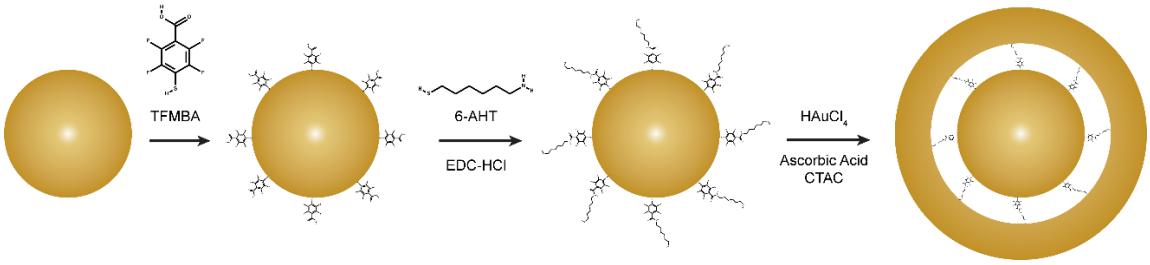

Figure 4.1 Process to synthesize the Au_{core}/TFMBA/Au_{shell} GeNP.

4.2.4. Preparation of antibody conjugated gap-enhanced nanoparticle

The antibody was covalently immobilized on the GeNP using SH-PEG-COOH as a linker. The following process is used to prepare the antibody conjugated GeNP for the detection of h-FABP (GeNP/$Ab_{h\text{-}FABP}$). To start with, 300 µL of 1mM SH-PEG-COOH in phosphate buffer was mixed with 600 µL of Au_{core} /MPAA/Au_{shell} GeNP (around 462 pM). The mixture was shaken overnight before being centrifuged (1000 rcf, 12 min) and resuspended in 600 µL of phosphate buffer. Next, EDC-HCl (0.2 mg) and sulfo-NHS (0.6 mg) were added into the resuspended solution, which was then left to mix for 30 min. The nanoparticles were centrifuged and resuspended in 600 µL of phosphate buffer, followed

by addition of 3.8 μL of anti-human fatty acid binding protein antibody (10E1) solution (6.6 mg mL^{-1}). The mixture was shaken for 1 hour, followed by the addition of 150 μL of BSA (5%, w/v) in phosphate-buffered saline (PBS, PH 7.4). After shaking for 30 min, the particles were centrifuged and washed with BSA (1%, w/v) in PBS (PH 8.5). Finally, the synthesized GeNP/$Ab_{h\text{-}FABP}$ was resuspended in 600 μL of PBS (PH 8.5) containing BSA (0.1%, w/v) and stored in a fridge before using. The same procedures were repeated for the different antibodies using the GeNPs containing TFMBA and DTNB. Specifically, Au_{core} /TFMBA/Au_{shell} GeNP and 4.8 μL of anti-human copeptin antibody (4801) solution (5.2 mg mL^{-1}) were used to get antibody conjugated GeNP for the detection of copeptin (GeNP/$Ab_{Copeptin}$). In addition, Au_{core} /DTNB/Au_{shell} GeNP and 3.3 μL of anti-cardiac troponin I antibody (560cc) solution (7.5 mg mL^{-1}) were used to get antibody conjugated GeNP for the detection of cTnI (GeNP/Ab_{cTnI}).

4.2.5. Preparation of lateral flow assay strip

To begin with, a Whatman FF120HP nitrocellulose paper (25 mm in width) was dispensed with antibodies to form the test line and the control line. To prepare the control line, anti-mouse IgG solution (0.25 mg mL^{-1}) was dispensed on the nitrocellulose paper using a 6 V power supply and a pump with a flow rate of 0.2 mL min^{-1}. To prepare the test line, a solution mixed of anti-cardiac troponin I antibody (19c7cc) solution (0.05 mg mL^{-1}), anti-human fatty acid binding protein antibody (28) solution (0.25 mg mL^{-1}), and anti-human copeptin antibody (4804) solution (0.05 mg mL^{-1}) were dispensed on the nitrocellulose paper. The nitrocellulose paper was dried at 4 ℃ overnight. The

nitrocellulose paper was then immersed in a phosphate buffer (PH 7.4) with BSA (1%, w/v), triton X-100 (0.1%, v/v), and trehalose (4%, w/v) for 5 min and dried at 37 °C for 30 min. The sample pad was prepared by soaking a Whatman grade 1 chromatography paper (15 mm width) in PBS (PH 7.4) with BSA (0.1%, w/v) and drying it at 37 °C for 1 hour. The conjugation pad was prepared by soaking a glass fiber pad (8 mm width) in a borate buffer (PH 9) with BSA (1%, w/v) and trehalose (4%, w/v). After drying the glass fiber pad at 37 °C for 1 hour, a mixture (1:1:1) of GeNP/$Ab_{h\text{-}FABP}$, GeNP/$Ab_{Copeptin}$, and GeNP/Ab_{cTnI}, was dropped on the glass fiber and was dried at 37 °C for 1 hour. The absorption pad is a thick blot filter paper (25 mm width), which is connected to the nitrocellulose paper via a grade 1 Whatman paper (4 mm width). The sample pad, conjugation pad, antibody functionalized nitrocellulose paper, and absorption pad were assembled on an adhesive card with 2 mm overlap between the pads. Finally, the assembled paper was cut into paper strips with a width of 5 mm and stored in fridge.

4.2.6. Assay test for single biomarker detection

To evaluate the single biomarker detection performance in a buffer solution, the following samples were prepared. Samples with different concentrations of cTnI (0 - 0.1 ng mL^{-1}), h-FABP (0 - 50 ng mL^{-1}), or copeptin (0 - 0.07 ng mL^{-1}) in PBS (PH7.4) were prepared for testing each assay. To test the performance of the assay for single biomarker detection in a serum matrix, human serum solutions spiked with different concentrations of cTnI, h-FAHP, or copeptin were prepared. The background concentration of cTnI, h-FABP, and copeptin in the serum solution was firstly measured using commercial ELISA

kits. The measured cTnI concentration in the serum was below the detection limit of the ELISA kit (0.0044 ng mL^{-1}), thus we used it as a cTnI free serum sample. The measured background concentration of h-FABP in the serum was 2.3 ng mL^{-1}. The measured background concentration of copeptin in the serum was 0.007 ng mL^{-1}. Based on these measured background concentrations, serum samples with 0 - 0.3 ng mL^{-1} of cTnI, 2.3 - 52.3 ng mL^{-1} of h-FABP, or 0.007 - 0.077 ng mL^{-1} of copeptin were prepared. The prepared biomarker spiked serum samples were used without any dilution.

The following procedures were used to run the assay. To begin with, 50 µL of sample was dropped on the sample pad. After the sample was wicked into the conjugation pad, 50 µL of running buffer (PBS with 0.25% tween (v/v)) was added. It takes about 25 min for the sample and the running buffer to completely wick through the strip. Tests for each concentration were performed in triplicate. Then, the SERS signal on the test line was read. The SERS intensity on the test line area was measured using the mapping function in the Thermo Scientific DXR Raman confocal microscope with a 780 nm laser. A 3 × 12 point array was measured on the test line area. The step size of the array in the direction parallel to the test line was 400 µm, and the step size of the array across the test line was 200 µm. Each point was measured by excited with a 20 mW laser using 2 s exposure. All spectra were baseline corrected.

4.2.7. Assay test for multiplex detection of the biomarker panel

The performance of the assay for multiplex detection of the biomarker panel was evaluated in a human serum matrix. Human serum solutions spiked with mixture of

different concentrations of cTnI, copeptin, and h-FABP were prepared. Specifically, mixture 1 (0 ng mL^{-1} cTnI, 2.3 ng mL^{-1} h-FABP, 0.007 ng mL^{-1} copeptin), mixture 2 (0.07 ng mL^{-1} cTnI, 12.3 ng mL^{-1} h-FABP, 0.037 ng mL^{-1} copeptin), and mixture 3 (0.1 ng mL^{-1} cTnI, 27.3 ng mL^{-1} h-FABP, 0.057 ng mL^{-1} copeptin) were prepared. The serum mixture samples were used without any dilution. The same assay procedures as used in the single biomarker tests were used.

4.3. Results and discussion

4.3.1. Principle of the assay

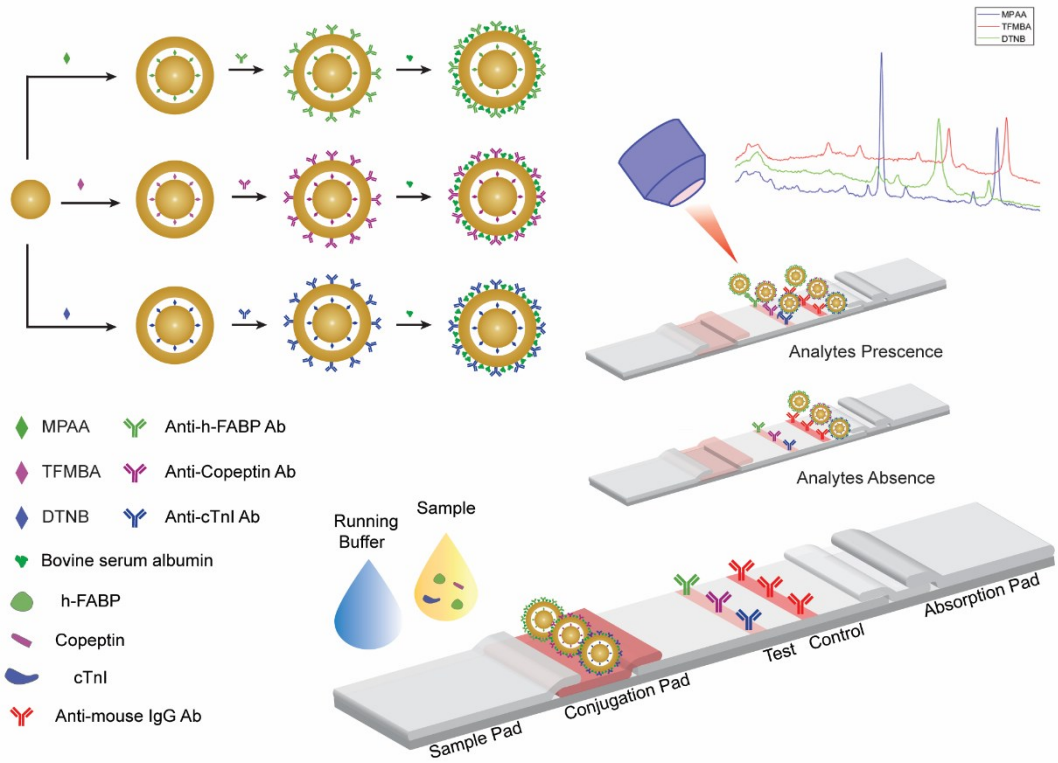

Figure 4.2 Schematic illustration of the process to prepare antibody conjugated gap-enhanced nanoparticle, and the lateral flow strip for a multiplex detection of the biomarker panel for myocardial infarction.

As shown in Figure 4.2, the designed assay was based on a lateral flow assay strip. Antibodies were used as the recognition elements of the target biomarkers and GeNPs were used to provide the SERS signal. Three GeNPs with MPAA, TFMBA, and DTNB, respectively, were used to produce SERS spectra with different characteristic peaks. The three GeNPs were then conjugated with secondary antibodies specific to h-FABP, copeptin, and cTnI, respectively. Bovine serum albumin (BSA) was used to block the particles, reducing nonspecific binding. In the lateral flow assay strip, primary antibodies specific to h-FABP, copeptin, and cTnI were immobilized on a single test line. The antibody conjugated GeNPs (GeNP/Ab) that have the secondary antibodies specific to h-FABP, copeptin, and cTnI, were dry-stored on the conjugation pad.

The assay is initiated by adding the sample to the sample pad. The sample solution moves to the conjugation pad, where the solution resuspended the dried GeNP/Ab. When the h-FABP, copeptin, and cTnI biomarkers are present in the sample, they bind to their respective secondary antibodies on the GeNP. Primary antibodies are specific to each of the biomarkers. Biomarker capture leads to the formation of a sandwich assay when the primary antibody, captured biomarker, and the GeNP are all present. At higher target biomarker concentrations more GeNP/Ab is captured on the test line. Excess GeNP/Ab flow across the control line, where the anti-mouse IgG antibody bound with the GeNP/Ab. When there was no target biomarker present in the sample, particles were only captured on the control line. Finally, the excess running buffer and particles were wicked by the absorption pad. The SERS spectra on the single test line was used to quantify the

concentration of h-FABP, copeptin, and cTnI in the sample. The signal from the single test line was resolved by the differentiable SERS peaks related to each of the three biomarkers. Specifically, the presence of h-FABP in the sample was related to the characteristic peaks of MPAA in the SERS spectra. The presence of copeptin was related to the peaks of TFMBA. The presence of cTnI was related to the peaks of DTNB.

4.3.2. Characterization of the gap-enhanced nanoparticle

The gold-core gold-shell GeNPs were synthesized using RRM as the spacer. This strategy makes the whole surface of the gold core available for RRM adsorption which enables good SERS signal. Three RRMS, MPAA, DTNB, and TFMBA were used in synthesizing three gold-core gold-shell GeNPs (Au_{core}/MPAA/Au_{shell} GeNP, Au_{core}/DTNB/Au_{shell} GeNP, Au_{core}/TFMBA/Au_{shell} GeNP). The peak assignments and the SERS spectra of the three GeNPs are shown in Table C1 and Figure C1 in Appendix C. All of the three RRMs have a thiol group and a carboxylic group. The amine terminated alkane thiol linker, 6-AHT is covalently bound to the carboxylic acid group of the RRMs via EDC coupling. After the 6-AHT was bound, the gold core surface was surrounded by a layer of thiol groups. Reduction of $HAuCl_4$ using ascorbic acid in the presence of the gold core particles, facilitates the formation of a gold shell. The thiol groups from the RRM and the introduced 6-AHT helped to form strong Au-S bonds on both core and shell side, which increase the stability of the GeNPs and results in the generation of a robust SERS signal. In addition, the formation of molecule-metal bonds on both core and shell made the chemical enhancement available and might contribute partly to enhance the

SERS signal. Figure 4.2 illustrates the mentioned synthesis steps using Au_{core}/TFMBA/Au_{shell} GeNP as an example.

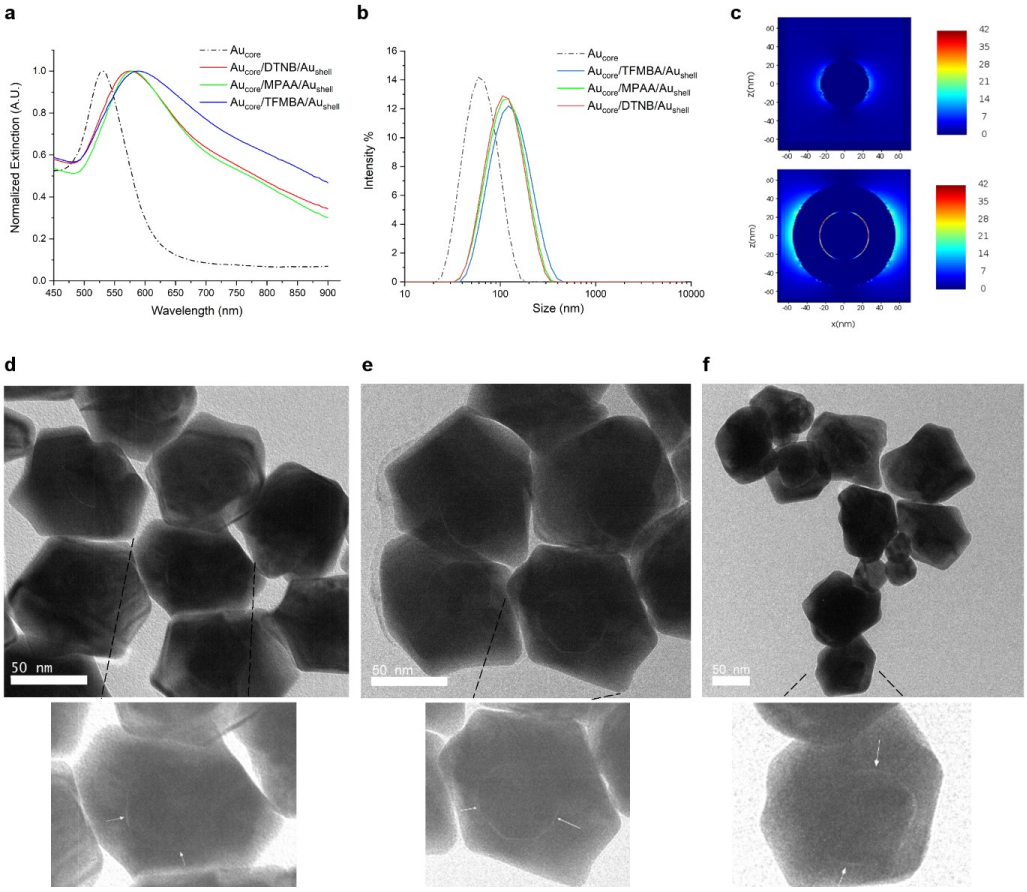

Figure 4.3 (a) Extinction spectra and (b) hydrodynamic size distributions of the synthesized Au_{core} nanoparticle, Au_{core}/DTNB/Au_{shell} GeNP, Au_{core}/MPAA/Au_{shell} GeNP, and Au_{core}/TFMBA/Au_{shell} GeNP. (c) FDTD simulation of electromagnetic field of Au_{core} and GeNP. In the simulation, Au_{core} size is 52.1 nm, gap size is 0.9 nm, shell thickness is 28.3 nm, and incident light wavelength is 780 nm. The TEM images of the synthesized (d) Au_{core}/DTNB/Au_{shell} GeNP, (e) Au_{core}/MPAA/Au_{shell} GeNP, and (f) Au_{core}/TFMBA/Au_{shell} GeNP. Inset: TEM images after increasing brightness, the gap is also labeled with white arrows.

A complete gold shell plays a large role in generating strong and uniform SERS signal.[109] The amount of 6-AHT bound to the RRMs determines the amount of thiol group available. Sufficient 6-AHT is required for effective coverage and complete formation of a gold shell. Additional 6-AHT may also fill in the spare surface area between RRMs on the gold core, as a result a reduction of electrostatic repulsion between particles could lead to particle aggregation. Thus, we optimized the amount of 6-AHT added to enable efficient gold shell growth. The full optimization process is detailed in the supporting information and displayed in Figure C2 in Appendix C. The optimal amounts of 6-AHT were then used to synthesize each GeNP: 0.01 mM was used in the synthesis of Au_{core}/MPAA/Au_{shell} and 0.001 mM was used in Au_{core}/TFMBA/Au_{shell} and Au_{core}/DTNB/Au_{shell}. Figure 4.3(a) shows the extinction spectra of the synthesized particles. Compared with the Au_{core}, the GeNPs had a red shift in the localized surface plasmon resonance (LSPR) peak due to the growth of gold shell. The red shift of Au_{core}/TFMBA/Au_{shell} was larger than the other two, indicating a thicker shell was grown in this particle.

The hydrodynamic sizes of the synthesized particles were characterized using dynamic light scattering. As shown in Figure 4.3(b), the hydrodynamic sizes of the three GeNPs were larger than the Au_{core} (52.1 nm) indicating a successful growth of outer shell. Specifically, the hydrodynamic size of the Au_{core}/TFMBA/Au_{shell} was 110.6 nm, indicating a growth of 29.3 nm in radius. The hydrodynamic size of the Au_{core}/DTNB/Au_{shell} was 94.6 nm, indicating a growth of 21.3 nm in radius. The hydrodynamic size of the Au_{core}/MPAA/Au_{shell} was 99.6 nm, indicating a growth of 23.8 nm in radius. The size

distributions of Au_{core}/DTNB/Au_{shell} and Au_{core}/MPAA/Au_{shell} were very similar. These two GeNPs were slightly smaller in size and more monodispersed than Au_{core}/TFMBA/Au_{shell}. The larger average size and the higher polydisperse of Au_{core}/TFMBA/Au_{shell} may be caused by the lower electrostatic force and poorer particle stability of Au_{core}/TFMBA, which makes it easier to aggregate before growing the shell. The zeta potential of the synthesized particles is shown in Figure C3 in Appendix C. It shows that the surface charge of the particle changed from a strong negative value caused by citrate association to a strong positive value after growing the shell which is caused by cetyltrimethylammonium chloride (CTAC).

Figure 4.3(c) shows the electromagnetic (EM) field distribution of Au_{core} and GeNP calculated using the finite-difference time-domain (FDTD) simulation. The maximum EM field intensity at 780 nm in the gap of GeNP is 12.4 times larger than that of Au_{core}. Figure 4.3(d)-4.3(f) show the TEM images of the synthesized GeNPs. Small gaps between the metal core and the metal shell can be observed. As shown in the images, the gap sizes were around 0.9 nm, 0.9 nm, and 1.1 nm in Au_{core}/TFMBA/Au_{shell}, Au_{core}/DTNB/Au_{shell}, and Au_{core}/MPAA/Au_{shell} GeNPs, respectively. These gaps with around 1 nm size are good for generating a strong electromagnetic field for a strong SERS signal.[109]

To quantify the enhancement in SERS signal generated after growing the gold shell, we measured SERS spectra of the GeNPs and the Au_{core}/RRMs and compared their peak intensity. Notably, some studies used large-size spherical gold nanoparticles and adsorb RRM on particle surface to achieve high SERS signal.[100, 269] Because of this,

it is also of great interest to evaluate whether the GeNP is more efficient in enhancing the SERS signal than a large-size solid spherical particle. To test this, we also measured the SERS spectra of an around 99 nm solid spherical particle (Au_{99nm}), which has a similar size to the GeNPs. Figure C4 in Appendix C shows the TEM images of the synthesized Au_{core} and Au_{99nm}. The SERS comparisons are in the supporting information including Figure C5 in Appendix C. In brief, the SERS intensity of the RRM in the gap of GeNPs are more than 105 times higher than that on the Au_{core}, confirming the large enhancement effect in SERS signal after growing the shell.[108] In addition, the SERS intensity of the RRM in the gap of GeNPs are more than 15 times higher than that on the Au_{99nm}, confirming that using the gap inside the GeNP is more efficient in enhancing the SERS signal than using a large-size solid spherical particle.

Figure 4.4(a) shows the SERS spectra of the synthesized three GeNPs and molecular structures of the RRMs. The 1591 cm^{-1} peak of MPAA exhibited minimal overlap with the peaks from the other two RRMs, thus this peak of MPAA was selected for peak resolving. DTNB and TFMBA have multiple peaks displayed minimal overlap with the peaks from the other RRMs. The peak selection of DTNB and TFMBA is described in the supporting information. In brief, 1556 cm^{-1} peak of DTNB and 1632 cm^{-1} peak of TFMBA were chosen for resolving the signal from the three GeNPs. Figure 4.4(b)-4.4(d) shows the SERS signal calibration curves of the three GeNPs using the selected peaks. The limits of detection of these GeNPs were calculated according to values given by three times the standard deviation of the blank solution: 0.27 pM for the GeNP with MPAA, 0.11 pM for the GeNP with DTNB, 0.28 pM for the GeNP with TFMBA.

The good signal-to-noise ratio of these GeNPs is capable to provide SERS signal for high-sensitivity assays.

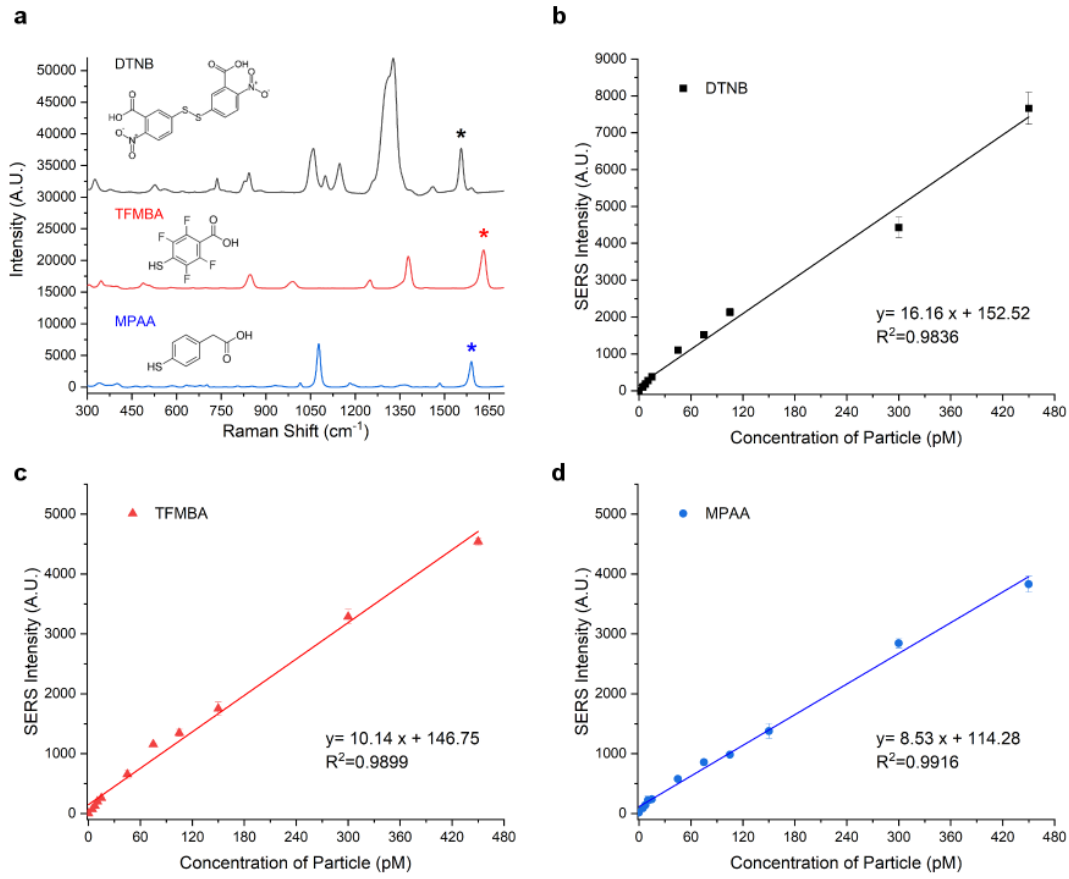

Figure 4.4 (a) SERS spectra of the synthesized GeNPs. The best distinctive characteristic peak of each GeNP is marked. Insets: molecule structures of the corresponding Raman reporter molecules. (b-d) Plots of SERS peak intensity against different concentrations of GeNPs for Au_{core}/DTNB/Au_{shell} GeNP (1556 cm^{-1}), Au_{core}/TFMBA/Au_{shell} GeNP (1632 cm^{-1}), and Au_{core}/MPAA/Au_{shell} GeNP (1591 cm^{-1}) in water, respectively. The SERS signal was obtained using 780 nm laser, 24mW power, 2 s exposure time, and 3 exposures. Error bars are mean ± SD (n = 3).

4.3.3. Analytical performance of the assay for single biomarker detection

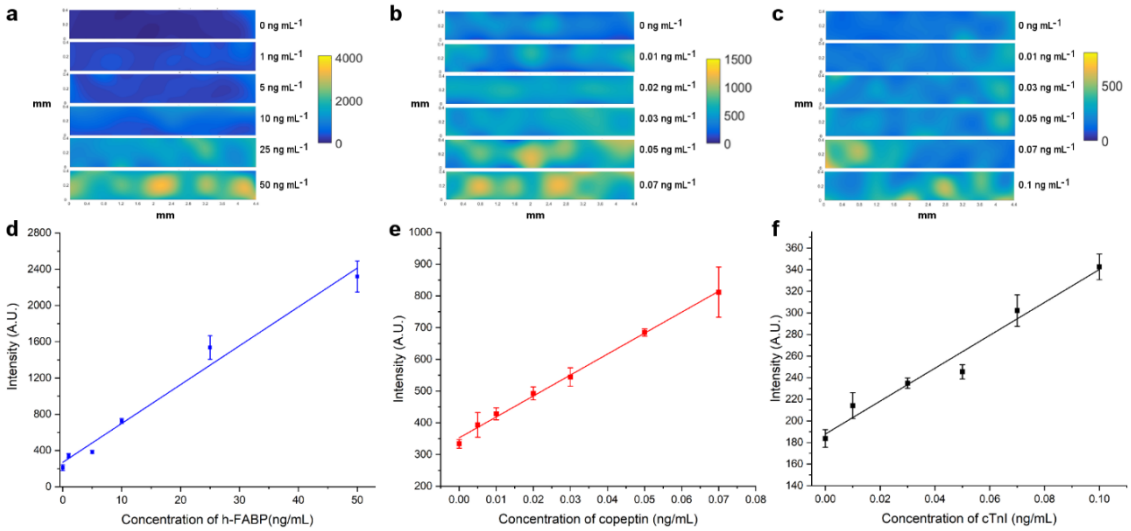

Figure 4.5 SERS intensity maps of the test line in assays for (a) h-FABP, (b) copeptin, and (c) cTnI, respectively. SERS spectra at different points covering the test line (3 × 12 points) were used to generate the plot. The SERS peak intensity at each grid point was extracted. 1591 cm^{-1} peak was used for h-FABP assay, 1556 cm^{-1} peak was used for cTnI assay, and 1632 cm^{-1} peak was used for copeptin assay. The SERS intensity was then represented using different colors. Response curves for (d) h-FABP, (e) copeptin, and (f) cTnI, respectively, in buffer solution. The SERS intensity of one paper strip was the average of SERS intensities from all the points in a map. Error bars are mean ± SD (n = 3).

The performance of the GeNPs-based lateral flow assay for the detection of each biomarker spiked in PBS buffer solution was initially evaluated. Figure 4.5(a)-4.5(c) show that the overall SERS intensity on the test line increased when the biomarker concentration was increased. Figure 4.5(d)-4.5(f) show the response curves of the assay for the detection of each biomarker. The h-FABP could be detected across 0.86-50 ng mL^{-1} of h-FABP,

with a limit of detection of 0.86 ng mL^{-1}. The copeptin could be detected across 0.004-0.07 ng mL^{-1}, with a limit of detection of 0.004 ng mL^{-1}. The cTnI could be detected across 0.01-0.1 ng mL^{-1}, with a limit of detection of 0.01 ng mL^{-1}.

Human serum, was used to evaluate assay performance in a more complex clinical biological matrix. Serum samples were spiked with different concentrations of the target biomarkers. Figure 4.6 shows the response curves for the detection of each biomarker spiked in serum. The SERS signal in the serum for all three assays is lower than that was observed in the buffer, which may be caused by the proteins in serum nonspecifically blocking some of the antibodies on the GeNP or on the test line reducing the number of specific binding events. Additionally, the serum may be less efficient at resuspending the dried GeNPs due to its higher viscosity. Dynamic linear detection ranges of 0.01-0.3 ng mL^{-1}, 0.03-0.077 ng mL^{-1}, and 4-52.3 ng mL^{-1} for cTnI, copeptin, and h-FABP in human serum samples were achieved, which successfully covered the clinically relevant ranges of these biomarkers. The lower end of the detection range in serum was calculated using three times of standard deviation on the background concentration of the serum solution used. Because of the strong signal from the GeNP, we obviated the need of extra steps of signal amplification used in other study to achieve the wanted sensitivity.[85]

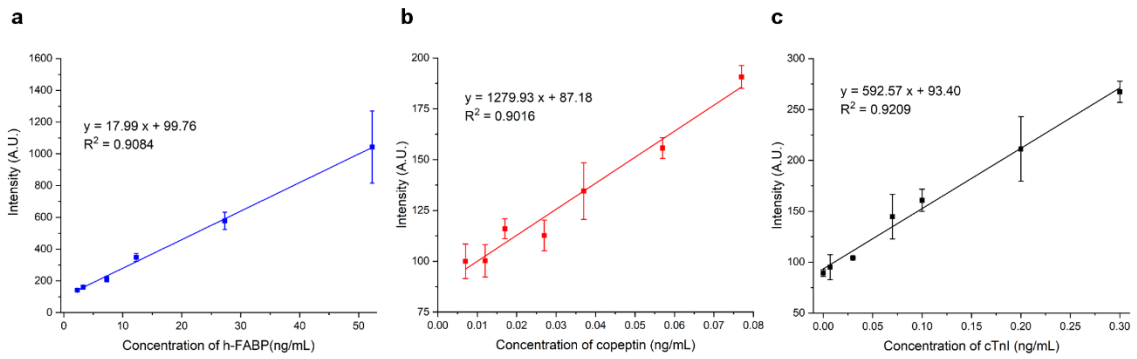

Figure 4.6 Response curve to different concentrations of (a) h-FABP, (b) copeptin, and (c) cTnI, respectively, in human serum. The peak intensities at different peaks were used for plotting the three response curves. 1591 cm^{-1} peak was used for h-FABP assay, 1556 cm^{-1} peak was used for cTnI assay, and 1632 cm^{-1} peak was used for copeptin assay. Error bars are mean ± SD (n = 3).

4.3.4. Multiplex detection of the biomarker panel on a single test line

As shown above, the three developed GeNPs have distinguishable peaks. We tested the performance of the GeNPs-based lateral flow assay for multiplex detection in a single test line using peak resolving. The performance was tested using different mixtures of cTnI, h-FABP, and copeptin, in human serum solutions. Figure 4.7(a) shows the spectra when detecting a mixture (0.07 ng mL^{-1} cTnI, 12.3 ng mL^{-1} h-FABP, and 0.037 ng mL^{-1} copeptin) using the multiplexed assay compared with when detecting 0.07 ng mL^{-1} cTnI, 12.3 ng mL^{-1} h-FABP, or 0.037 ng mL^{-1} copeptin using single biomarker assay. It can be observed that the peaks corresponding to each single biomarker were clearly observed in the spectra taken from the single test line. As shown in Figure 4.7(b), when testing Mixture 1, the SERS response for each biomarker in the multiplex assay was comparable to the

response observed in the single biomarker assay. Mixture 1 had low concentrations of each biomarker (0 ng mL^{-1} cTnI, 2.3 ng mL^{-1} h-FABP, 0.007 ng mL^{-1} copeptin). This result indicates there was no cross-reactivity among the three biomarkers in the developed multiplexed assay when all three biomarkers were at low concentration. When testing Mixture 2, which had higher concentration of the three biomarkers than Mixture 1, the signal in the multiplex assay was generally lower than the response observed in each single biomarker assay. This indicates some interference appeared when there were high concentrations of the three biomarkers. The interference may be caused by the decreased accessibility of the primary antibodies on the test line after large amount of biomarker bound to the antibodies on the test line and were crowed on the test line. This may then lead to a decreased response signal due to "hook effect". Base on the result, the signal from the mixture was about 0.87-0.92 times of the signal from the single biomarker sample, which still was a relatively small interference. Mixture 3, which had higher concentrations of the three biomarkers than Mixture 2, behaves very similar to Mixture 2. Only cTnI showed a larger signal in the multiplex detection than in the single biomarker sample (ratio>1), which may be due to the large standard deviation of this tests. Overall, our results indicate there was no cross-reactivity among the three biomarkers in the developed multiplexed assay for the detection of mixture samples with low concentrations of biomarkers and a relatively low cross-reactivity for mixture samples with high concentrations of biomarkers. In addition, statistical analysis (shown in Table C4, Figure C8, Figure C9, Figure C10 in Appendix C) was used to evaluate the SERS signals from the multiplex detection of mixtures and the SERS signals from the single-biomarker

detection. The statistical analysis results confirm there was a low cross-reactivity in the developed multiplexed assay.

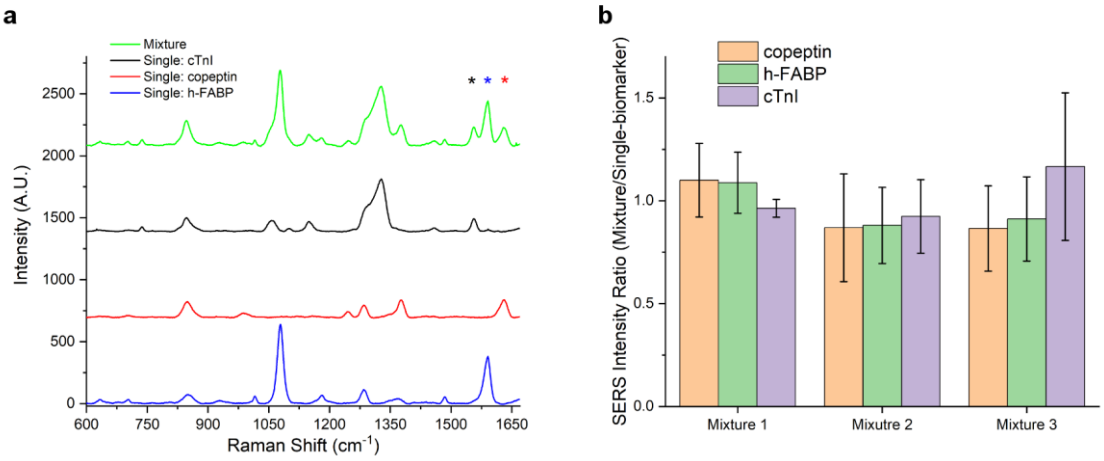

Figure 4.7 (a) Comparison of the spectrum of the multiplexed assay when detecting a mixture in serum solution composed of 0.07 ng mL^{-1} cTnI, 12.3 ng mL^{-1} h-FABP, and 0.037 ng mL^{-1} copeptin with the spectra of the single biomarker assays when detecting 0.07 ng mL^{-1} cTnI, 12.3 ng mL^{-1} h-FABP, and 0.037 ng mL^{-1} copeptin. (b) Comparison of the SERS signal in the multiplex assay and in the single biomarker assay when measuring the three mixture samples in serum solution. Mixture 1 has 0 ng mL^{-1} cTnI, 2.3 ng mL^{-1} h-FABP, and 0.007 ng mL^{-1} copeptin; Mixture 2 has 0.07 ng mL^{-1} cTnI, 12.3 ng mL^{-1} h-FABP, and 0.037 ng mL^{-1} copeptin; Mixture 3 has 0.1 ng mL^{-1} cTnI, 27.3 ng mL^{-1} h-FABP, 0.057 ng mL^{-1} copeptin. SERS intensity at 1591 cm^{-1} peak was used for h-FABP response, 1556 cm^{-1} peak was used for cTnI response, and 1632 cm^{-1} peak was used for copeptin response. Error bars are mean ± SD (n = 3).

4.4. Conclusion

In summary, we have developed a spectrally multiplexed multiplex assay on a paper strip for detection of the biomarker panel composed of cTnI, copeptin, and h-FABP. A gold-core and gold-shell GeNP, which could generate a strong SERS signal attributed to the inner nanogap between core and shell, was synthesized for the detection of these low-concentration biomarkers. We developed a new method to form the interior nanogap in the GeNP using RRM and 6-AHT. Strong Au-S bonds were formed on both core and shell side by using the RRM with a thiol group and introducing the 6-AHT as a linker. The strong bonds on both core and shell side and the covalent bond between RRM and 6-AHT led to a stable structure, which ensured the stable SERS signal generation from the GeNPs. The three GeNPs with different RRMs, showed differentiable SERS peaks (1556 cm^{-1} from DTNB, 1632 cm^{-1} from TFMBA, 1591 cm^{-1} from MPAA). Using the optimal amount of 6-AHT, GeNPs with gap sizes of 0.9-1.1 nm and shell thicknesses of 21-29 nm were formed. The SERS signals from GeNPs were 105-254 times higher than that from Au_{core}, confirming the large enhancement factor from GeNPs in SERS signal. The developed method to synthesize GeNPs, which is simple and able to embed with more RRM, can be expand to other RRMs in addition to DTNB, MPAA, ad TFMBA. Other linkers with different lengths can replace 6-AHT and be used to adjust the interior gap size of the GeNPs. The possibility of using different lengths linkers add the potential flexibility of adjusting the SERS enhancement factor by tuning the gap size.

In addition, the developed paper-based SERS assay based on the synthesized GeNPs achieved a sensitive detection of h-FABP (0.86-50 ng mL^{-1}), copeptin (0.004 -

0.07 ng mL^{-1}), and cTnI (0.01-0.1 ng mL^{-1}) in buffer samples. The detection ranges of the assay in serum samples also covered the clinically relevant range of the three biomarkers. Moreover, when detecting these three biomarkers simultaneously, the signal from the single test line was resolved by the differentiable SERS peaks from the GeNPs and a relatively low cross interference among the three biomarkers was observed. The developed paper-based assay strip avoided the complicated assay steps and ensured the simplicity, cost-effectiveness, and user-friendliness of the assay. The developed peak resolved multiplex assay using a single test line required less total volume of sample, lower total cost, shorter manufacturing time, less reagent, and shorter signal reading time than using single biomarker assays for each biomarker or using multiplex assay based on multiple test zones. Therefore, there is a strong potential for the developed peak-resolved assay to be utilized for biomarker panel analysis and on-site diagnosis of MI, especially at resource-limited clinical settings.

5. SUMMARY

Myocardial infarction (MI) is a problematic disease because of its prevalence, incidence, and high rate of mortality. Timely diagnosis of MI is essential for determining and implementing the treatment in a timely manner. In addition, early rule-out of non-MI patients and the consequent early discharge help to avoid the prolonged monitoring and the high cost of staying in hospitals. A biomarker test using a biomarker panel consisting of cTnI, copeptin, and h-FABP is needed for better diagnosis of MI and early ruling out the non-MI patients. To eventually improve patients' access to the diagnostic tests, especially in resource-limited settings, a cost-effective, user-friendly, and simple-to-use xPOCT sensing system for multiplex detection of the biomarker panel is largely needed. Efforts were made in this work to develop the xPOCT sensing system.

Among the three biomarkers for MI, cTnI is the one with the lowest molar concentrations in human blood. Thus, the first effort was made to develop a high-sensitivity single biomarker assay for the detection of cTnI. Specifically, an aptamer-based assay on a lateral flow assay strip for detection of cTnI was developed and characterized. A lateral flow assay strip was used to achieve simplicity, low cost, and user-friendliness of the assay. The aptamer was used because of its advantages, such as good thermal stability, good stability in a wide PH range, long shelf life, and low cost. A pair of aptamers, a primary aptamer and a secondary aptamer, that bounds to different sites of cTnI were used. The primary aptamer was immobilized on the nitrocellulose paper using biotin-streptavidin interaction. The secondary aptamer with an amine group was

immobilized on silica/MGITC/AuNP using TEPSA as a linker. MGITC, a molecule with electronic transitions near 638 nm, was used as an RRM on AuNP to achieve the resonance condition and generate a strong SERRS signal. The MGITC/AuNP was then encapsulated in a silica shell to form silica/MGITC/AuNP. The silica shell could improve SERS signal stability because it prevented the RRM from dissociating and prevented interfering molecules in a sample matrix from adsorbing on the surface of the metallic nanostructures. The size of the silica/MGITC/AuNP particle was around 129 nm. Two manual steps were needed in running the assay. The first step was to load 25 μL of sample and the second step was to add 50 μL of running buffer. The detection time of the assay was 40 mins. The developed assay achieved a detection range of 0.016-0.1 ng/mL for cTnI in buffer solution. The assay showed a low response to C-reactive protein, h-FABP, and B-type natriuretic peptide, indicating a good selectivity of the cTnI assay. In addition, the developed assay showed reasonable stability when it was stored at room temperature over 10 days. A good recovery rate was observed when using the assay for the detection of cTnI in spiked human serum samples, indicating the serum matrix had a low effect on the assay. Because the target detection range for cTnI is 0.01-0.1 ng/mL, the developed assay needs to be improved to extend the lower end of the detection range. In addition, two manual steps are still needed in the assay, thus a more automatic paper-based device is needed to make the assay easier to use.

A μPAD with wax printed channels, a horizontal motion mechanical valve, a paper arm, and a compressed sponge was designed to automatically finish multi-step processes. The developed μPAD showed good performance in both a two-step process and a four-

step process. To finish the two-step process, solution 2 was added to the washing buffer storage region on the μPAD, and solution 1 was added to the inlet. The solution flowed in the hydrophilic channel and was absorbed by the compressed sponge. The compressed sponge increased in height after it absorbed solution 1. The paper arm then transformed the vertical movement of the compressed sponge into a horizontal movement. The hydrophilic head at the tip of the paper arm then connected the washing solution storage region and the inlet, which allowed solution 2 to flow in the channel. The distance of the horizontal movement was correlated to the volume of solution 1 added. Specifically, the addition of 25 μL to 125 μL of solution 1 led to a horizontal movement of 0.4 mm to 3.4 mm. In addition, to improve the assay sensitivity, a localized dissolvable delay was designed and added to the μPAD to decrease the flow rate in the paper channel. A mixture of fructose and sucrose was used as the dissolvable material in the localized dissolvable delay. The good parameters to make the localized dissolvable delay was to drop 2.5 μL of 0.6 g/mL sucrose with 1.0 g/mL fructose at 15 mm position on the hydrophilic channel. The μPAD with this localized dissolvable delay successfully decreased the flow rate and doubled the flow time in the hydrophilic channel. The developed μPAD with the mechanical valve was successfully used to automate an aptamer-based SERS assay for cTnI, which has two steps (sample reaction and washing). The developed assay achieved a detection range of 0.02-0.5 ng/mL for cTnI in buffer solution. The sample volume was 75 μL and the detection time was more than 60 mins. Although the assay was more sensitive in the low concentration range in the μPAD with the dissolvable delay than the

μPAD without the delay, the assay needs to be improved to extend the lower end of the detection range.

To increase the sensitivity of the cTnI assay, a new SERS active particle, gap-enhanced nanoparticle, was developed. To overcome the limitation of currently reported methods in the synthesis of gap-enhanced particles, a modified method using RRM-based spacer was developed. Three gap-enhanced particles with different RRMs (DTNB, MPAA, TFMBA) in each particle was successfully synthesized. The synthesized gap-enhanced particles showed gap sizes of 0.9-1.1 nm and shell thicknesses of 21-29 nm. The nanometer gap largely enhanced the SERS signal and the gold shell protected the RRM and ensured a stable SERS signal. In addition, antibodies with a high affinity and high specificity to cTnI were used as the recognition element. The primary antibody was immobilized on a test line and the secondary antibody was immobilized on the gap-enhanced particle. Using the above components, a single biomarker assay for cTnI was developed on a lateral flow assay strip. The size of the gap-enhanced nanoparticle used in the cTnI assay was around 94.6 nm. Two manual steps were needed in running the assay. The first step was to load 50 μL of sample and the second step was to add 50 μL of washing buffer. The detection time of the assay was around 27 mins. The developed single biomarker assay achieved a detection range of 0.01-0.1 ng/mL for cTnI in buffer solution, which covered its clinically relevant range. Using a similar setup, assay for copeptin was developed and achieved a detection range of 0.004 -0.07 ng/mL, and assay for h-FABP was developed and achieved a detection range of 0.86-50 ng/mL. The assays were also tested in serum samples and showed a good performance. Using the gap-enhanced

particles with different RRMs, multiplex detection of the three biomarkers in a single test line was achieved. The three gap-enhanced particles made with different RRMs showed differentiable SERS peaks. The signal from each biomarker on a single test line was resolved by the differentiable peaks of different RRMs in SERS active particles (1556 cm^{-1} from DTNB for cTnI, 1632 cm^{-1} from TFMBA for copeptin, 1591 cm^{-1} from MPAA for h-FABP). When detecting these three biomarkers simultaneously, a relatively low cross-interference among the three biomarkers was observed.

The developed multiplex assay for detection of cTnI, copeptin, and h-FABP was a cost-effective, user-friendly, and simple-to-use system. When detecting spiked human serum samples, the quantitative assays successfully covered 5-16.8 ng/mL for the detection of h-FABP, partially covered 0.004-0.056 ng/mL for the detection of copeptin, and successfully covered 0.01-0.1 ng/mL for the detection of cTnI. The detection range of the assay for copeptin in serum samples was 0.03-0.077 ng/mL. Although it didn't cover the concentrations in healthy humans (0.004-0.018 ng/mL), this range covered the clinical cut-off value of copeptin to indicate MI (0.056 ng/mL) and was sufficient in this application. The detection time of the assay was within 60 minutes. With these features, the developed assay shows some potential to be used in the xPOCT sensing system, to improve patients' access to diagnostic tests, especially in resource-limited settings.

Several aspects of work could be continued in future work. Firstly, more RRMs in addition to DTNB, MPAA, and TFMBA, can be used to synthesize gap-enhanced particles. Using more gap-enhanced particles with differentiable peaks, simultaneous detection of four or more biomarkers could be achieved. Secondly, in the synthesis of gap-

enhanced particles, other linkers with different lengths can replace 6-AHT and be used to adjust the interior gap size of the gap-enhanced particles. The possibility of using different lengths linkers add the potential flexibility of adjusting the SERS enhancement factor by tuning the gap size. Thirdly, in the synthesis of gap-enhanced particles, the core size and the shell thickness of the gap-enhanced particles can be adjusted to achieve an optimal signal. Lastly, the μPAD with the mechanical valve can be combined with the developed lateral flow strip to automate the multiplex assay for detection of cTnI, copeptin, and h-FABP (two steps: sample reaction and washing).

REFERENCES

1. Hansson, G.K., *Inflammation, Atherosclerosis, and Coronary Artery Disease.* The New England Journal of Medicine, 2005. **352**(16): p. 1685-1695.
2. Bentzon, J.F., et al., *Mechanisms of Plaque Formation and Rupture.* Circulation Research, 2014. **114**(12): p. 1852-1866.
3. Rafieian-Kopaei, M., et al., *Atherosclerosis: Process, Indicators, Risk Factors and New Hopes.* International Journal of Preventive Medicine, 2014. **5**(8): p. 927-946.
4. Sandfort, V., J.A. Lima, and D.A. Bluemke, *Noninvasive Imaging of Atherosclerotic Plaque Progression: Status of Coronary Computed Tomography Angiography.* Circulation: Cardiovascular Imaging, 2015. **8**(7): p. e003316.
5. Davies, M.J., *The Pathophysiology of Acute Coronary Syndromes.* Heart, 2000. **83**(3): p. 361-366.
6. Dave, T., et al., *Plaque Regression and Plaque Stabilisation in Cardiovascular Diseases.* Indian Journal of Endocrinology and Metabolism, 2013. **17**(6): p. 983-989.
7. Amsterdam, E.A., et al., *2014 AHA/ACC Guideline for the Management of Patients with Non-ST-Elevation Acute Coronary Syndromes: a report of the American College of Cardiology/American Heart Association Task Force on Practice Guidelines.* Journal of the American College of Cardiology, 2014. **64**(24): p. e139-e228.

8. Thygesen, K., et al., *Fourth Universal Definition of Myocardial Infarction (2018).* Journal of the American College of Cardiology, 2018. **72**(18): p. 2231-2264.

9. Benjamin, E.J., et al., *Heart Disease and Stroke Statistics-2018 Update: A Report From the American Heart Association.* Circulation, 2018. **137**(12): p. e67-e492.

10. Bhatnagar, P., et al., *The Epidemiology of Cardiovascular Disease in the UK 2014.* Heart, 2015. **101**(15): p. 1182-1189.

11. Benjamin, E.J., et al., *Heart Disease and Stroke Statistics-2019 Update A Report From the American Heart Association.* Circulation, 2019. **139**(10): p. E56-E528.

12. WHO. *Cardiovascular Diseases (CVDs)*. 2017 [cited 2021 February 14]; Available from: https://www.who.int/news-room/fact-sheets/detail/cardiovascular-diseases-(cvds).

13. Pedigo, A., T. Aldrich, and A. Odoi, *Neighborhood Disparities in Stroke and Myocardial Infarction Mortality: a GIS and Spatial Scan Statistics Approach.* Bmc Public Health, 2011. **11**: p. 644.

14. Patel, S.A., et al., *County-Level Variation in Cardiovascular Disease Mortality in the United States in 2009-2013: Comparative Assessment of Contributing Factors.* American Journal of Epidemiology, 2016. **184**(12): p. 933-942.

15. Graham, G.N., et al., *Racial Disparities in Patient Characteristics and Survival After Acute Myocardial Infarction.* Jama Network Open, 2018. **1**(7): p. e184240.

16. Antman, E.M., et al., *ACC/AHA Guidelines for the Management of Patients with ST-elevation Myocardial Infarction--Executive Summary: a Report of the*

American College of Cardiology/American Heart Association Task Force on Practice Guidelines (Writing Committee to Revise the 1999 Guidelines for the Management of Patients With Acute Myocardial Infarction). Circulation, 2004. **110**(5): p. 588-636.

17. Antman, E.M., et al., *ACC/AHA Guidelines for the Management of Patients with ST-elevation Myocardial Infarction: a Report of the American College of Cardiology/American Heart Association Task Force on Practice Guidelines (Committee to Revise the 1999 Guidelines for the Management of Patients with Acute Myocardial Infarction).* Circulation, 2004. **110**(9): p. e82-e292.
18. Smith, S.C., et al., *ACC/AHA Guidelines for Percutaneous Coronary Intervention (Revision of the 1993 PTCA Guidelines) - Executive Summary - A Report of the American College of Cardiology/American Heart Association Task Force on Practice Guidelines (Committee to Revise the 1993 Guidelines for Percutaneous Transluminal Coronary Angioplasty) - Endorsed by the Society for Cardiac Angiography and Interventions.* Circulation, 2001. **103**(24): p. 3019-3041.
19. Ahmad, M., et al. *Percutaneous Coronary Intervention*. 2021 [cited 2021 February 19]; Available from: https://www.ncbi.nlm.nih.gov/books/NBK556123/.
20. Malik, T.F. and V.S. Tivakaran, *Percutaneous Transluminal Coronary Angioplasty*, in *StatPearls*. 2021: Treasure Island (FL).

21. Brodie, B.R., et al., *Importance of Time to Reperfusion for 30-day and Late Survival and Recovery of Left Ventricular Function After Primary Angioplasty for Acute Myocardial Infarction.* Journal of the American College of Cardiology, 1998. **32**(5): p. 1312-1319.

22. Brodie, B.R., et al., *Importance of Time to Reperfusion on Outcomes with Primary Coronary Angioplasty for Acute Myocardial Infarction (Results from the Stent Primary Angioplasty in Myocardial Infarction Trial).* American Journal of Cardiology, 2001. **88**(10): p. 1085-1090.

23. Association, A.H. *Heart Procedures and Surgeries*. Treatment of a Heart Attack 2021 [cited 2021 April 24]; Available from: https://www.heart.org/en/health-topics/heart-attack/treatment-of-a-heart-attack/cardiac-procedures-and-surgeries.

24. Twerenbold, R., et al., *Clinical Use of High-Sensitivity Cardiac Troponin in Patients With Suspected Myocardial Infarction.* Journal of the American College of Cardiology, 2017. **70**(8): p. 996-1012.

25. Stepinska, J., et al., *Diagnosis and Risk Stratification of Chest Pain Patients in the Emergency Department: Focus on Acute Coronary Syndromes. A Position Paper of the Acute Cardiovascular Care Association.* Eur Heart J Acute Cardiovasc Care, 2020. **9**(1): p. 76-89.

26. O'Gara, P.T., et al., *2013 ACCF/AHA Guideline for the Management of St-elevation Myocardial Infarction: a Report of the American College of Cardiology Foundation/American Heart Association Task Force on Practice*

Guidelines. Journal of the American College of Cardiology, 2013. **61**(4): p. e78-e140.

27. Lambert, L., et al., *Association Between Timeliness of Reperfusion Therapy and Clinical Outcomes in ST-Elevation Myocardial Infarction.* JAMA, 2010. **303**(21): p. 2148-2155.

28. Wildi, K., et al., *Safety and Efficacy of the 0 h/3 h Protocol for Rapid Rule Out of Myocardial Infarction.* American Heart Journal, 2016. **181**: p. 16-25.

29. Ryan, T.J., et al., *ACC/AHA Guidelines for the Management of Patients With Acute Myocardial Infarction. A Report of the American College of Cardiology/American Heart Association Task Force on Practice Guidelines (Committee on Management of Acute Myocardial Infarction).* Journal of the American College of Cardiology, 1996. **28**(5): p. 1328-428.

30. Makam, A.N. and O.K. Nguyen, *Use of Cardiac Biomarker Testing in the Emergency Department.* Jama Internal Medicine, 2015. **175**(1): p. 67-75.

31. Ouyang, M.X., et al., *A Review of Biosensor Technologies for Blood Biomarkers Toward Monitoring Cardiovascular Diseases at the Point-of-care.* Biosensors and Bioelectronics, 2021. **171**: p. 112621.

32. Dzoyem, J.P., V. Kuete, and J.N. Eloff, *23 - Biochemical Parameters in Toxicological Studies in Africa: Significance, Principle of Methods, Data Interpretation, and Use in Plant Screenings*, in *Toxicological Survey of African Medicinal Plants*, V. Kuete, Editor. 2014, Elsevier. p. 659-715.

33. Ohtsuki, I. and S. Morimoto, *Troponin*, in *Encyclopedia of Biological Chemistry (Second Edition)*, W.J. Lennarz and M.D. Lane, Editors. 2013, Academic Press: Waltham. p. 445-449.

34. O'Brien, P., et al. *Review of Qualification Data for Cardiac Troponins*. 2011 [cited 2021 February 19]; Available from: https://www.fda.gov/media/87774/download.

35. Jneid, H., et al., *2017 AHA/ACC Clinical Performance and Quality Measures for Adults With ST-Elevation and Non-ST-Elevation Myocardial Infarction: A Report of the American College of Cardiology/American Heart Association Task Force on Performance Measures.* Journal of the American College of Cardiology, 2017. **70**(16): p. 2048-2090.

36. Gore, M.O., et al., *Age- and Sex-Dependent Upper Reference Limits for the High-Sensitivity Cardiac Troponin T Assay.* Journal of the American College of Cardiology, 2014. **63**(14): p. 1441-1448.

37. Sandoval, Y., et al., *Diagnosis of Type 1 and Type 2 Myocardial Infarction Using a High-Sensitivity Cardiac Troponin I Assay with Sex-Specific 99th Percentiles Based on the Third Universal Definition of Myocardial Infarction Classification System.* Clinical Chemistry, 2015. **61**(4): p. 657-663.

38. Neumann, J.T., et al., *Diagnosis of Myocardial Infarction Using a High-sensitivity Troponin I 1-hour Algorithm.* JAMA cardiology, 2016. **1**(4): p. 397-404.

39. Bhatia, P.M. and L.B. Daniels, *Highly Sensitive Cardiac Troponins: The Evidence Behind Sex-Specific Cutoffs.* Journal of the American Heart Association, 2020. **9**(10): p. e015272.

40. Venge, P., et al., *Clinical Performance of Two Highly Sensitive Cardiac Troponin I Assays.* Clinical Chemistry, 2009. **55**(1): p. 109-116.

41. Hines, M.T., *Chapter 7 - Clinical Approach to Commonly Encountered Problems*, in *Equine Internal Medicine (Fourth Edition)*, S.M. Reed, W.M. Bayly, and D.C. Sellon, Editors. 2018, W.B. Saunders. p. 232-310.

42. Reichlin, T., et al., *Incremental Value of Copeptin for Rapid Rule Out of Acute Myocardial Infarction.* Journal of the American College of Cardiology, 2009. **54**(1): p. 60-68.

43. Nobian, A., A. Mohamed, and I. Spyridopoulos, *The Role of Arginine Vasopressin in Myocardial Infarction and Reperfusion.* Kardiologia Polska, 2019. **77**(10): p. 908-917.

44. Morgenthaler, N.G., et al., *Copeptin: Clinical Use of a New Biomarker.* Trends in endocrinology & metabolism, 2008. **19**(2): p. 43-49.

45. Loughrey, C.M. and I.S. Young, *CHAPTER 38 - Clinical Biochemistry of the Cardiovascular System*, in *Clinical Biochemistry: Metabolic and Clinical Aspects (Third Edition)*, W.J. Marshall, et al., Editors. 2014, Churchill Livingstone. p. 737-766.

46. Roffi, M., et al., *2015 ESC Guidelines for the Management of Acute Coronary Syndromes in Patients Presenting Without Persistent ST-segment Elevation: Task*

Force for the Management of Acute Coronary Syndromes in Patients Presenting without Persistent ST-Segment Elevation of the European Society of Cardiology (ESC). European heart journal, 2016. **37**(3): p. 267-315.

47. Raskovalova, T., et al., *Diagnostic Accuracy of Combined Cardiac Troponin and Copeptin Assessment for Early Rule-out of Myocardial Infarction: a Systematic Review and Meta-analysis.* Eur Heart J Acute Cardiovasc Care, 2014. **3**(1): p. 18-27.

48. Keller, T., et al., *Copeptin Improves Early Diagnosis of Acute Myocardial Infarction.* Journal of the American College of Cardiology, 2010. **55**(19): p. 2096-2106.

49. Möckel, M., et al., *Early Discharge Using Single Cardiac Troponin and Copeptin Testing in Patients With Suspected Acute Coronary Syndrome (ACS): a Randomized, Controlled Clinical Process Study.* European heart journal, 2015. **36**(6): p. 369-376.

50. Ray, P., et al., *Combined Copeptin and Troponin to Rule out Myocardial Infarction in Patients with Chest Pain and a History of Coronary Artery Disease.* The American Journal of Emergency Medicine, 2012. **30**(3): p. 440-448.

51. Mueller, C., *Biomarkers and Acute Coronary Syndromes: an Update.* European heart journal, 2014. **35**(9): p. 552-556.

52. Smith, G.S., G.L. Walter, and R.M. Walker, *Chapter 18 - Clinical Pathology in Non-Clinical Toxicology Testing*, in *Haschek and Rousseaux's Handbook of*

Toxicologic Pathology (Third Edition), W.M. Haschek, C.G. Rousseaux, and M.A. Wallig, Editors. 2013, Academic Press: Boston. p. 565-594.

53. Reiter, M., et al., *Heart-type Fatty Acid-binding Protein in the Early Diagnosis of Acute Myocardial Infarction.* Heart, 2013. **99**(10): p. 708-714.

54. Ye, X.-d., et al., *Heart-Type Fatty Acid Binding Protein (H-FABP) as a Biomarker for Acute Myocardial Injury and Long-Term Post-Ischemic Prognosis.* Acta pharmacologica sinica, 2018. **39**(7): p. 1155-1163.

55. Morrow, D.A., et al., *National Academy of Clinical Biochemistry Laboratory Medicine Practice Guidelines: Clinical characteristics and utilization of biochemical markers in acute coronary syndromes.* Circulation, 2007. **115**(13): p. e356-e375.

56. Inoue, K., et al., *Heart Fatty Acid-binding Protein Offers Similar Diagnostic Performance to High-sensitivity Troponin T in Emergency Room Patients Presenting With Chest Pain.* Circulation Journal, 2011. **75**(12): p. 2813-2820.

57. Slot, M.H.E.B., et al., *Heart-type Fatty Acid-binding Protein in the Early Diagnosis of Acute Myocardial Infarction: a Systematic Review and Meta-analysis.* Heart, 2010. **96**(24): p. 1957-1963.

58. McCann, C.J., et al., *Novel Biomarkers in Early Diagnosis of Acute Myocardial Infarction Compared With Cardiac Troponin T.* European Heart Journal, 2008. **29**(23): p. 2843-2850.

59. Viswanathan, K., et al., *Heart-type Fatty Acid-binding Protein Predicts Long-term Mortality and Re-infarction in Consecutive Patients With Suspected Acute*

Coronary Syndrome Who Are Troponin-negative. Journal of the American College of Cardiology, 2010. **55**(23): p. 2590-2598.

60. McMahon, C.G., et al., *Diagnostic Accuracy of Heart-Type Fatty Acid–Binding Protein for the Early Diagnosis of Acute Myocardial Infarction.* The American Journal of Emergency Medicine, 2012. **30**(2): p. 267-274.

61. O'Donoghue, M., et al., *Prognostic Utility of Heart-type Fatty Acid Binding Protein in Patients With Acute Coronary Syndromes.* Circulation, 2006. **114**(6): p. 550-557.

62. Carroll, C., et al., *Heart-type Fatty Acid Binding Protein as an Early Marker for Myocardial Infarction: Systematic Review and Meta-analysis.* Emergency Medicine Journal, 2013. **30**(4): p. 280-286.

63. Liao, J., et al., *Human Heart-type Fatty Acid-binding Protein for on-site Diagnosis of Early Acute Myocardial Infarction.* International Journal of Cardiology, 2009. **133**(3): p. 420-423.

64. Drain, P.K., et al., *Diagnostic Point-of-care Tests in Resource-limited Settings.* The Lancet Infectious Diseases, 2014. **14**(3): p. 239-249.

65. Syedmoradi, L., et al., *Point of Care Testing: The Impact of Nanotechnology.* Biosensors and Bioelectronics, 2017. **87**: p. 373-387.

66. St John, A. and C.P. Price, *Existing and Emerging Technologies for Point-of-Care Testing.* The Clinical Biochemist Reviews, 2014. **35**(3): p. 155-167.

67. Land, K.J., et al., *REASSURED Diagnostics to Inform Disease Control Strategies, Strengthen Health Systems and Improve Patient Outcomes.* Nature Microbiology, 2019. **4**(1): p. 46-54.

68. Dincer, C., et al., *Multiplexed Point-of-Care Testing - xPOCT.* Trends Biotechnol, 2017. **35**(8): p. 728-742.

69. Wu, Y., et al., *Emerging Design Strategies for Constructing Multiplex Lateral Flow Test Strip Sensors.* Biosensors and Bioelectronics, 2020. **157**: p. 112168.

70. Chon, H., et al., *SERS-based Competitive Immunoassay of Troponin I and CK-MB Markers for Early Diagnosis of Acute Myocardial Infarction.* Chemical Communications, 2014. **50**(9): p. 1058-1060.

71. Su, Y., et al., *Plasmon Near-Field Coupling of Bimetallic Nanostars and a Hierarchical Bimetallic SERS "Hot Field": Toward Ultrasensitive Simultaneous Detection of Multiple Cardiorenal Syndrome Biomarkers.* Analytical Chemistry, 2019. **91**(1): p. 864-872.

72. Zhang, D., et al., *Quantitative Detection of Multiplex Cardiac Biomarkers With Encoded SERS Nanotags on a Single T Line in Lateral Flow Assay.* Sensors and Actuators B-Chemical, 2018. **277**: p. 502-509.

73. Li, X.Z., et al., *Surface-enhanced Raman Spectroscopy (SERS)-based Immunochromatographic Assay (ICA) for the Simultaneous Detection of Two Pyrethroid Pesticides.* Sensors and Actuators B-Chemical, 2019. **283**: p. 230-238.

74. Zhang, D., et al., *Quantitative and Ultrasensitive Detection of Multiplex Cardiac Biomarkers in Lateral Flow Assay With Core-shell Sers Nanotags.* Biosensors and Bioelectronics, 2018. **106**: p. 204-211.

75. Han, M.M., et al., *An Octuplex Lateral Flow Immunoassay for Rapid Detection of Antibiotic Residues, Aflatoxin M-1 and Melamine in Milk.* Sensors and Actuators B-Chemical, 2019. **292**: p. 94-104.

76. Anfossi, L., et al., *Silver and Gold Nanoparticles as Multi-chromatic Lateral Flow Assay Probes for the Detection of Food Allergens.* Analytical and Bioanalytical Chemistry, 2019. **411**(9): p. 1905-1913.

77. Zhang, D., et al., *Rapid and Ultrasensitive Quantification of Multiplex Respiratory Tract Infection Pathogen via Lateral Flow Microarray based on SERS Nanotags.* Theranostics, 2019. **9**(17): p. 4849-4859.

78. Byzova, N.A., et al., *Development of a Lateral Flow Highway: Ultra-Rapid Multitracking Immunosensor for Cardiac Markers.* Sensors, 2019. **19**(24): p. 5494.

79. Kaur, A. and S. Dhakal, *Recent Applications of FRET-based Multiplexed Techniques.* Trends in Analytical Chemistry, 2020. **123**: p. 115777.

80. Di Nardo, F., et al., *Colour-encoded Lateral Flow Immunoassay for the Simultaneous Detection of Aflatoxin B1 and Type-B Fumonisins in a Single Test Line.* Talanta, 2019. **192**: p. 288-294.

81. Wang, W.W., et al., *A Novel Immunochromatographic Assay Based on a Time-resolved Chemiluminescence Strategy for the Multiplexed Detection of Ractopamine and Clenbuterol.* Analytica Chimica Acta, 2016. **917**: p. 79-84.

82. Sun, J.Y., et al., *Multiplexed Electrochemical and SERS Dual-mode Detection of Stroke Biomarkers: Rapid Screening With High Sensitivity.* New Journal of Chemistry, 2019. **43**(34): p. 13381-13387.

83. Zhao, J.W., et al., *A Novel Potential-resolved Electrochemiluminescence Immunosensor for the Simultaneous Determination of Brain Natriuretic Peptide and Cardiac Troponin I.* Sensors and Actuators B: Chemical, 2020. **311**: p. 127934.

84. Tang, L. and J. Casas, *Quantification of Cardiac Biomarkers Using Label-free and Multiplexed Gold Nanorod Bioprobes for Myocardial Infarction Diagnosis.* Biosensors and Bioelectronics, 2014. **61**: p. 70-75.

85. Li, F., et al., *Multiplexed Chemiluminescence Determination of Three Acute Myocardial Infarction Biomarkers Based on Microfluidic Paper-based Immunodevice Dual Amplified by Multifunctionalized Gold Nanoparticles.* Talanta, 2020. **207**: p. 120346.

86. Wilson, R., A.R. Cossins, and D.G. Spiller, *Encoded Microcarriers for High-throughput Multiplexed Detection.* Angewandte Chemie International Edition, 2006. **45**(37): p. 6104-6117.

87. Perez-Jimenez, A.I., et al., *Surface-enhanced Raman Spectroscopy: Benefits, Trade-offs and Future Developments.* Chemical Science, 2020. **11**(18): p. 4563-4577.

88. Langer, J., et al., *Present and Future of Surface-Enhanced Raman Scattering.* Acs Nano, 2020. **14**(1): p. 28-117.

89. Lane, L.A., X. Qian, and S. Nie, *SERS Nanoparticles in Medicine: From Label-Free Detection to Spectroscopic Tagging.* Chemical Reviews, 2015. **115**(19): p. 10489-10529.

90. Rousseau, D.L. and M.R. Ondrias, *Raman Scattering*, in *Optical Techniques in Biological Research*, D.L. Rousseau, Editor. 1984, Academic Press. p. 65-132.

91. Schlucker, S., *SERS Microscopy: Nanoparticle Probes and Biomedical Applications.* Chemphyschem, 2009. **10**(9-10): p. 1344-1354.

92. Kneipp, J., H. Kneipp, and K. Kneipp, *SERS—A Single-molecule and Nanoscale Tool for Bioanalytics.* Chemical Society Reviews, 2008. **37**(5): p. 1052-1060.

93. Moskovits, M., *Surface-enhanced Raman Spectroscopy: A Brief Retrospective.* Journal of Raman Spectroscopy, 2005. **36**(6-7): p. 485-496.

94. Petryayeva, E. and U.J. Krull, *Localized Surface Plasmon Resonance: Nanostructures, Bioassays and Biosensing—A Review.* Analytica Chimica Acta, 2011. **706**(1): p. 8-24.

95. Doering, W.E. and S. Nie, *Single-Molecule and Single-Nanoparticle SERS: Examining the Roles of Surface Active Sites and Chemical Enhancement.* The Journal of Physical Chemistry B, 2002. **106**(2): p. 311-317.

96. Yu, X.X., et al., *Tuning Chemical Enhancement of SERS by Controlling the Chemical Reduction of Graphene Oxide Nanosheets.* Acs Nano, 2011. **5**(2): p. 952-958.

97. Wang, Y.Q., B. Yan, and L.X. Chen, *SERS Tags: Novel Optical Nanoprobes for Bioanalysis.* Chemical Reviews, 2013. **113**(3): p. 1391-1428.

98. Li, Y., et al., *Raman Tags: Novel Optical Probes for Intracellular Sensing and Imaging.* Biotechnology Advances, 2017. **35**(2): p. 168-177.

99. Khlebtsov, N.G., et al., *Gap-enhanced Raman Tags: Fabrication, Optical Properties, and Theranostic Applications.* Theranostics, 2020. **10**(5): p. 2067-2094.

100. Hong, S.M. and X. Li, *Optimal Size of Gold Nanoparticles for Surface-Enhanced Raman Spectroscopy under Different Conditions.* Journal of Nanomaterials, 2013. **2013**: p. 790323

101. Reguera, J., et al., *Anisotropic Metal Nanoparticles for Surface Enhanced Raman Scattering.* Chemical Society Reviews, 2017. **46**(13): p. 3866-3885.

102. Israelsen, N.D., C. Hanson, and E. Vargis, *Nanoparticle Properties and Synthesis Effects on Surface-enhanced Raman Scattering Enhancement Factor: An Introduction.* The Scientific World Journal, 2015. **2015**: p. 124582.

103. Kumar, G.V.P., *Plasmonic Nano-architectures for Surface Enhanced Raman Scattering: A Review.* Journal of Nanophotonics, 2012. **6**: p. 064503.

104. Kleinman, S.L., et al., *Creating, Characterizing, and Controlling Chemistry With SERS Hot Spots.* Physical Chemistry Chemical Physics, 2013. **15**(1): p. 21-36.

105. Song, J.B., et al., *SERS-Encoded Nanogapped Plasmonic Nanoparticles: Growth of Metallic Nanoshell by Templating Redox-Active Polymer Brushes.* Journal of the American Chemical Society, 2014. **136**(19): p. 6838-6841.

106. Chen, G., et al., *High-purity Separation of Gold Nanoparticle Dimers and Trimers.* Journal of the American Chemical Society, 2009. **131**(12): p. 4218-4219.

107. Zhang, Y., et al., *Ultrabright Gap-enhanced Raman Tags for High-speed Bioimaging.* Nature Communications, 2019. **10**(1): p. 3905.

108. Lin, L., H.C. Gu, and J. Ye, *Plasmonic Multi-shell Nanomatryoshka Particles as Highly Tunable SERS Tags With Built-in Reporters.* Chemical Communications, 2015. **51**(100): p. 17740-17743.

109. Oh, J.W., et al., *Thiolated DNA-Based Chemistry and Control in the Structure and Optical Properties of Plasmonic Nanoparticles with Ultrasmall Interior Nanogap.* Journal of the American Chemical Society, 2014. **136**(40): p. 14052-14059.

110. Zhou, Y. and P. Zhang, *Simultaneous SERS and Surface-enhanced Fluorescence From Dye-embedded Metal Core-shell Nanoparticles.* Physical Chemistry Chemical Physics, 2014. **16**(19): p. 8791-8794.

111. Zhou, Y., et al., *Engineering Versatile SERS-active Nanoparticles by Embedding Reporters Between Au-core/Ag-shell Through Layer-by-layer Deposited Polyelectrolytes.* Journal of Materials Chemistry C, 2013. **1**(23): p. 3695-3699.

112. Ayala-Orozco, C., et al., *Fluorescence Enhancement of Molecules Inside a Gold Nanomatryoshka.* Nano Letters, 2014. **14**(5): p. 2926-2933.

113. Gandra, N. and S. Singamaneni, *Bilayered Raman-Intense Gold Nanostructures with Hidden Tags (BRIGHTs) for High-Resolution Bioimaging.* Advanced Materials, 2013. **25**(7): p. 1022-1027.

114. Sharma, B., et al., *SERS: Materials, Applications, and the Future.* Materials Today, 2012. **15**(1-2): p. 16-25.

115. McNay, G., et al., *Surface-Enhanced Raman Scattering (SERS) and Surface-Enhanced Resonance Raman Scattering (SERRS): A Review of Applications.* Applied Spectroscopy, 2011. **65**(8): p. 825-837.

116. Qian, X.M., et al., *In Vivo Tumor Targeting and Spectroscopic Detection With Surface-enhanced Raman Nanoparticle Tags.* Nature Biotechnology, 2008. **26**(1): p. 83-90.

117. Boca, S., et al., *Flower-shaped Gold Nanoparticles: Synthesis, Characterization and Their Application as SERS-active Tags Inside Living Cells.* Nanotechnology, 2011. **22**(5): p. 055702.

118. Pallaoro, A., et al., *Mapping Local pH in Live Cells Using Encapsulated Fluorescent SERS Nanotags.* Small, 2010. **6**(5): p. 618-622.

119. Chen, M., et al., *High-sensitive Bioorthogonal SERS Tag for Live Cancer Cell Imaging by Self-assembling Core-satellites Structure Gold-silver Nanocomposite.* Talanta, 2017. **172**: p. 176-181.

120. Fales, A.M., H. Yuan, and T. Vo-Dinh, *Silica-coated Gold Nanostars for Combined Surface-enhanced Raman Scattering (SERS) Detection and Singlet-oxygen Generation: a Potential Nanoplatform for Theranostics.* Langmuir, 2011. **27**(19): p. 12186-12190.

121. Lee, S., et al., *Rapid and Sensitive Phenotypic Marker Detection on Breast Cancer Cells Using Surface-enhanced Raman Scattering (SERS) Imaging.* Biosensors and Bioelectronics, 2014. **51**: p. 238-243.

122. Doering, W.E. and S.M. Nie, *Spectroscopic Tags Using Dye-embedded Nanoparticles and Surface-enhanced Raman Scattering.* Analytical Chemistry, 2003. **75**(22): p. 6171-6176.

123. Khlebtsov, B.N., et al., *SERS-based Lateral Flow Immunoassay of Troponin I by Using Gap-enhanced Raman Tags.* Nano Research, 2019. **12**(2): p. 413-420.

124. Zhao, Y., et al., *Gap-Tethered Au@AgAu Raman Tags for the Ratiometric Detection of MC-LR.* Analytical Chemistry, 2019. **91**(11): p. 7162-7172.

125. Hu, C.Y., et al., *Highly Narrow Nanogap-containing Au@Au Core-shell SERS Nanoparticles: Size-dependent Raman Enhancement and Applications in Cancer Cell Imaging.* Nanoscale, 2016. **8**(4): p. 2090-2096.

126. Lee, J.H., et al., *Synthesis, Optical Properties, and Multiplexed Raman Bio-Imaging of Surface Roughness-Controlled Nanobridged Nanogap Particles.* Small, 2016. **12**(34): p. 4726-4734.

127. Lim, D.K., et al., *Highly Uniform and Reproducible Surface-enhanced Raman Scattering From DNA-tailorable Nanoparticles With 1-nm Interior Gap.* Nature Nanotechnology, 2011. **6**(7): p. 452-460.

128. Kim, J.M., et al., *Cyclodextrin-Based Synthesis and Host-Guest Chemistry of Plasmonic Nanogap Particles with Strong, Quantitative, and Highly Multiplexable Surface-Enhanced Raman Scattering Signals.* Journal of Physical Chemistry Letters, 2020. **11**(19): p. 8358-8364.

129. Khanadeev, V., et al., *SERS Response From Gap-enhanced Raman Tags as a Function of the Shell Thickness.* Saratov Fall Meeting 2019: Optical and Nano-Technologies for Biology and Medicine,, 2020. **11457**: p. 114570z.

130. Gu, Y.Q., et al., *Raman Photostability of Off-resonant Gap-enhanced Raman Tags.* Rsc Advances, 2018. **8**(26): p. 14434-14444.

131. Gu, Y.Q., et al., *Gap-enhanced Raman Tags for Physically Unclonable Anticounterfeiting Labels.* Nature Communications, 2020. **11**(1): p. 516.

132. Wu, L., et al., *Simultaneous Evaluation of p53 and p21 Expression Level for Early Cancer Diagnosis Using SERS Technique.* Analyst, 2013. **138**(12): p. 3450-3456.

133. Gellner, M., K. Kompe, and S. Schlucker, *Multiplexing with SERS Labels Using Mixed SAMs of Raman Reporter Molecules.* Analytical and Bioanalytical Chemistry, 2009. **394**(7): p. 1839-1844.

134. Kaminska, A., et al., *SERS-based Immunoassay in a Microfluidic System for the Multiplexed Recognition of Interleukins from Blood Plasma: Towards Picogram Detection.* Scientific Reports, 2017. **7**: p. 10656.

135. Salehi, M., et al., *Two-color SERS Microscopy for Protein Co-localization in Prostate Tissue With Primary Antibody-protein A/G-gold Nanocluster Conjugates.* Nanoscale, 2014. **6**(4): p. 2361-2367.

136. Nima, Z.A., et al., *Circulating Tumor Cell Identification by Functionalized Silver-gold Nanorods With Multicolor, Super-enhanced SERS and Photothermal Resonances.* Scientific Reports 2014. **4**: p. 4752.

137. Lai, Y.M., et al., *Raman-encoded Microbeads for Spectral Multiplexing With SERS Detection.* Rsc Advances, 2015. **5**(18): p. 13762-13767.

138. Morales, M.A. and J.M. Halpern, *Guide to Selecting a Biorecognition Element for Biosensors.* Bioconjugate Chemistry, 2018. **29**(10): p. 3231-3239.

139. Van Dorst, B., et al., *Recent Advances in Recognition Elements of Food and Environmental Biosensors: a Review.* Biosensors and Bioelectronics, 2010. **26**(4): p. 1178-1194.

140. Bazin, I., et al., *New Biorecognition Molecules in Biosensors for the Detection of Toxins.* Biosensors and Bioelectronics, 2017. **87**: p. 285-298.

141. Schroeder, H.W. and L. Cavacini, *Structure and Function of Immunoglobulins.* Journal of Allergy and Clinical Immunology, 2010. **125**(2): p. S41-S52.

142. Janeway, C.A.J., et al., *Antigen Recognition by B-cell and T-cell Receptors*, in *Immunobiology: The immune system in health and disease*. 2001, Garland Science. p. 116-122.

143. Leenaars, M. and C.F.M. Hendriksen, *Critical Steps in the Production of Polyclonal and Monoclonal Antibodies Evaluation and Recommendations.* Ilar Journal, 2005. **46**(3): p. 269-279.

144. Lipman, N.S., et al., *Monoclonal Versus Polyclonal Antibodies: Distinguishing Characteristics, Applications, and Information Resources.* Ilar Journal, 2005. **46**(3): p. 258-268.

145. Zhu, L.P., et al., *Electrochemiluminescence Immunosensor Based on Au Nanocluster and Hybridization Chain Reaction Signal Amplification for Ultrasensitive Detection of Cardiac Troponin I.* Acs Sensors, 2019. **4**(10): p. 2778-2785.

146. Ye, J., et al., *Dual-Wavelength Ratiometric Electrochemiluminescence Immunosensor for Cardiac Troponin I Detection.* Analytical Chemistry, 2019. **91**(2): p. 1524-1531.

147. Shu, J., Z. Han, and H. Cui, *Highly Chemiluminescent TiO2/tetra(4-carboxyphenyl)porphyrin/N-(4-aminobutyl)-N-ethylisoluminol Nanoluminophores for Detection of Heart Disease Biomarker Copeptin based on Chemiluminescence Resonance Energy Transfer.* Analytical and Bioanalytical Chemistry, 2019. **411**(18): p. 4175-4183.

148. Zhang, W., et al., *Development of a Quantitative Detection Card for Heart-Type Fatty Acid-Binding Protein Based on Background Fluorescence Quenching Immune Chromatography.* Journal of Medical Biochemistry, 2019. **38**(2): p. 172-180.

149. Byzova, N.A., et al., *A Triple Immunochromatographic Test for Simultaneous Determination of Cardiac Troponin I, Fatty Acid Binding Protein, and C-reactive Protein Biomarkers.* Microchimica Acta, 2017. **184**(2): p. 463-471.

150. Saha, B., T.H. Evers, and M.W.J. Prins, *How Antibody Surface Coverage on Nanoparticles Determines the Activity and Kinetics of Antigen Capturing for Biosensing.* Analytical Chemistry, 2014. **86**(16): p. 8158-8166.

151. Balamurugan, S., et al., *Surface Immobilization Methods for Aptamer Diagnostic Applications.* Analytical and Bioanalytical Chemistry, 2008. **390**(4): p. 1009-1021.

152. Song, K.-M., S. Lee, and C. Ban, *Aptamers and Their Biological Applications.* Sensors, 2012. **12**(1): p. 612-631.

153. Chen, X., et al., *Sensitive Electrochemical Aptamer Biosensor for Dynamic Cell Surface N-Glycan Evaluation Featuring Multivalent Recognition and Signal Amplification on a Dendrimer–Graphene Electrode Interface.* Analytical Chemistry, 2014. **86**(9): p. 4278-4286.

154. Jin, C., et al., *Cancer Biomarker Discovery Using DNA Aptamers.* Analyst, 2016. **141**(2): p. 461-466.

155. Iliuk, A.B., L. Hu, and W.A. Tao, *Aptamer in Bioanalytical Applications.* Analytical Chemistry, 2011. **83**(12): p. 4440-4452.

156. Jo, H., et al., *Electrochemical Aptasensor of Cardiac Troponin I for the Early Diagnosis of Acute Myocardial Infarction.* Analytical Chemistry, 2015. **87**(19): p. 9869-9875.

157. Jo, H., et al., *Highly Sensitive Amperometric Detection of Cardiac Troponin I Using Sandwich Aptamers and Screen-Printed Carbon Electrodes.* Talanta, 2017. **165**: p. 442-448.

158. Kakoti, A. and P. Goswami, *Multifaceted Analyses of the Interactions Between Human Heart Type Fatty Acid Binding Protein and Its Specific Aptamers.* Biochimica Et Biophysica Acta-General Subjects, 2017. **1861**(1): p. 3289-3299.

159. Zhang, Y.L., P. Zuo, and B.C. Ye, *A Low-cost and Simple Paper-based Microfluidic Device for Simultaneous Multiplex Determination of Different Types of Chemical Contaminants in Food.* Biosensors and Bioelectronics, 2015. **68**: p. 14-19.

160. Yetisen, A.K., M.S. Akram, and C.R. Lowe, *Paper-based Microfluidic Point-of-care Diagnostic Devices.* Lab on a Chip, 2013. **13**(12): p. 2210-2251.

161. Li, X., D.R. Ballerini, and W. Shen, *A Perspective on Paper-based Microfluidics: Current Status and Future Trends.* Biomicrofluidics, 2012. **6**(1): p. 11301.

162. Ivanov, A.V., et al., *Nucleic Acid Lateral Flow Assay With Recombinase Polymerase Amplification: Solutions for Highly Sensitive Detection of RNA Virus.* Talanta, 2020. **210**: p. 120616.

163. Ding, Y., et al., *A Dual Signal Immunochromatographic Strip for the Detection of Imidaclothiz Using a Recombinant Fluorescent-peptide Tracer and Gold Nanoparticles.* Sensors and Actuators B-Chemical, 2019. **297**: p. 126714.

164. Russo, L., et al., *Detection of Resistance Protein A (MxA) in Paper-based Immunoassays With Surface Enhanced Raman Spectroscopy With AuAg Nanoshells.* Nanoscale, 2019. **11**(22): p. 10819-10827.

165. Nguyen, V.T., et al., *Recent Advances in High-sensitivity Detection Methods for Paper-based Lateral-flow Assay.* Biosensors and Bioelectronics, 2020. **152**: p. 112015.

166. Altundemir, S., A.K. Uguz, and K. Ulgen, *A Review on Wax Printed Microfluidic Paper-based Devices for International Health.* Biomicrofluidics, 2017. **11**(4): p. 041501.

167. Yang, D., et al., *Polyelectrolyte-Coated Gold Magnetic Nanoparticles for Immunoassay Development: Toward Point of Care Diagnostics for Syphilis Screening.* Analytical Chemistry, 2013. **85**(14): p. 6688-6695.

168. Gong, Y., et al., *A Portable and Universal Upconversion Nanoparticle-Based Lateral Flow Assay Platform for Point-of-Care Testing.* Talanta, 2019. **201**: p. 126-133.

169. Mu, X., et al., *Multiplex Microfluidic Paper-based Immunoassay for the Diagnosis of Hepatitis C Virus Infection.* Analytical Chemistry, 2014. **86**(11): p. 5338-5344.

170. Ilacas, G.C., et al., *Paper-Based Microfluidic Devices for Glucose Assays Employing a Metal-Organic Framework (MOF).* Analytica Chimica Acta, 2019. **1055**: p. 74-80.

171. Rong, Z., et al., *Smartphone-Based Fluorescent Lateral Flow Immunoassay Platform for Highly Sensitive Point-of-Care Detection of Zika Virus Nonstructural Protein 1.* Analytica Chimica Acta, 2019. **1055**: p. 140-147.

172. Safenkova, I.V., et al., *Alarm Lateral Flow Immunoassay for Detection of the Total Infection Caused by the Five Viruses.* Talanta, 2019. **195**: p. 739-744.

173. Xiao, M., et al., *Ultrasensitive Detection of Avian Influenza A (H7N9) Virus using Surface-Enhanced Raman Scattering-Based Lateral Flow Immunoassay Strips.* Analytica Chimica Acta, 2019. **1053**: p. 139-147.

174. Ji, T.X., et al., *Point of Care Upconversion Nanoparticles-Based Lateral Flow Assay Quantifying Myoglobin in Clinical Human Blood Samples.* Sensors and Actuators B-Chemical, 2019. **282**: p. 309-316.

175. Wu, Z., et al., *Rapid Detection of Beta-Conglutin with a Novel Lateral Flow Aptasensor Assisted by Immunomagnetic Enrichment and Enzyme Signal Amplification.* Food Chemistry, 2018. **269**: p. 375-379.

176. Liu, L.Y., D.T. Yang, and G.Z. Liu, *Signal Amplification Strategies for Paper-Based Analytical Devices.* Biosensors and Bioelectronics, 2019. **136**: p. 60-75.

177. Martinez, A.W., et al., *Patterned Paper as a Platform for Inexpensive, Low-Volume, Portable Bioassays.* Angewandte Chemie-International Edition, 2007. **46**(8): p. 1318-1320.

178. Cate, D.M., et al., *Recent Developments in Paper-Based Microfluidic Devices.* Analytical Chemistry, 2015. **87**(1): p. 19-41.

179. dos Santos, G.P., C.C. Correa, and L.T. Kubota, *A Simple, Sensitive and Reduced Cost Paper-Based Device with Low Quantity of Chemicals for the Early Diagnosis of Plasmodium Falciparum Malaria using an Enzyme-Based Colorimetric Assay.* Sensors and Actuators B-Chemical, 2018. **255**: p. 2113-2120.

180. Ota, R., et al., *Quantitative Evaluation of Analyte Transport on Microfluidic Paper-Based Analytical Devices (mu PADs).* Analyst, 2018. **143**(3): p. 643-653.

181. Fu, E., et al., *Two-Dimensional Paper Network Format That Enables Simple Multistep Assays for Use in Low-Resource Settings in the Context of Malaria Antigen Detection.* Analytical Chemistry, 2012. **84**(10): p. 4574-4579.

182. Toley, B.J., et al., *Tunable-Delay Shunts for Paper Microfluidic Devices.* Analytical Chemistry, 2013. **85**(23): p. 11545-11552.

183. Ramachandran, S., et al., *Long-Term Dry Storage of an Enzyme-Based Reagent System for ELISA in Point-of-Care Devices.* Analyst, 2014. **139**(6): p. 1456-1462.

184. Li, F., et al., *High-Resolution Temporally Resolved Chemiluminescence based on Double-Layered 3D Microfluidic Paper-Based Device for Multiplexed Analysis.* Biosensors and Bioelectronics, 2019. **141**: p. 111472.

185. Preechakasedkit, P., et al., *Development of an Automated Wax-Printed Paper-Based Lateral Flow Device for Alpha-Fetoprotein Enzyme-Linked Immunosorbent Assay.* Biosensors and Bioelectronics, 2018. **102**: p. 27-32.

186. Rivas, L., et al., *Improving Sensitivity of Gold Nanoparticle-Based Lateral Flow Assays by Using Wax-Printed Pillars as Delay Barriers of Microfluidics.* Lab on a Chip, 2014. **14**(22): p. 4406-4414.

187. Jang, I. and S. Song, *Facile and Precise Flow Control for a Paper-Based Microfluidic Device through Varying Paper Permeability.* Lab on a Chip, 2015. **15**(16): p. 3405-3412.

188. Choi, J.R., et al., *Lateral Flow Assay Based on Paper-Hydrogel Hybrid Material for Sensitive Point-of-Care Detection of Dengue Virus.* Advanced Healthcare Materials, 2017. **6**(1): p. 1600920.

189. Chu, W.R., et al., *Paper-Based Chemiluminescence Immunodevice with Temporal Controls of Reagent Transport Technique.* Sensors and Actuators B-Chemical, 2017. **250**: p. 324-332.

190. Lutz, B., et al., *Dissolvable Fluidic Time Delays for Programming Multi-Step Assays in Instrument-Free Paper Diagnostics.* Lab on a Chip, 2013. **13**(14): p. 2840-2847.

191. Fu, E., et al., *Controlled Reagent Transport in Disposable 2D Paper Networks.* Lab on a Chip, 2010. **10**(7): p. 918-920.

192. Songok, J. and M. Toivakka, *Controlling Capillary-Driven Surface Flow on a Paper-based Microfluidic Channel.* Microfluidics and Nanofluidics, 2016. **20**(4): p. 63.

193. Giokas, D.L., G.Z. Tsogas, and A.G. Vlessidis, *Programming Fluid Transport in Paper-Based Microfluidic Devices Using Razor-Crafted Open Channels.* Analytical Chemistry, 2014. **86**(13): p. 6202-6207.

194. da Silva, E.T.S.G., et al., *Triboelectric Effect as a New Strategy for Sealing and Controlling the Flow in Paper-Based Devices.* Lab on a Chip, 2015. **15**(7): p. 1651-1655.

195. Verma, M.S., et al., *Sliding-strip Microfluidic Device Enables ELISA on Paper.* Biosensors and Bioelectronics, 2018. **99**: p. 77-84.

196. Sun, X.G., et al., *Improved Assessment of Accuracy and Performance Using a Rotational Paper-based Device for Multiplexed Detection of Heavy Metals.* Talanta, 2018. **178**: p. 426-431.

197. Han, J.L., et al., *Simple Way To Fabricate Novel Paper-Based Valves Using Plastic Comb Binding Spines.* Acs Sensors, 2018. **3**(9): p. 1789-1794.

198. Chen, C., et al., *Novel Wax Valves To Improve Distance-Based Analyte Detection in Paper Microfluidics.* Analytical Chemistry, 2019. **91**(8): p. 5169-5175.

199. Reboud, J., et al., *Paper-based Microfluidics for DNA Diagnostics of Malaria in Low Resource Underserved Rural Communities.* Proceedings of the National Academy of Sciences, 2019. **116**(11): p. 4834-4842.

200. Alba-Patino, A., S.M. Russell, and R. de la Rica, *Origami-enabled Signal Amplification for Paper-based Colorimetric Biosensors.* Sensors and Actuators B-Chemical, 2018. **273**: p. 951-954.

201. Han, K.N., J.S. Choi, and J. Kwon, *Three-dimensional Paper-based Slip Device for One-step Point-of-care Testing.* Scientific Reports, 2016. **6**: p. 25710.

202. Sun, X., et al., *Rotational Paper-based Electrochemiluminescence Immunodevices for Sensitive and Multiplexed Detection of Cancer Biomarkers.* Analytica Chimica Acta, 2018. **1007**: p. 33-39.

203. Sun, H., et al., *A Suspending-droplet Mode Paper-based Microfluidic Platform for Low-cost, Rapid, and Convenient Detection of Lead(II) Ions in Liquid Solution.* Biosensors and Bioelectronics, 2018. **99**: p. 361-367.

204. Martinez, A.W., et al., *Programmable Diagnostic Devices Made From Paper and Tape.* Lab on a Chip, 2010. **10**(19): p. 2499-2504.

205. Li, X., P. Zwanenburg, and X. Liu, *Magnetic Timing Valves for Fluid Control in Paper-Based Microfluidics.* Lab on a Chip, 2013. **13**(13): p. 2609-2614.

206. Toley, B.J., et al., *A Versatile Valving Toolkit for Automating Fluidic Operations in Paper Microfluidic Devices.* Lab on a Chip, 2015. **15**(6): p. 1432-1444.

207. Rosenfeld, T. and M. Bercovici, *Dynamic Control of Capillary Flow in Porous Media by Electroosmotic Pumping.* Lab on a Chip, 2019. **19**(2): p. 328-334.

208. Guo, Z.H., et al., *Self-Powered Electrowetting Valve for Instantaneous and Simultaneous Actuation of Paper-Based Microfluidic Assays.* Advanced Functional Materials, 2019. **29**(15): p. 1808974.

209. Ainla, A., et al., *Electrical Textile Valves for Paper Microfluidics.* Advanced Materials, 2017. **29**(38): p. 1702894.

210. Lafleur, L.K., et al., *A Rapid, Instrument-free, Sample-to-result Nucleic Acid Amplification Test.* Lab on a Chip, 2016. **16**(19): p. 3777-3787.

211. Wang, J., et al., *A Paper-based Device With an Adjustable Time Controller for the Rapid Determination of Tumor Biomarkers.* Sensors and Actuators B-Chemical, 2018. **254**: p. 855-862.

212. Cai, L., et al., *Defining Microchannels and Valves on a Hydrophobic Paper by Low-cost Inkjet Printing of Aqueous or Weak Organic Solutions.* Biomicrofluidics, 2015. **9**(4): p. 046503.

213. Gerbers, R., et al., *A New Paper-Based Platform Technology for Point-of-Care Diagnostics.* Lab on a Chip, 2014. **14**(20): p. 4042-4049.

214. Chen, H., et al., *A Fluidic Diode, Valves, and a Sequential-Loading Circuit Fabricated on Layered Paper.* Lab on a Chip, 2012. **12**(16): p. 2909-2913.

215. Jahanshahi-Anbuhi, S., et al., *Paper-Based Microfluidics with an Erodible Polymeric Bridge Giving Controlled Release and Timed Flow Shutoff.* Lab on a Chip, 2014. **14**(1): p. 229-236.

216. Noh, N. and S.T. Phillips, *Metering the Capillary-Driven Flow of Fluids in Paper-Based Microfluidic Devices.* Analytical Chemistry, 2010. **82**(10): p. 4181-4187.

217. Shin, J.H., et al., *Programmed Sample Delivery on a Pressurized Paper.* Biomicrofluidics, 2014. **8**(5): p. 054121.

218. Kong, T., et al., *A Fast, Reconfigurable Flow Switch for Paper Microfluidics Based on Selective Wetting of Folded Paper Actuator Strips.* Lab on a Chip, 2017. **17**(21): p. 3621-3633.

219. Sharma, A., et al., *Gold Nanoparticle Conjugated Magnetic Beads for Extraction and Nucleation Based Signal Amplification in Lateral Flow Assaying.* Sensors and Actuators B-Chemical, 2020. **312**: p. 127959.

220. Ouyang, W. and J. Han, *Universal Amplification-free Molecular Diagnostics by Billion-fold Hierarchical Nanofluidic Concentration.* Proceedings of the National Academy of Sciences of the United States of America, 2019. **116**(33): p. 16240-16249.

221. Sinha, A., et al., *An Integrated Microfluidic System With Field-effect-transistor Sensor Arrays for Detecting Multiple Cardiovascular Biomarkers From Clinical Samples.* Biosensors and Bioelectronics, 2019. **129**: p. 155-163.

222. Fathil, M.F.M., et al., *Diagnostics on Acute Myocardial Infarction: Cardiac Troponin Biomarkers.* Biosensors and Bioelectronics, 2015. **70**: p. 209-220.

223. Benjamin, *Heart Disease and Stroke Statistics-2018 Update: A Report From the American Heart Association (vol 137, pg e67, 2018).* Circulation, 2018. **137**(12): p. E493-E493.

224. Mueller, C., R. Twerenbold, and T. Reichlin, *Early Diagnosis of Myocardial Infarction with Sensitive Cardiac Troponin Assays.* Clinical Chemistry, 2019. **65**(3): p. 490-491.

225. Aldous, S.J., *Cardiac Biomarkers in Acute Myocardial Infarction.* International Journal of Cardiology, 2013. **164**(3): p. 282-294.

226. Eggers, K.M., et al., *Value of Cardiac Troponin I Cutoff Concentrations below the 99th Percentile for Clinical Decision-Making.* Clinical Chemistry, 2009. **55**(1): p. 85-92.

227. Liang, C., et al., *Smartphone-app Based Point-of-care Testing for Myocardial Infarction Biomarker cTnI Using an Autonomous Capillary Microfluidic Chip With Self-aligned on-chip Focusing (SOF) Lenses.* Lab on a Chip, 2019. **19**(10): p. 1797-1807.

228. McDonnell, B., et al., *Cardiac Biomarkers and the Case for Point-of-care Testing.* Clinical Biochemistry, 2009. **42**(7-8): p. 549-561.

229. Liu, J.J., et al., *Point-of-Care Testing Based on Smartphone: The Current State-of-the-Art (2017-2018).* Biosensors and Bioelectronics, 2019. **132**: p. 17-37.

230. Sardi, A.R., et al., *Point-of-Care Testing of Troponin Levels Compared With Automated Laboratory Evaluation: A Reliability Study.* Critical Care Nursing Quarterly, 2016. **39**(4): p. 345-351.

231. Azzazy, H.M.E. and R.H. Christenson, *Cardiac Markers of Acute Coronary Syndromes: Is There a Case for Point-of-care Testing?* Clinical Biochemistry, 2002. **35**(1): p. 13-27.

232. Amsterdam, E.A., et al., *2014 AHA/ACC Guideline for the Management of Patients With Non-ST-Elevation Acute Coronary Syndromes A Report of the American College of Cardiology/American Heart Association Task Force on Practice Guidelines.* Journal of the American College of Cardiology, 2014. **64**(24): p. E139-E228.

233. Lambert, L., et al., *Association Between Timeliness of Reperfusion Therapy and Clinical Outcomes in ST-Elevation Myocardial Infarction.* Jama-Journal of the American Medical Association, 2010. **303**(21): p. 2148-2155.

234. O'Gara, P.T., et al., *2013 ACCF/AHA Guideline for the Management of ST-Elevation Myocardial Infarction A Report of the American College of Cardiology Foundation/American Heart Association Task Force on Practice Guidelines.* Journal of the American College of Cardiology, 2013. **61**(4): p. E78-E140.

235. Cao, J.T., et al., *Reduced Graphene Oxide-gold Nanoparticles-catalase-based Dual Signal Amplification Strategy in a Spatial-resolved Ratiometric Electrochemiluminescence Immunoassay.* Analyst, 2020. **145**(1): p. 91-96.

236. Natarajan, S., et al., *A Paper Microfluidics-based Fluorescent Lateral Flow Immunoassay for Point-of-care Diagnostics of Non-communicable Diseases.* Analyst, 2019. **144**(21): p. 6291-6303.

237. Garza, J.T. and G.L. Cote, *Collection Method of SERS Active Nanoparticles for Sensitive and Precise Measurements.* Analytical Chemistry, 2017. **89**(24): p. 13120-13127.

238. Fu, X.L., et al., *A graphene oxide/gold nanoparticle-based amplification method for SERS immunoassay of cardiac troponin I.* Analyst, 2019. **144**(5): p. 1582-1589.

239. Lee, S.R., et al., *Simultaneous Detection of SERS and Fluorescence Using a Single Excitation for Microbead-Based Analysis.* Journal of Biomedical Nanotechnology, 2013. **9**(7): p. 1241-1244.

240. Zhang, D., et al., *Quantitative and ultrasensitive detection of multiplex cardiac biomarkers in lateral flow assay with core-shell SERS nanotags.* Biosensors & Bioelectronics, 2018. **106**: p. 204-211.

241. Bai, T.T., et al., *Functionalized Au@Ag-Au nanoparticles as an optical and SERS dual probe for lateral flow sensing.* Analytical and Bioanalytical Chemistry, 2018. **410**(9): p. 2291-2303.

242. Lou, D.D., et al., *A Signal Amplifying Fluorescent Nanoprobe and Lateral Flow Assay for Ultrasensitive Detection of Cardiac Biomarker Troponin I.* Analytical Methods, 2019. **11**(28): p. 3506-3513.

243. Vasantham, S., et al., *Paper Based Point of Care Immunosensor for the Impedimetric Detection of Cardiac Troponin I Biomarker.* Biomedical Microdevices, 2019. **22**(1): p. 6.

244. Negahdary, M. and H. Heli, *An Electrochemical Troponin I Peptisensor Using a Triangular Icicle-like Gold Nanostructure.* Biochemical Engineering Journal, 2019. **151**: p. 107326.

245. Gao, C.M., et al., *Paper Based Modification-free Photoelectrochemical Sensing Platform With Single-crystalline Aloe Like Tio2 as Electron Transporting Material for Ctni Detection.* Biosensors and Bioelectronics, 2019. **131**: p. 17-23.

246. Luo, Z.B., et al., *DNA Nanotetrahedron Linked Dual-aptamer Based Voltammetric Aptasensor for Cardiac Troponin I Using a Magnetic Metal-organic Framework as a Label.* Microchimica Acta, 2019. **186**(6): p. 374.

247. Gong, M.M., et al., *Nanoporous Membranes Enable Concentration and Transport in Fully Wet Paper-Based Assays.* Analytical Chemistry, 2014. **86**(16): p. 8090-8097.

248. Zhu, G.Y., et al., *Paper-based immunosensors: Current trends in the types and applied detection techniques.* Trac-Trends in Analytical Chemistry, 2019. **111**: p. 100-117.

249. Thiviyanathan, V. and D.G. Gorenstein, *Aptamers and the Next Generation of Diagnostic Reagents.* Proteomics Clinical Applications, 2012. **6**(11-12): p. 563-573.

250. Song, D., et al., *SERS Based Aptasensor for Ochratoxin A by Combining Fe3O4@Au Magnetic Nanoparticles and Au-DTNB@Ag Nanoprobes with Multiple Signal Enhancement.* Microchimica Acta, 2018. **185**(10): p. 491.

251. Nie, S.M. and S.R. Emery, *Probing Single Molecules and Single Nanoparticles by Surface-enhanced Raman Scattering.* Science, 1997. **275**(5303): p. 1102-1106.

252. Bastus, N.G., J. Comenge, and V. Puntes, *Kinetically Controlled Seeded Growth Synthesis of Citrate-Stabilized Gold Nanoparticles of up to 200 nm: Size Focusing versus Ostwald Ripening.* Langmuir, 2011. **27**(17): p. 11098-11105.

253. Maiti, K.K., et al., *Development of Biocompatible SERS Nanotag With Increased Stability by Chemisorption of Reporter Molecule for in Vivo Cancer Detection.* Biosensors and Bioelectronics, 2010. **26**(2): p. 398-403.

254. Harmsen, S., et al., *Cancer imaging using surface-enhanced resonance Raman scattering nanoparticles.* Nature Protocols, 2017. **12**(7): p. 1400-1414.

255. Li, M., et al., *Shape-dependent Surface-enhanced Raman Scattering in gold-Ramanprobe-silica Sandwiched Nanoparticles for Biocompatible Applications.* Nanotechnology, 2012. **23**(11): p. 115501.

256. Goff, D.C., et al., *2013 ACC/AHA Guideline on the Assessment of Cardiovascular Risk A Report of the American College of Cardiology/American Heart Association Task Force on Practice Guidelines.* Circulation, 2014. **129**(25): p. S49-S73.

257. Mythili, S. and N. Malathi, *Diagnostic Markers of Acute Myocardial Infarction.* Biomedical Reports, 2015. **3**(6): p. 743-748.

258. Frohnmeyer, E., et al., *Aptamer Lateral Flow Assays for Rapid and Sensitive Detection of Cholera Toxin.* Analyst, 2019. **144**(5): p. 1840-1849.

259. Sharma, A., et al., *Magnetic Field Assisted Preconcentration of Biomolecules for Lateral Flow Assaying.* Sensors and Actuators B-Chemical, 2019. **285**: p. 431-437.

260. Li, K.J., et al., *Simultaneous Detection of Gastric Cancer Screening Biomarkers Plasma Pepsinogen I/II using Fluorescent Immunochromatographic Strip Coupled with a Miniature Analytical Device.* Sensors and Actuators B-Chemical, 2019. **286**: p. 272-281.

261. Kim, T.H., et al., *Solenoid Driven Pressure Valve System: Toward Versatile Fluidic Control in Paper Microfluidics.* Analytical Chemistry, 2018. **90**(4): p. 2534-2541.

262. Ouellette, N.T., H.T. Xu, and E. Bodenschatz, *A Quantitative Study of Three-Dimensional Lagrangian Particle Tracking Algorithms.* Experiments in Fluids, 2006. **40**(2): p. 301-313.

263. Kelley, D.H. and N.T. Ouellette, *Using Particle Tracking to Measure Flow Instabilities in an Undergraduate Laboratory Experiment.* American Journal of Physics, 2011. **79**(3): p. 267-273.

264. Su, S.X., et al., *Adsorption and Covalent Coupling of ATP-Binding DNA Aptamers onto Cellulose.* Langmuir, 2007. **23**(3): p. 1300-1302.

265. Laos, A.K., et al. *Crystallization of the Supersaturated Sucrose Solutions in the Presence of Fructose, Glucose and Corn Syrup*. in *Innovations in Food Technology, Proceedings of European Congress of Chemical Engineering*

(ECCE-6), Copenhagen, Denmark, Sept 16-20, 2007. 2007. Copenhagen, Denmark.

266. Feng, L.N., et al., *Ultrasensitive Multianalyte Electrochemical Immunoassay Based on Metal Ion Functionalized Titanium Phosphate Nanospheres.* Analytical Chemistry, 2012. **84**(18): p. 7810-7815.

267. Chen, R.P., et al., *Vertical Flow Assays Based on Core-shell SERS Nanotags for Multiplex Prostate Cancer Biomarker Detection.* Analyst, 2019. **144**(13): p. 4051-4059.

268. Li, Y.X., et al., *Metal-Organic Frameworks for Preserving the Functionality of Plasmonic Nanosensors.* Acs Applied Materials & Interfaces, 2021. **13**(4): p. 5564-5573.

269. Njoki, P.N., et al., *Size Correlation of Optical and Spectroscopic Properties for Gold Nanoparticles.* The Journal of Physical Chemistry C, 2007. **111**(40): p. 14664-14669.

270. Apple, F.S., et al., *Point-of-care i-STAT Cardiac Troponin I for Assessment of Patients With Symptoms Suggestive of Acute Coronary Syndrome.* Clinical Chemistry, 2006. **52**(2): p. 322-325.

271. Kemper, D.W., et al., *Analytical Evaluation of a New Point of Care System for Measuring Cardiac Troponin I.* Clinical Biochemistry, 2017. **50**(4-5): p. 174-180.

272. Stober, W., A. Fink, and E. Bohn, *Controlled Growth of Monodisperse Silica Spheres in Micron Size Range.* Journal of Colloid and Interface Science, 1968. **26**(1): p. 62-69.

273. Seager, R.J., et al., *Solid Dissolution in a Fluid Solvent Is Characterized by the Interplay of Surface Area-dependent Diffusion and Physical Fragmentation.* Scientific Reports, 2018. **8**: p. 7711.

274. Schechinger, M., et al., *A SERS Approach for Rapid Detection of MicroRNA-17 in the Picomolar Range.* Analyst, 2019. **144**(13): p. 4033-4044.

275. Wang, Z., et al., *Dual-mode Probe Based on Mesoporous Silica Coated Gold Nanorods for Targeting Cancer Cells.* Biosensors and Bioelectronics, 2011. **26**(6): p. 2883-2889.

276. Shrestha, Y.K. and F. Yan, *Determination of Critical Micelle Concentration of Cationic Surfactants by Surface-enhanced Raman Scattering.* Rsc Advances, 2014. **4**(70): p. 37274-37277.

277. Roth, P.G., R.S. Venkatachalam, and F.J. Boerio, *Surface-Enhanced Raman-Scattering from Para-Nitrobenzoic Acid.* Journal of Chemical Physics, 1986. **85**(2): p. 1150-1155.

278. Alula, M.T., et al., *Preparation of Silver Nanoparticles Coated ZnO/Fe3O4 Composites Using Chemical Reduction Method for Sensitive Detection of Uric Acid via Surface-enhanced Raman Spectroscopy.* Analytica Chimica Acta, 2019. **1073**: p. 62-71.

279. Schutz, M., et al., *Synthesis of Glass-coated SERS Nanoparticle Probes via SAMs with Terminal SiO2 Precursors.* Small, 2010. **6**(6): p. 733-737.

280. Lin, C.C. and C.W. Chang, *AuNPs@mesoSiO2 Composites for SERS Detection of DTNB Molecule.* Biosensors and Bioelectronics, 2014. **51**: p. 297-303.

281. Philippidis, A., Z.E. Papliaka, and D. Anglos, *Surface Enhanced Raman and 2D-Fluorescence Spectroscopy for the Investigation of Amino Acids and Egg Proteins.* Microchemical Journal, 2016. **126**: p. 230-236.

282. Lippert, T., F. Zimmermann, and A. Wokaun, *Surface-Analysis of Excimer-Laser-Treated Polyethylene-Terephthalate by Surface-Enhanced Raman-Scattering and X-Ray Photoelectron-Spectroscopy.* Applied Spectroscopy, 1993. **47**(11): p. 1931-1942.

283. Hu, J.W., et al., *Surface-enhanced Raman Spectroscopy Study on the Structure Changes of 4-mercaptopyridine Adsorbed on Silver Substrates and Silver Colloids.* Spectrochimica Acta Part a-Molecular and Biomolecular Spectroscopy, 2002. **58**(13): p. 2827-2834.

284. Zhang, Y.Y., et al., *Analyses of Enrofloxacin, Furazolidone and Malachite Green in Fish Products With Surface-enhanced Raman Spectroscopy.* Food Chemistry, 2012. **135**(2): p. 845-850.

285. Castro, J.L., et al., *Surface-enhanced Raman Scattering of 3-phenylpropionic Acid (Hydrocinnamic Acid).* Journal of Raman Spectroscopy, 2002. **33**(6): p. 455-459.

286. Wu, X.M., et al., *The Surface-enhanced Raman Spectra of Aflatoxins: Spectral Analysis, Density Functional Theory Calculation, Detection and Differentiation.* Analyst, 2012. **137**(18): p. 4226-4234.

287. Wu, S.Y., Y. Shen, and C.J. Jin, *Surface-enhanced Raman Scattering Induced by the Coupling of the Guided Mode With Localized Surface Plasmon Resonances.* Nanoscale, 2019. **11**(30): p. 14164-14173.

288. Ou, Y.M., et al., *Rapid Analysis of Multiple Sudan Dyes in Chili Flakes Using Surface-Enhanced Raman Spectroscopy Coupled with Au-Ag Core-Shell Nanospheres.* Food Analytical Methods, 2017. **10**(3): p. 565-574.

289. Preuss, M. and F. Bechstedt, *Vibrational Spectra of Ammonia, Benzene, and Benzene Adsorbed on Si (001) by First Principles Calculations With Periodic Boundary Conditions.* Physical Review B, 2006. **73**(15): p. 155413.

290. Jiang, L., et al., *Surface-enhanced Raman Scattering Spectra of Adsorbates on Cu2O Nanospheres: Charge-transfer and Electromagnetic Enhancement.* Nanoscale, 2013. **5**(7): p. 2784-2789.

291. Xu, S.P., et al., *Immunoassay Using Probe-labelling Immunogold Nanoparticles With Silver Staining Enhancement via Surface-enhanced Raman Scattering.* Analyst, 2004. **129**(1): p. 63-68.

292. Haruna, K., et al., *Hydroxylamine Reduced Silver Colloid for Naphthalene and Phenanthrene Detection Using Surface-enhanced Raman Spectroscopy.* Chemical Engineering Journal, 2016. **304**: p. 141-148.

293. Klein, R. *Bland-Altman and Correlation Plot* MATLAB Central File Exchange 2021 [cited 2021 October 6]; Available from: https://www.mathworks.com/matlabcentral/fileexchange/45049-bland-altman-and-correlation-plot.

294. Giavarina, D., *Understanding Bland Altman analysis.* Biochemia Medica, 2015. **25**(2): p. 141-151.

295. Bland, J.M. and D.G. Altman, *Statistical Methods for Assessing Agreement between Two Methods of Clinical Measurement.* Lancet, 1986. **1**(8476): p. 307-310.

APPENDIX A

SUPPORTING INFORMATION FOR APTAMER-BASED SURFACE ENHANCED RESONANCE RAMAN SCATTERING ASSAY ON A PAPER FLUIDIC PLATFORM FOR DETECTION OF CARDIAC TROPONIN I

To evaluate the distribution of the particles on a test line on the paper strip, the following process was implemented. The SERS intensity on the test line area was measured using the mapping function in the Thermo Scientific DXR Raman confocal microscope with a 780 nm laser. A 10 × 40 point array with a 100 μm step size was measured on the test line area. Each point was measured by exciting with a 24 mW laser using a 3 s exposure. All spectra were baseline corrected. By using the peak intensity at around 1617 cm^{-1}, the SERS intensity map could be drawn. Figure A1 shows the SERS intensity map of the test line on a paper strip after testing 0.03 ng/mL of cTnI. It could be observed that the SERS signal at some spots are stronger. To overcome this variation, our work used a portable Raman spectrometer that has a Raster mode, which can scan a larger area on the test line than a single spot Raman measurement system. The Raman spectrometer also had a spot size of around 2.5 mm in its Raster mode, and hence it covered the thickness of the test line. An averaged intensity at 3 different spots of the test line from the left side to the right side was also used. Because the strip had a width of 4 mm and the spectrometer had a spot size of around 2.5 mm, three measurements was enough to cover the whole test line area. The final SERRS signal of the test line on a strip was the average of the intensity from these spectra.

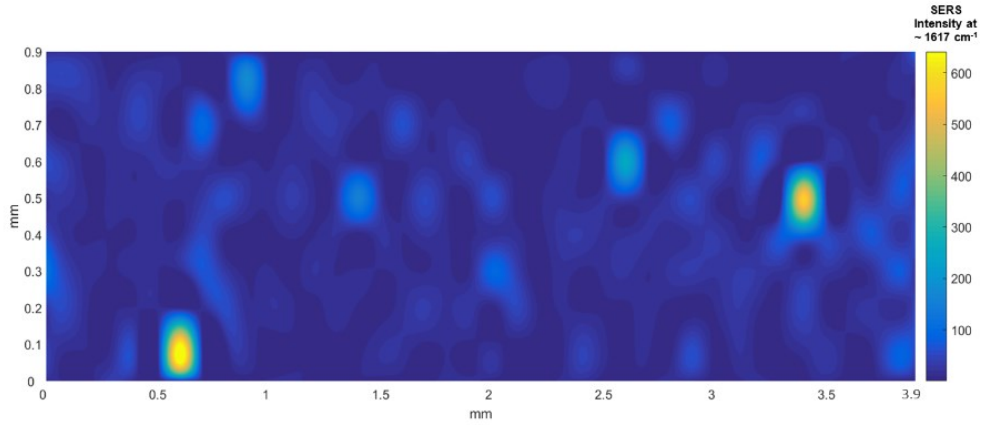

Figure A1 SERS intensity distribution at the test line when testing 0.03 ng/mL of cTnI.

Table A1. Comparison of the developed assay with previously reported assays for cTnI detection

No.	Transduction Mode	Portable Reader? (Y/N)	Recognition Element	Paper Based Platform? (Y/N)	Limit of Detection (ng/mL)	Detection Time (min)	Ref.
1	Electrochemilumine scence (ECL)	N	antibody	N	0.0001	120	[235]
2	Electrochemilumine scence (ECL)	N	antibody	N	0.0032	240	[83]
3	Fluorescence	N	antibody	Y	0.049	15	[242]
4	Electrochemistry	N	antibody	Y	0.05	1	[243]
5	Fluorescence	Y	antibody	Y	0.01	10	[236]
6	Electrochemistry	N	peptide	N	0.0009	50	[244]
7	Photoelectrochemic al	N	aptamer	Y	0.00000047	240	[245]
8	Electrochemistry	N	aptamer	N	0.0057	120	[246]
9	Electrochemistry	Y	antibody	N	0.02	<10	* [270]
10	-	Y	antibody	N	0.018	<10	* [271]
11	Surface Enhanced Raman Spectroscopy (SERS)	Y	aptamer	Y	0.016	40	This work

* Commercially available product

APPENDIX B

SUPPORTING INFORMATION FOR PAPER MICROFLUIDIC DEVICE WITH A HORIZONTAL MOTION VALVE AND A LOCALIZED DELAY FOR AUTOMATIC CONTROL OF A MULTISTEP ASSAY

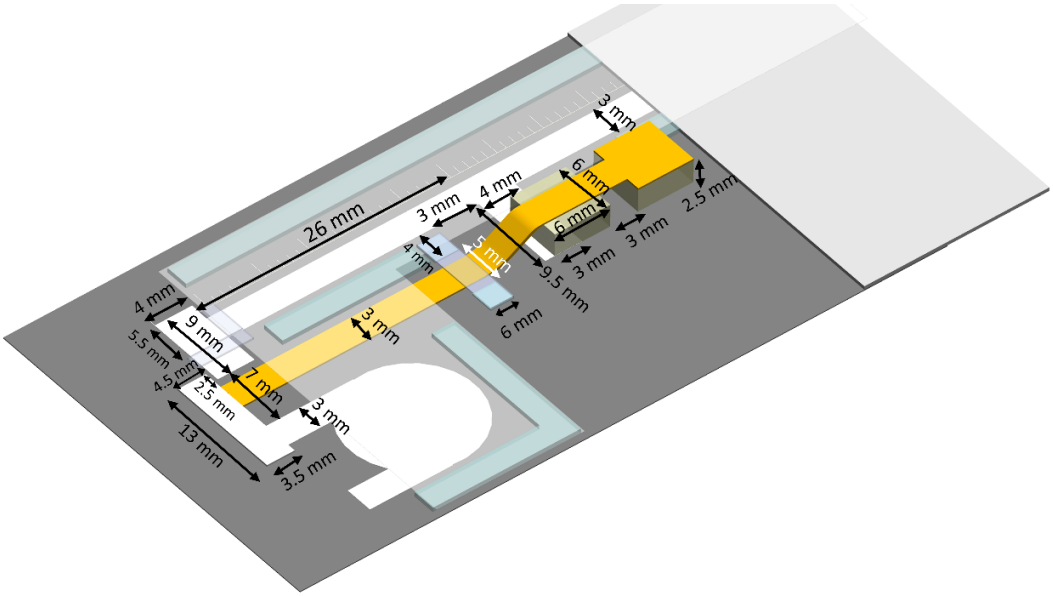

Figure B1. Dimensions and positions of components when making the µPAD with a horizontal motion mechanical valve.

Table B1. Amounts of saturated sucrose solution and fructose needed to make the sucrose solution and sucrose/fructose mixtures.

Solution	Volume of Saturated Sucrose Solution (mL)	Volume of DI water (mL)	Weight of Fructose (g)
0.2 g/mL sucrose	1	9	-
0.6 g/mL sucrose	3	7	-
1 g/mL sucrose	5	5	-
1.4 g/mL sucrose	7	3	-
1.8 g/mL sucrose	9	1	-
0.2 g/mL sucrose with 0.5 g/mL fructose	1	9	5
0.6 g/mL sucrose with 0.5 g/mL fructose	3	7	5
1 g/mL sucrose with 0.5 g/mL fructose	5	5	5
1.4 g/mL sucrose with 0.5 g/mL fructose	7	3	5
0.2 g/mL sucrose with 1.0 g/mL fructose	1	9	10
0.6 g/mL sucrose with 1.0 g/mL fructose	3	7	10
1 g/mL sucrose with 1.0 g/mL fructose	5	5	10
1.4 g/mL sucrose with 1.0 g/mL fructose	7	3	10
0.2 g/mL sucrose with 1.5 g/mL fructose	1	9	15
0.6 g/mL sucrose with 1.5 g/mL fructose	3	7	15
1 g/mL sucrose with 1.5 g/mL fructose	5	5	15
1.4 g/mL sucrose with 1.5 g/mL fructose	7	3	15
0.2 g/mL sucrose with 2.0 g/mL fructose	1	9	20
0.6 g/mL sucrose with 2.0 g/mL fructose	3	7	20
1 g/mL sucrose with 2.0 g/mL fructose	5	5	20
1.4 g/mL sucrose with 0.5 g/mL fructose	7	3	5
1.4 g/mL sucrose with 1 g/mL fructose	7	3	10
1.4 g/mL sucrose with 1.5 g/mL fructose	7	3	15
1.8 g/mL sucrose with 0.5 g/mL fructose	9	1	5
2.5 g/mL fructose	-	10	25

To form a test line and a control line in the μPAD, aptamer 1 and the control line DNA strand were immobilized on the hydrophilic channel of cellulose paper using a modified process based on the Schiff base and reduction method [264]. The reaction process is shown in Figure B2. The cellulose paper was first reacted with $NaIO_4$ to oxidize

hydroxyl groups and generate aldehyde groups. The aldehyde groups were then reacted with amine-functionalized aptamer 1 to form a Schiff base, which was then reduced by $NaCNBH_3$ to generate a stable covalent bond between the aptamer and cellulose paper.

Specifically, a wax patterned paper was soaked in 60 mL of 0.03 M NaIO4 and allowed to react overnight at room temperature in the dark. The paper was then washed with water and dried in a desiccator. Amine-functionalized aptamer 1 in PBS (pH 7.4) was heated to 85 °C for 5 min and then cooled to room temperature to fold into its tertiary structure. Aptamer 1 (300 μM) was then dispensed on the paper using a dispenser (ClaremontBio Solutions, USA) with a 6 V power supply and a pump with a flow rate of 0.15 mL/min. A similar process, with a flow rate of 0.15 mL/min, was used to dispense the control line DNA strand. The paper was then immersed in 0.1 M $NaBH_3CN$ in PBS for 10 hours in the dark. The paper was washed three times with PBS and water, and then dried at room temperature.

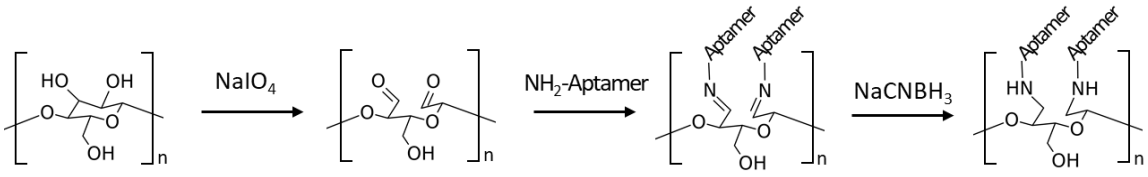

Figure B2. Reaction process to immobilize aptamer on cellulose paper based on a Schiff base plus reduction method.

To create aptamer 2-functionalized SERS active particles, 60 nm gold nanoparticles (AuNPs) were synthesized using a seed-mediated synthesis method [252]. Briefly, 75 mL of 2.2 mM sodium citrate in water was heated under vigorous stirring. After the solution boiled, 0.5 mL of 25 mM $HAuCl_4$ was injected, and the mixture was stirred for 30 min. The temperature was then adjusted to 90 °C, followed by injection of 0.5 mL of 25 mM $HAuCl_4$ and the mixture stirred for 30 min. This process was repeated one time before diluting the particle solution by extracting 27.5 mL of solution and adding 26.5 mL of water and 1 mL of 60 mM sodium citrate. While keeping the temperature at 90 °C, 0.5 mL of 25mM $HAuCl_4$ was injected, and the mixture was stirred for 30 min. The above processes were repeated until the size of the particle reached 60 nm. The final AuNP solution was cooled down at room temperature.

A Raman reporter molecule (Malachite green isothiocyanate, MGITC) was modified on the AuNPs to provide a SERS signal. The AuNPs were then encapsulated in a silica shell using a modified method based on Stöber′s method [272]. Briefly, 50 µL of 20 µM MGITC solution was mixed with 10 mL AuNPs in a glass vial, and the mixture was kept shaking for 15 min. 12.4 µL of 1 mM SH-PEG-COOH was then added, and the mixture was kept shaking for 15 min. The mixture was then centrifuged (1.5k rcf, 20 min) and resuspended in 1 mL of 2-propanol. 3.6 mL of water and 19.7 µL of 0.1 mM (3-mercaptopropyl)trimethoxysilane (MPTMS) solution were added in the particle solution, and the mixture was kept shaking for 15 min. 9 mL of 2-propanol and 250 µL of ammonium hydroxide were then added, followed by adding 100 µL of TEOS solution (1% in 2-propanol) and another 100 µL after 30 min while stirring in rotator. The mixture was

then kept rotating overnight. The resulting solution was centrifuged (1k rcf, 20 min) and washed three times with ethanol. Finally, the synthesized silica shell particle was resuspended in 5 mL of ethanol.

To immobilize aptamer 2 on the silica shell particle, 0.3 mL of water and 0.2 mL of (3-triethoxysilyl)propylsuccinic anhydride (TEPSA) (0.2 M in ethanol) were added in 1 mL silica shell particles. The particle solution was kept shaking overnight and then was washed and resuspended in 1 mL of phosphate buffer (PH 7.4). 75 μL of 50 mM Sulfo-NHS and 20 mM EDC and 80 μL of 0.01 mM amine-functionalized aptamer 2 were then added to the particle solution, and the mixture was left shaking for 1 hour. The mixture was then sonicated and mixed with 75 μL of 0.2 M ethanolamine solution (PH 8.6), followed by shaking for 1 hour. Finally, the aptamer-functionalized silica shell particles were sonicated, washed and resuspended in 0.2 mL of phosphate buffer (PH 7.4).

A glass fiber pad was soaked in a buffer with 1% bovine serum albumin, 0.5% Tween 20 and 5% sucrose and then dried at 45 °C for 1 hour. The synthesized aptamer-functionalized SERS active particles were then dried on the glass fiber pad at 45 °C for 1 hour. The glass fiber pad with particles was then cut into 4 mm × 4 mm squares.

An evaporation test was developed to evaluate the effect of the sealing film to reduce evaporation. To estimate the evaporation from the μPADs without and with a sealing film during flow, the μPAD was saturated with water and its mass change over time was monitored on a balance. By subtracting the mass of the original (dry) device, the mass lost from evaporation of the water (% mass loss) can be calculated with time, as shown in Figure B3. The mass loss in the μPADs with a sealing film is much lower than

in the μPADs without a sealing film, which confirms the effect of the sealing film to reduce evaporation.

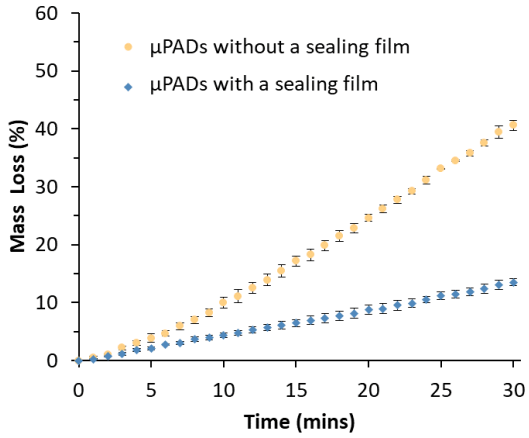

Figure B3. Comparison of evaporation of water from the μPADs without and with a sealing film. The measurements were taken after loading 50 μL of water in the inlet of the μPADs in a mass balance.

Dissolution of the material and fluid wicking are the main processes that occur when a fluid wicks through a paper with a dissolvable material. These processes are different for Region 1 (before the delay), Region 2 (the dissolvable delay), and Region 3 (after the delay). The process of a fluid wicking through a paper can be described using a Lucas-Washburn model [190], which assumes the porous media is a bundle of parallel capillary tubes and the transformed equation can be written as:

Equation 1

$$t = \frac{L^2 \cdot 2\eta}{\gamma \cdot cos\theta \cdot r}$$

where t is time, L is the length the fluid penetrated, γ is the fluid surface tension, θ is the contact angel, r is the radius for a cylindrical pore, and η is the fluidic dynamic viscosity. The radius for a cylindrical pore in Lucas-Washburn equation should not be simply interpreted as the pore size of a porous paper [190]. Instead, cylindrical pore radius is a parameter affected by pore size, porosity, and pore shape of the paper. According to Equation 1, fluid will have a longer flow time and a slower flow rate at a further position down the channel and thus, a longer Region 1 leads to a slower flow rate at the beginning of Region 2.

In Region 2, both dissolution of sugar and fluid wicking are happening. Dissolution of a dissolvable material can be described using the Nernst–Brunner equation [273],

Equation 2

$$\frac{dM}{dt} = \frac{A(t) \cdot D}{\delta}(c_s - c_b)$$

where M is the total mass dissolved, A denotes the total exposed surface area at time t, D is the diffusion coefficient of the dissolved molecule in the solvent, δ is the thickness of liquid unstirred boundary layer, c_s is the saturation solubility of the sugar, and c_b is the mass concentration of dissolved sugar in the fluid. Generally, δ can be decreased with an agitation. Although no exterior agitation is used, a turbulent flow can form when the flow comes in contact with the dissolvable material. A fast flow rate can cause a strong

agitation. Based on Equation 1, the flow rate near the inlet is faster than at the end. Thus, the position of the localized dissolvable delay (length of Region 1) affects the dissolution speed of the sugar. Fluid viscosity is reported to be the main factor contributing to the time delay when using a sucrose-based dissolvable delay [190]. Because surface flow is limited by the choke tape, the effect of sugar on the radius of the cylindrical pore in Region 2 also limits flow as the fluid largely wicks through the porous matrix of the paper. Notably, a faster dissolution speed of the sugar would cause both a larger increase in viscosity and a larger increase in the cylindrical pore in Region 2. These two parameters are tradeoffs since the viscosity and the cylindrical pore size have opposite effect on the flow time as noted in Equation 1.

In Region 3, after the dissolvable delay sugar region, fluid with dissolved sugar wicks in the blank paper. The fluid viscosity is determined by the amount of sugar dissolved in Region 2. Thus, compared with Region 1, Region 3 has an increased viscosity η which will cause a longer flow time.

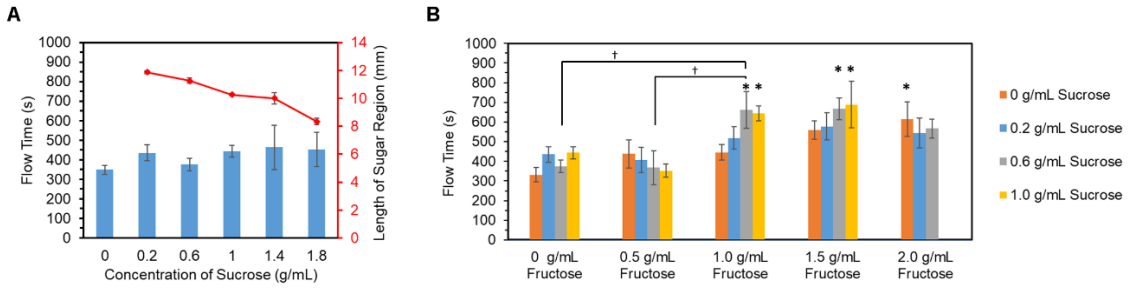

Figure B4. (a) The column data is the flow time of the fluid front to reach 40 mm on the paper with localized dissolvable delays made with 3 µL of different concentrations of sucrose, and the scatter data is the length of the sugar region using these sucrose solutions. (b) Comparison of flow time of the fluid front to reach 40 mm on the paper with localized dissolvable delays made of 3 µL of different concentrations of sucrose with different concentrations of fructose. All the localized dissolvable delays were located at the 10 mm position from the inlet. *Significantly different compared with µPAD without delay ($p < 0.05$); †Significantly different compared with delays made of different sugar solutions ($p < 0.05$).

We initially used sucrose solution to form the localized dissolvable delay and tested our flow time delay by measuring the time the fluid front reached the 40 mm location. As shown in Figure B4(a), the flow time in µPAD with localized delays made of sucrose was shorter than 500 s, and the delay wasn't increased effectively by increasing the concentration of sucrose. Compared with a flow time of 348 s in the µPAD without sucrose, the localized delay made of sucrose didn't effectively slow down the fluid. This indicates sucrose solution couldn't form an effective localized delay using the one-step dropping method. When limited volume of sucrose solution was dropped on the paper, the sucrose solution would quickly spread out in the paper and the dried sucrose would form a crystalline structure, leaving most pores vacant in the paper. An SEM image of the paper with dried sucrose is shown in a Figure B5(b). Fluid could flow through the pores

and the time to dissolve the sucrose was short. Thus, the fluid was not effectively hindered in the delay region possibly due to both large cylindrical pore radius and low viscosity.

Fructose and mixtures of fructose and sucrose were evaluated for their performance in providing a localized dissolvable delay. As shown in Figure B4(b), the flow time in the μPAD with dissolvable delays made of only fructose increased with the concentration of fructose used in making the delay. When the concentration of fructose was 1.5 g/mL, the flow time reached 560 s. The longer flow time using fructose and the monotonic increase compared to sucrose could be caused, in part, by the slower formation of crystals of fructose and better penetration in the paper pores of fructose, thereby filling the pores more completely than sucrose. Figure B4(b) also shows the flow time in the μPAD with dissolvable delays made of mixtures of different concentrations of fructose and sucrose. It shows that the sucrose/fructose mixture had a longer flow time than only fructose when fructose concentration was 1.0 g/mL and 1.5 g/mL. The longer flow times of the sucrose/fructose mixtures could be attributed to the slower speed in forming sucrose crystals and more of the sucrose/fructose mixture filling in the pores (Figure B5(c)). More effectively filled pores possibly decreased the cylindrical pore radius, which increased flow time and decreased flow rate. Moreover, the slow flow increased the interaction time of the fluid to improve sugar dissolution. As the sugar was effectively dissolved and both fructose and sucrose increased fluid viscosity after they were dissolved, the fluid was effectively slowed down due to the high viscosity. The flow time in channels with 0.6 g/mL or 1 g/mL sucrose and 1.0 g/mL fructose, 0.6 g/mL or 1 g/mL sucrose and 1.5 g/mL fructose, and 0 g/mL sucrose with 2.0 g/mL fructose were all significantly different from

the flow time in a blank channel as indicated by the * in Figure B4(b). Among these five combinations that maximized flow time, the 0.6 g/mL sucrose with 1.0 g/mL fructose was used in future experiments because it consumed less sugar material and was less viscous, which made it easier to make on the paper. It also provided a flow time of 661 s, close to 2 times the flow time in a μPAD without a dissolvable delay.

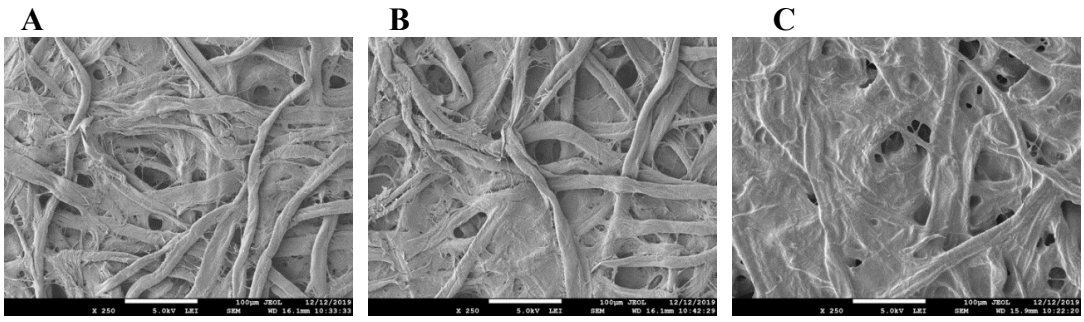

Figure B5. SEM images. Whatman grade 1 chromatography paper (a) without any sugar, (b) with 0.6 g/mL sucrose, and (c) with 0.6 g/mL sucrose and 1.0 g/mL fructose. The scale bar indicates 100 μm.

The total particle count at the 10 mm test line position was characterized using fluorescent particles. Initially, 50 μL of water with fluorescent particles was loaded in the μPADs with a localized dissolvable delay made of 2.5 μL of 0.6 g/mL sucrose with 1.0 g/mL fructose at 15 mm. To measure the total particle count, 5 s videos were taken from a fluorescent microscope at 300 s, 600 s, 900 s, 1200 s, 1440 s, and 1680 s, after loading the fluorescent particle solution. The same tests were done in μPADs without the localized

dissovable delay. Movements of the 1.1 μm fluorescent particles at 10 mm past the inlet of the μPAD were tracked using a program developed in a previous study [262, 263]. Particle counts were obtained by adding up all moving particles tracked in all frames of the 5 s video. As shown in Figure B6, to achieve a total particle count of 1300, it took around 900 s for a blank μPAD and around 1650 s for the μPAD with a delay. Because a longer time was needed in the μPAD with a delay for same number of particles to reach the test line, the reaction time between analytes and particles in the μPAD with a delay would be longer and hence allow for more time to interact.

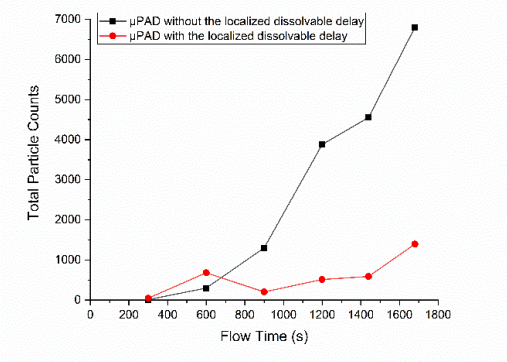

Figure B6. The total counts of fluorescent particles at 10 mm from 300 s to 1680 s in μPADs without and with a localized dissolvable delay. The localized dissolvable delay was made of 2.5 μL of 0.6 g/mL sucrose with 1.0 g/mL fructose located at 15 mm from the inlet. The particle counts were the total counts of moving particle tracked in all frames of a 5 s video.

Performance of the mechanical valve without a dissolvable delay was characterized. For the mechanical valve alone, 150 μL of the blue fluid (made by mixing

PBS with food color dye) was loaded in the washing solution storage area followed by loading 75 µL of the red fluid in the inlet of the µPADs. Movements of the two fluids were recorded using a webcam. The flow time to the specific positions was read from the recorded videos. Figure B7 shows the repeatability of the flow time in the µPAD with the mechanical valve. It can be observed that the design provided a consistent control in terms of the time to open the valve and initiate Step 2.

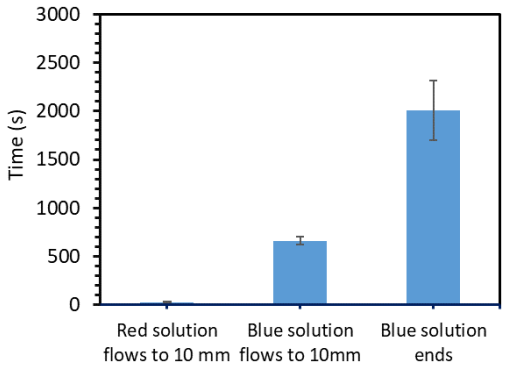

Figure B7. Repeatability of the flow time in the µPAD with a mechanical valve for a two-step process without a delay.

The immobilization of aptamer 1 on the test line was confirmed by imaging using a fluorescent microscope. Before imaging, the paper was reacted with a DNA strand with a complementary sequence to aptamer 1 and a fluorescein at the 5'- end. Specifically, an aptamer immobilized paper was incubated in a solution with 3 µL of 100 µM DNA-fluorescein and 50 µL of hybridization buffer (6× SSC) for 1 hour. After incubation, the

unbound DNA-fluorescein was washed off, and the paper was dried before imaging. As shown in Figure B8, a strong fluorescent intensity observed on the test line region compared with the rest of hydrophilic channel confirms the successful immobilization of aptamer 1 on the paper. The thickness of the test line was smaller than 1 mm.

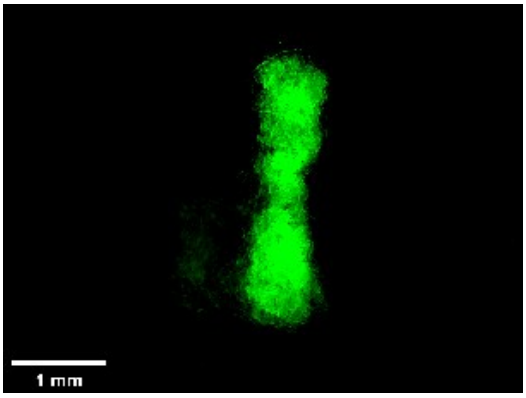

Figure B8. Image of a cellulose paper immobilized with aptamer 1. The image was taken using a fluorescent microscope.

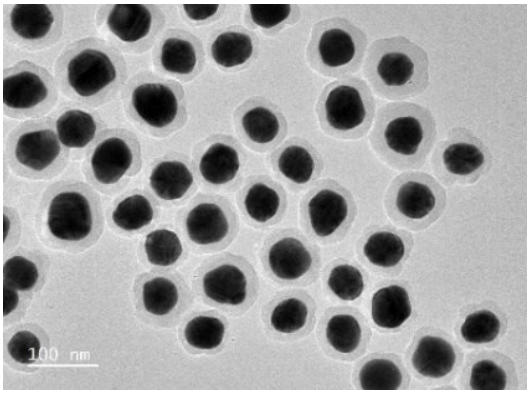

Figure B9. TEM images of synthesized silica shell SERS particles showing the nanoparticles and the silica shell encapsulation.

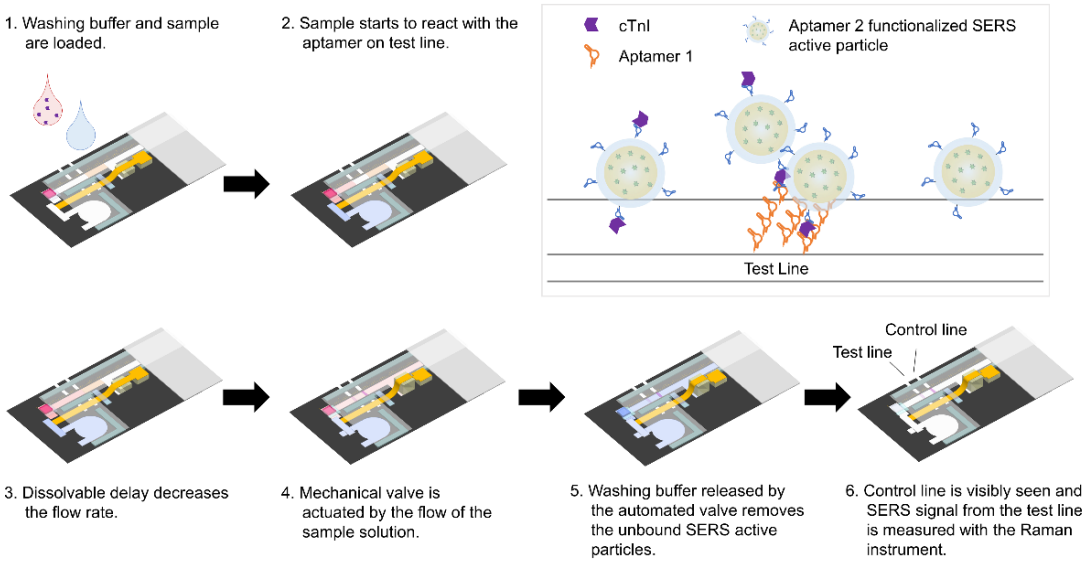

Figure B10. Schematic representation of the aptamer-based assay using the µPAD with a localized dissolvable delay and a mechanical valve.

The SERS spectra of the hydrophilic channel on the Whatman grade 1 chromatography paper with and without the SERS active particles were measured. The raw spectra were baseline corrected using *Baseline Estimation and Denoising with Sparsity* function in MATLAB (cut-off frequency of 0.006, filter order of 1, asymmetry parameter of 6). The baseline corrected spectra are shown in Figure B11. It is observed that 1168 cm^{-1}, 1584 cm^{-1}, and 1614 cm^{-1} are the characteristic peaks from the SERS active particles and, although the paper itself has Raman peaks, that at those wavenumbers the signal intensity is high compared to the background signal from the cellulose paper. In

terms of the peak assignments, 1168 cm^{-1} is assigned to in-plane benzene ν_9 mode, 1584 cm^{-1} is assigned to ring in-plane stretching and bending, and 1614 cm^{-1} is assigned to C–C and *N*-phenyl stretching [274].

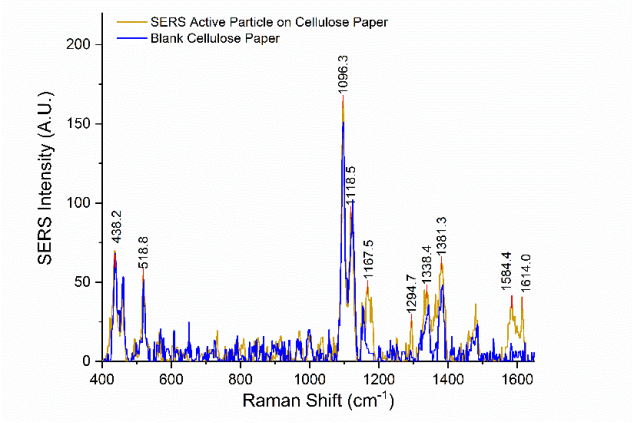

Figure B11. SERS spectra of a blank cellulose paper and a cellulose paper with the aptamer-functionalized SERS active particle.

(a)

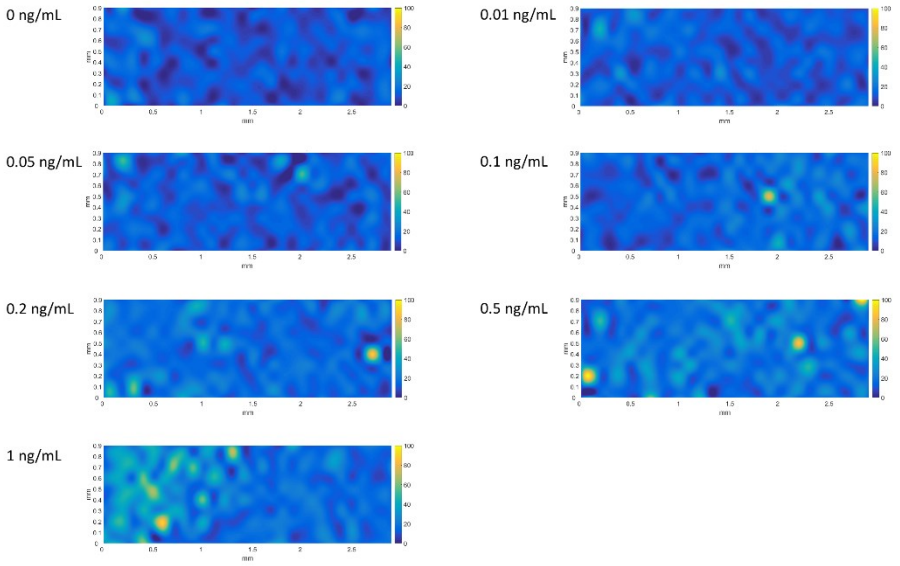

(b)

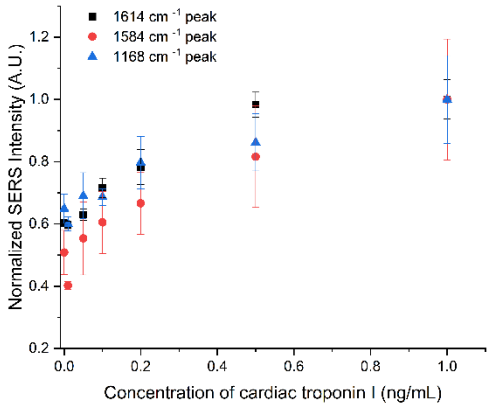

Figure B12. (a) SERS intensity maps of the test line on the μPADs after testing different concentrations of cTnI using peaks at 1614 cm^{-1}. To plot the maps, SERS spectra at different points covering the test line (10 × 30 points, 100 μm step size) were first measured. The SERS intensity at 1614 cm^{-1} for each grid point was used to plot the color maps. The color represents the value of the SERS intensity. (b) Comparison of SERS response on the test line of μPADs to different concentrations of cTnI using the different peaks.

The SERS intensity on the test line area was measured using the mapping function in the Thermo Scientific DXR Raman confocal microscope with a 780 nm laser. A 10 × 30 point array with a 100 μm step size was measured on the test line area. Each point was measured by excited with a 24 mW laser using 2 s exposure. All spectra were baseline corrected using the same method mentioned above. The peak intensities at 1168 cm^{-1}, 1584 cm^{-1}, and 1614 cm^{-1} were obtained by calculating the maximum values in the ranges of 1165 cm^{-1}-1185 cm^{-1}, 1574 cm^{-1}-1590 cm^{-1}, and 1610 cm^{-1}-1630 cm^{-1}, respectively. By using the peak intensity at a specific peak, the SERS intensity map could be drawn. Figure B12(a) shows the SERS intensity map of the test line on μPADs after testing different concentrations of cTnI using the peaks at 1614 cm^{-1}.

After adding up the SERS intensity at specific peaks from the 10 × 30 point array, the correlation between the SERS response on the test line of μPADs with the concentration of cTnI was plotted. As shown in Figure B12(b), the SERS response at 1168 cm^{-1}, 1584 cm^{-1}, and 1614 cm^{-1} increased with the concentration of the cTnI. The error bars are a bit high at 1584 cm^{-1}, indicating a low signal-to-noise ratio using this peak, but this could be improved with various signal and image processing approaches.

Assay response to different concentrations of cTnI using a μPAD with a localized dissolvable delay made of 2.5 μL of 0.6 g/mL sucrose and 1.0 g/mL fructose located at 15 mm from the inlet was compared to the response using a μPAD without a dissolvable delay. As shown in Figure B13, the assay using μPADs with the localized dissolvable delay shows a better sensitivity in the low concentration range than the assay using blank μPADs. In addition, the assay using μPADs with a dissolvable delay also reached a plateau

at 0.5 ng/mL compared to the assay using blank µPADs. This indicates the assay saturated at a lower concentration, which may be caused by more cTnI protein bound to the aptamers and more particles captured due to longer sample reaction time.

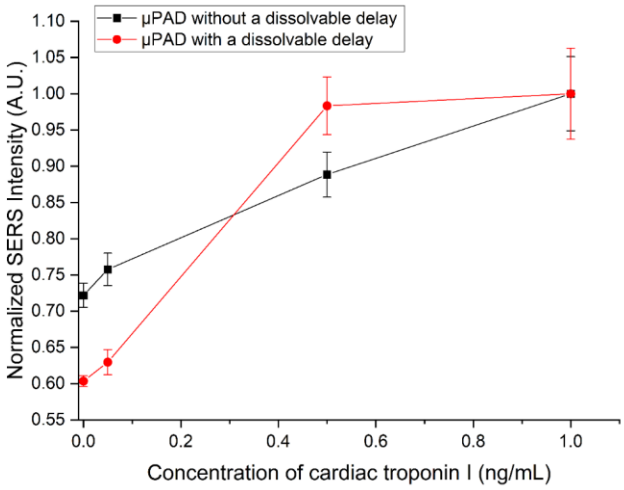

Figure B13. Comparison of the assay response to different concentrations of cTnI using a µPAD without a dissolvable delay and a µPAD with a localized dissolvable delay made of 2.5 µL of 0.6 g/mL sucrose and 1.0 g/mL fructose located at 15 mm from the inlet.

Flow time of the µPADs for cTnI assay when using a µPAD with and without a dissolvable delay was also compared. In this test, both µPADs were functionalized with aptamers and had a glass fiber pad with aptamer-functionalized SERS active particles. The µPAD with a dissolvable delay had a delay region made of 2.5 µL of 0.6 g/mL sucrose with 1.0 g/mL fructose and was located at 15 mm from the inlet. The flow time was

recorded, after 150 µL of washing buffer (PBS with 0.25% Tween 20) was loaded in the washing solution storage area, followed by loading 75 µL of sample solution (PBS with cTnI) in the inlet of the µPADs. As depicted in Figure B14, the flow time was fairly repeatable for both configurations. The dissolvable delay caused a more than 2 times increase in the flow time for the sample to reach 25 mm (end of the dissolvable delay region). In addition, the dissolvable delay postponed the time to start Step 2 (flowing the washing buffer).

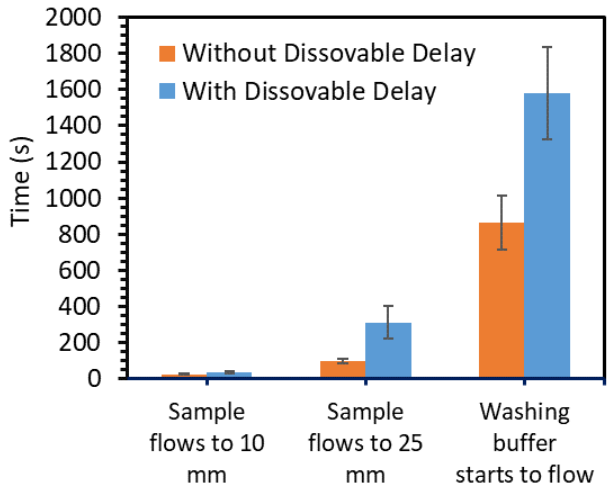

Figure B14. Comparison of the flow time of the µPADs for a cTnI assay when using a µPAD without a dissolvable delay and a µPAD with a localized dissolvable delay made of 2.5 µL of 0.6 g/mL sucrose and 1.0 g/mL fructose at a distance of 15 mm from the inlet.

APPENDIX C

SUPPORTING INFORMATION FOR SPECTRALLY MULTIPLEXED ASSAY USING GAP ENHANCED NANOPARTICLE FOR DETECTION OF A MYOCARDIAL INFARCTION BIOMARKER PANEL

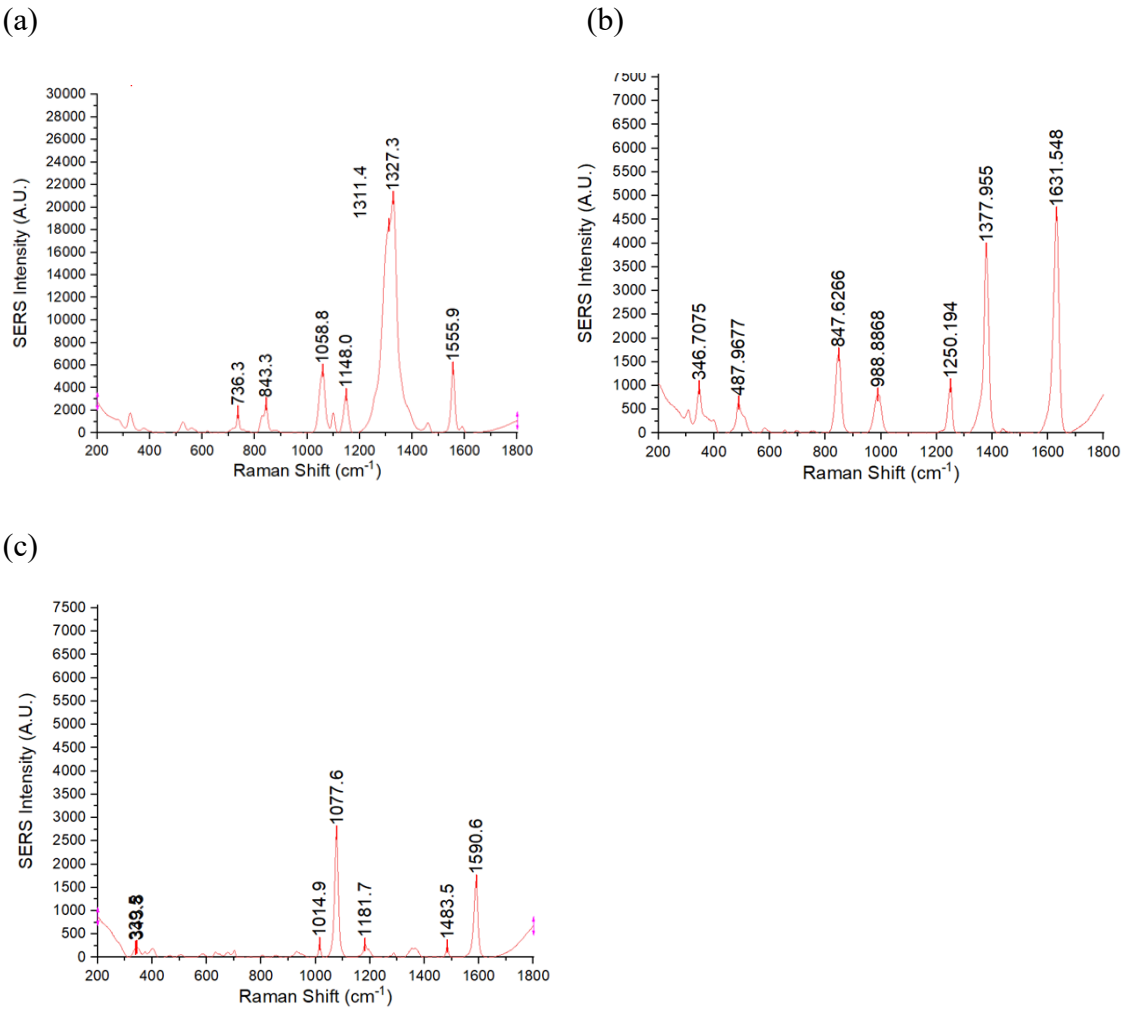

Figure C1. SERS spectra of the synthesized (a) Au_{core}/DTNB/Au_{shell}, (b) Au_{core}/TFMBA/Au_{shell}, and (c) Au_{core}/MPAA/Au_{shell} gap-enhanced nanoparticles. The spectra have been baseline corrected.

Table C1. Assignment of vibrational modes of DTNB, TFMBA, and MPAA, to the SERS spectrum of the gap-enhanced nanoparticles.

Raman Reporter	Peak (cm^{-1})	Assignment	Reference
DTNB	843	Nitro scissoring vibration	[275]
	1059	Succinimidyl N–C–O stretch overlapping with aromatic ring modes	[275, 276]
	1148	C-H bending	[277, 278]
	1327	Symmetric stretch of the N–O nitro group	[275, 279, 280]
	1556	Aromatic ring stretching	[275, 280]
TFMBA	848	Aromatic ring breathing	[281, 282]
	989	Ring breathing	[283]
	1250	C-H bending	[284-286]
	1378	C-H bending and C-C stretching	[286-288]
	1632	C-C stretching	[286, 289, 290]
MPAA	1078	ν_{12} aromatic ring vibration	[133, 291]
	1591	ν_{8a} aromatic ring vibration	[133, 291]

(a)

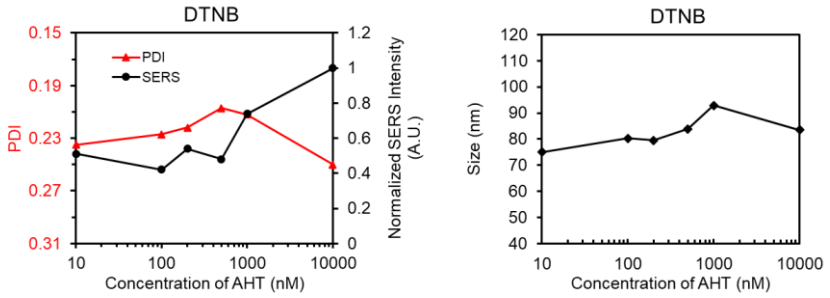

(b)

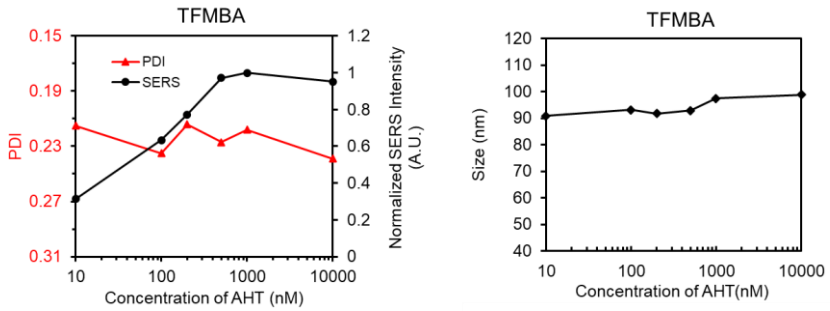

(c)

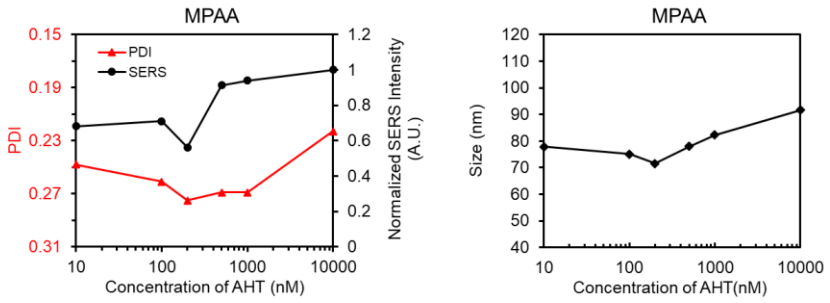

Figure C2. Optimization of the amount of AHT in synthesis of (a) Au_{core}/DTNB/Au_{shell}, (b) Au_{core}/TFMBA/Au_{shell}, and (c) Au_{core}/MPAA/Au_{shell} gap-enhanced nanoparticles. The SERS signal was obtained using 780 nm laser, 24mW, 1 s exposure time, 5 exposures. The SERS intensity of Au_{core}/DTNB/Au_{shell} is from the peak at 1148 cm^{-1}, SERS intensity of Au_{core}/TFMBA/Au_{shell} is from the peak at 1632 cm^{-1}, and SERS intensity of Au_{core}/MPAA/Au_{shell} is from the peak at 1591 cm^{-1}. The polydispersity index (PDI) and size value are from DLS data.

The amount of 6-AHT added affects the formation of the gold shell. A set of experiments were used to determine the optimal amount of 6-AHT to form a gap enhanced particle with good size distribution and a good SERS signal. The polydispersity index (PDI) was used to evaluate the particle size distribution. The amount of 6-AHT used to synthesize Au_{core}/DTNB/Au_{shell}, Au_{core}/TFMBA/Au_{shell}, and Au_{core}/MPAA/Au_{shell} gap enhanced particles were optimized, respectively.

As shown in Figure C2(a), Au_{core}/DTNB/Au_{shell} gap-enhanced particle size increases with 6-AHT from 10 nM to 1000 nM, indicating a better formation of the gold shell when more 6-AHT is present in this range. In addition, the SERS signal increases with the increase of 6-AHT, and thus a high 6-AHT concentration is favored to achieve a significant SERS signal. However, the PDI value of 10000 nM 6-AHT is the highest. This may be because the large amount of 6-AHT attached to the gold core decreases its stability, which causes aggregation before forming gold shells. In addition, the excess 6-AHT may form multiple layers of 6-AHT on the surface of Au_{core}, which decreases the number of free thiol groups and prevents the growth of the gold shell. This mixture of the Au_{core}, Au_{core}/DTNB/Au_{shell}, and the aggregated particles leads to a broader particle distribution. To achieve a high SERS signal and keep the uniformity of the particle size, 1000 nM of 6-AHT is determined to be the optimal amount for the synthesis of Au_{core}/DTNB/Au_{shell} particle.

As shown in Figure C2(b), Au_{core}/TFMBA/Au_{shell} gap-enhanced particle size slightly increases with 6-AHT. The SERS signal increases with 6-AHT from 10 nM to 500 nM and stops growing after 500 nM of 6-AHT. Thus, 500 to 10000 nM of 6-AHT are

similarly good for SERS signal. The PDI value of the particle using 1000 nM 6-AHT is the lowest among 500 nM, 1000 nM, and 10000 nM of 6-AHT. Therefore, to achieve a high SERS signal and keep the particle size uniformity, 1000 nM 6-AHT is selected for Au_{core}/TFMBA/Au_{shell} particle.

As shown in Figure C2(c), Au_{core}/MPAA/Au_{shell} gap-enhanced particle size increases with 6-AHT when 6-AHT increases from 200 nM to 10000 nM. The SERS signal increases with 6-AHT from 200 nM to 10000 nM. In addition, the PDI value of 10000 nM 6-AHT is the smallest. Therefore, to achieve a high SERS signal and keep the uniformity of the particle size, 10000 nM 6-AHT is selected for Au_{core}/MPAA/Au_{shell} particle.

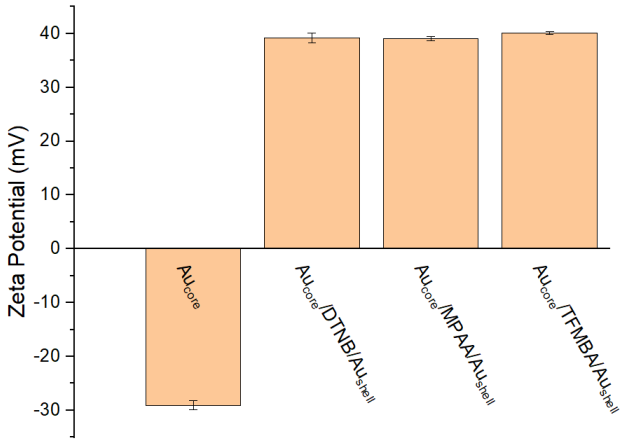

Figure C3. Zeta potential of the synthesized Au_{core} nanoparticle, Au_{core}/DTNB/Au_{shell} GeNP, Au_{core}/MPAA/Au_{shell} GeNP, and Au_{core}/TFMBA/Au_{shell} GeNP.

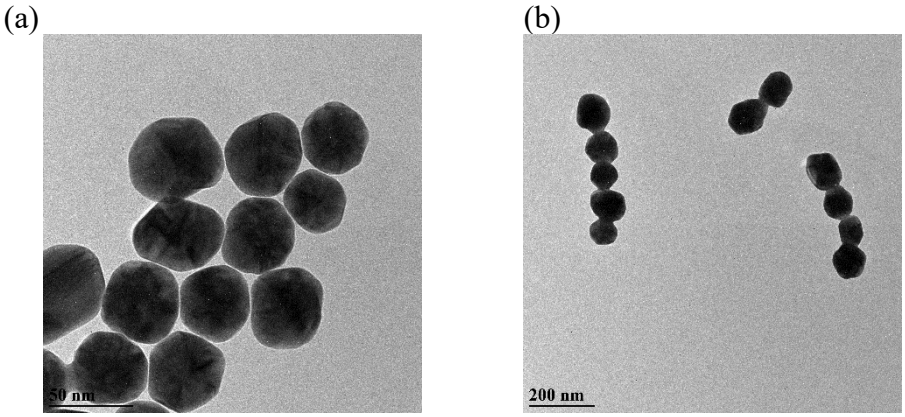

Figure C4. TEM image of (a) the synthesized gold core and (b) the around 99 nm gold nanoparticle.

To synthesize gold core nanoparticle (Au_{core}), the following procedures are used. Sodium citrate solution (75 mL, 2.2 mM) was heated until boiled. After the solution was boiled, $HAuCl_4$ solution (0.5 mL, 25 mM) was injected and the mixture was allowed to stir for 30 min. The temperature was then adjusted to 90 ℃. After confirming the solution temperature reached 90 ℃, $HAuCl_4$ solution (0.5 mL, 25 mM) was injected and the mixture was allowed to stir for 30 min. Another $HAuCl_4$ solution (0.5 mL, 25 mM) was then injected and the mixture was allowed to stir for 30 min. Next, the particle solution was diluted by extracting 27.5 mL of solution and adding the same volume of sodium citrate solution (2.2 mM). After confirming the solution temperature reached 90 ℃, $HAuCl_4$ solution (0.5 mL of 25 mM) was injected the mixture was allowed to stir for 30 min. Lastly, the nanoparticle solution was allowed to cool to room temperature.

(a)

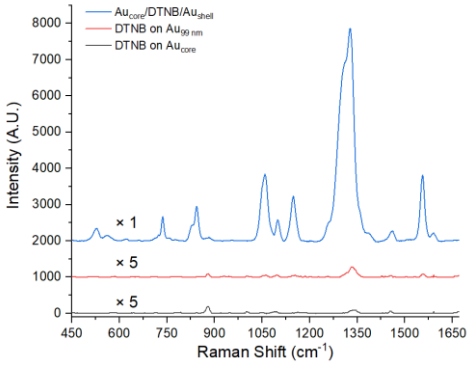

(b)

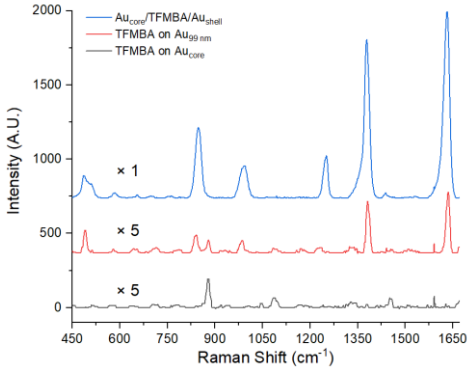

(c)

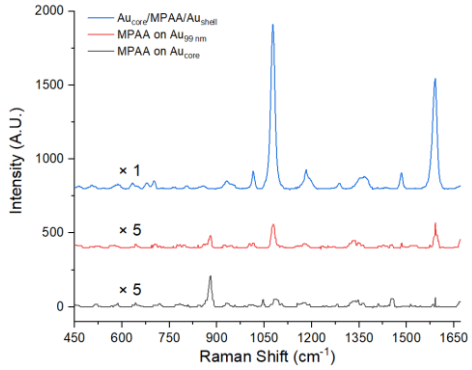

Figure C5. (a) Comparison of SERS spectra of Au$_{core}$/DTNB, Au$_{99nm}$/DTNB, and Au$_{core}$/DTNB/Au$_{shell}$ GeNP. (b) Comparison of SERS spectra of Au$_{core}$/TFMBA, Au$_{99nm}$/TFMBA, and Au$_{core}$/TFMBA/Au$_{shell}$ GeNP. (c) Comparison of SERS spectra of Au$_{core}$/MPAA, Au$_{99nm}$/MPAA, and Au$_{core}$/MPAA/Au$_{shell}$ GeNP. The SERS signal was obtained using a 780 nm laser, 24mW, 2 s exposure time, 3 exposures. The stock concentrations of the particles were determined using Nanosight Nanoparticle Tracking Analysis (NTA). To prepare the Au$_{core}$/RRM and Au$_{99nm}$/RRM, the Au$_{core}$ and Au$_{99nm}$ were diluted to be 90 pM, then added 25 µL of 10mM RRM. The mixtures were then shaken overnight before measuring their SERS signal. The Au$_{core}$/RRM/Au$_{shell}$ GeNPs were diluted to be 90 pM before measuring their SERS signal. The SERS spectra of the Au$_{core}$/DTNB and Au$_{99nm}$/DTNB were multiplied by 5 to show their peaks clearly.

The SERS signal of the Au_{core}/RRM/Au_{shell} GeNP was compared with the Au_{core}/RRM to evaluate the SERS enhancement after growing a gold shell. We also compared the GeNPs with a solid spherical particle similar to the GeNPs (a 99 nm gold nanoparticle) to evaluate the improvement of the core-gap-shell nanostructure.

Figure C5(a) shows the SERS spectra of Au_{core}/DTNB, Au_{99nm}/DTNB, and Au_{core}/DTNB/Au_{shell}. It indicates that the SERS signal of the Au_{99nm}/DTNB is slightly larger than Au_{core}/DTNB, except the peak at around 883 cm^{-1}. When preparing Au_{core}/DTNB and Au_{99nm}/DTNB, 25 μL of 10mM DTNB dissolved in ethanol was added into the particle. Because the mixture contains ethanol, some ethanol molecules adsorb on the surface of Au_{core} and Au_{99nm}. Due to this, the SERS spectra showed characteristic ethanol peaks at around 883 cm^{-1}, 1048 cm^{-1}, 1092 cm^{-1}, and 1450 cm^{-1} [292]. In addition, Au_{99nm}/DTNB showed a lower ethanol peak than Au_{core}/DTNB, possibly due to less favored ethanol adsorption on Au_{99nm} than on Au_{core}. Based on Figure C5(a) and the calculation shown below, the Au_{core}/DTNB/Au_{shell} has a much larger SERS intensity than the signal of Au_{core}/DTNB (120 times) and the signal of Au_{99nm}/DTNB (212 times).

Using the peak intensity at 1148 cm^{-1},

signal ratio of Au_{core}/DTNB/Au_{shell} to Au_{core}/DTNB = 1231.74/5.81 = 212

signal ratio of Au_{core}/DTNB/Au_{shell} to Au_{99nm}/DTNB = 1231.74/10.28=119.86

Figure C5(b) shows the SERS spectra of Au_{core}/TFMBA, Au_{99nm}/TFMBA, and Au_{core}/TFMBA/Au_{shell}. In the SERS spectrum of Au_{core}/TFMBA, the characteristic peaks from TFMBA were very low, and only the distinct peaks from ethanol were visible. In contrast, the Au_{99nm}/TFMBA showed clear peaks from TFMBA. Similar to particles with

DTNB, the ethanol peaks on Au_{99nm}/TFMBA were lower than the ethanol peaks on Au_{core}/TFMBA, possibly due to less favored ethanol adsorption on Au_{99nm} than on Au_{core}. Based on Figure C5(b) and the calculation shown below, the Au_{core}/TFMBA/Au_{shell} has a much larger SERS intensity than the signal of Au_{core}/TFMBA (254 times) and the signal of Au_{99nm}/TFMBA (15 times).

Using the peak intensity at 1632 cm^{-1},

signal ratio of Au_{core}/TFMBA/Au_{shell} to Au_{core}/TFMBA = 1253.56/4.94 = 253.79

signal ratio of Au_{core}/TFMBA/Au_{shell} to Au_{99nm}/TFMBA = 1253.56/81.11=15.45

Figure C5(c) shows the SERS spectra of Au_{core}/MPAA, Au_{99nm}/MPAA, and Au_{core}/MPAA/Au_{shell}. Similarly, the ethanol peaks on Au_{99nm}/MPAA were lower than the ethanol peaks on Au_{core}/MPAA, possibly due to less favored adsorption of ethanol on Au_{99nm} than on Au_{core}. It also shows that the SERS signal of the Au_{99nm}/MPAA is much larger than Au_{core}/MPAA. In addition, the Au_{core}/MPAA/Au_{shell} has a much larger SERS intensity than the signal of Au_{core}/MPAA (106 times) and the signal of Au_{99nm}/MPAA (35 times).

Using the peak intensity at 1078 cm^{-1},

signal ratio of Au_{core}/MPAA/Au_{shell} to Au_{core}/MPAA = 1110.69/10.49 = 105.84

signal ratio of Au_{core}/MPAA/Au_{shell} to Au_{99nm}/MPAA = 1110.69/31.29= 35.49

Notably, in synthesizing GeNPs, 25 μL of 10 mM RRM was added to incubate with the Au_{core} and then centrifuged to wash the excess RRM. Because of this, the actual RRM inside the gap of the Au_{core}/RRM/Au_{shell} GeNP should be much smaller than the added amount. Thus, the signal ratio of Au_{core}/RRM/Au_{shell} to Au_{core}/RRM or Au_{99nm}/RRM

should be larger than the values calculated above if controlling the attached amount of RRM to be the same. Despite this, the obtained result confirmed that a significant SERS enhancement could be achieved after growing the gold shell. Although increasing particle size can increase electromagnetic field and increase SERS intensity [100], using the gap inside the GeNP is more efficient in enhancing the SERS signal than the increasing size of a solid spherical particle.

Table C2. Calibration curves of Au_{core}/DTNB/Au_{shell} GeNP using 1148 cm^{-1} peak, 1327 cm^{-1} peak, and 1556 cm^{-1} peak.

Peak (cm^{-1})	Calibration curve	R^2
1148	y = 10.1x + 115.95	R^2 = 0.9844
1327	y = 52.468x + 446.87	R^2 = 0.9740
1556	y = 16.164x + 152.52	R^2 = 0.9836

Table C3. Calibration curves of Au_{core}/TFMBA/Au_{shell} GeNP using 989 cm^{-1} peak, 1378 cm^{-1} peak and 1632 cm^{-1} peak.

Peak (cm^{-1})	Calibration curve	R^2
989	y = 1.8056x + 25.206	R^2 = 0.989
1378	y = 8.53x + 124.70	R^2 = 0.9898
1632	y = 10.138x + 146.75	R^2 = 0.9899

The 1148 cm^{-1} peak, 1327 cm^{-1} peak, and 1556 cm^{-1} peak of DTNB displayed minimal overlap with the peaks from the other two RRMs. The 989 cm^{-1} peak, 1378 cm^{-1} peak, and 1632 cm^{-1} peak of TFMBA had least overlap with the peaks from the other two RRMs. Due to the GeNPs being uniformly distributed there was no aggregation induced SERS enhancement, therefore the SERS intensity should be linearly proportional to the concentration of the GeNPs measured.[108] The calibration curves of Au_{core}/DTNB/Au_{shell} GeNP using different peaks were compared in Table C2. The 1556 cm^{-1} peak displayed good linearity (R^2 = 0.9836) comparative to 1148 cm^{-1} (R^2 = 0.9844) but had a greater slope, therefore it was used in further analyses. In addition, the calibration curves of Au_{core}/TFMBA/Au_{shell} GeNP using different peaks were compared in Table C3. Because the 1632 cm^{-1} peak had a higher intensity than the 989 cm^{-1} peak and the 1378 cm^{-1} peak and all three peaks had similar linearity, the 1632 cm^{-1} peak of TFMBA was selected.

(a)

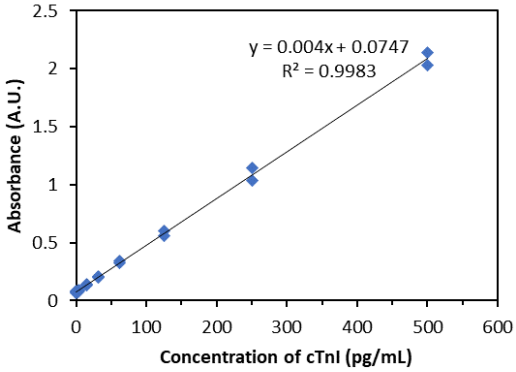

(b)

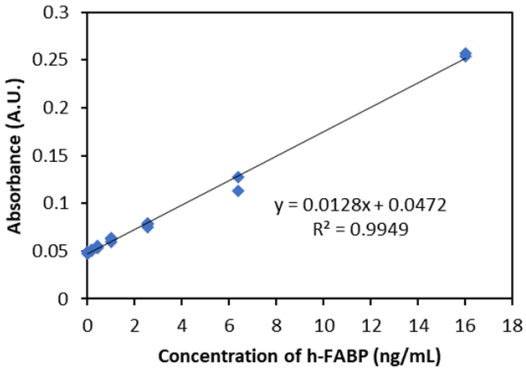

(c)

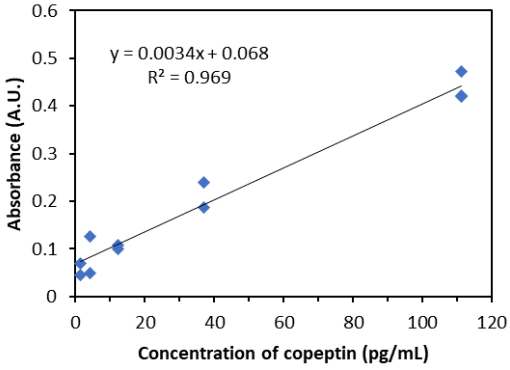

Figure C6. Calibration curves of the ELISA kits were used to calculate the concentration of the (a) cTnI, (b) h-FABP, and (c) copeptin in the human serum.

(a)

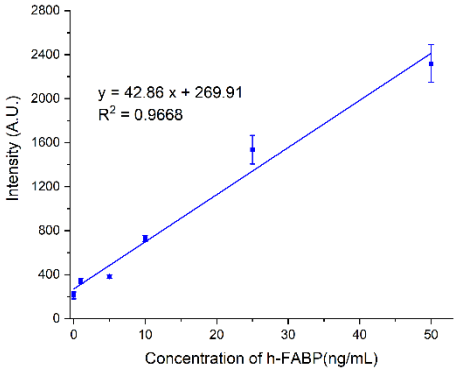

(b)

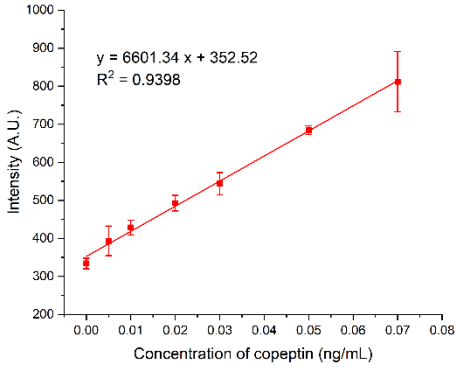

(c)

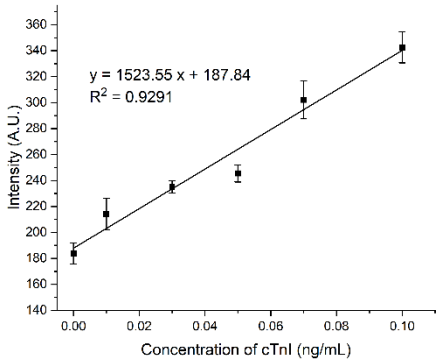

Figure C7. Response curve to different concentrations of (a) h-FABP, (b) copeptin, and (c) cTnI, respectively, in PBS buffer.

Table C4. Paired t-test of the SERS signals from multiplex detection of mixtures and the signals from single-biomarker detection.

Concentration of biomarker in sample	Paired t-test for equality of means of multiplex detection and single-biomarker detection		
	t Statistics	p-value	Significance*
0.007 ng/mL copeptin	1.503	0.272	Not significantly different
0.037 ng/mL copeptin	-1.147	0.370	Not significantly different
0.057 ng/mL copeptin	-1.012	0.418	Not significantly different
2.3 ng/mL h-FABP	1.609	0.249	Not significantly different
12.3 ng/mL h-FABP	-1.347	0.310	Not significantly different
27.3 ng/mL h-FABP	-1.066	0.398	Not significantly different
0 ng/mL cTnI	-1.469	0.280	Not significantly different
0.07 ng/mL cTnI	-2.506	0.129	Not significantly different
0.1 ng/mL cTnI	0.685	0.564	Not significantly different

* 0.05 significance level. p-values <0.05 were considered statistically significant.

Paired t-test was used to evaluate the means of the SERS signals from the multiplex detection of mixtures and the SERS signals from the single-biomarker detection. As shown in Table C4, the t-test results indicate that the means of SERS signal in the two detection settings are not significantly different at 0.05 significance level.

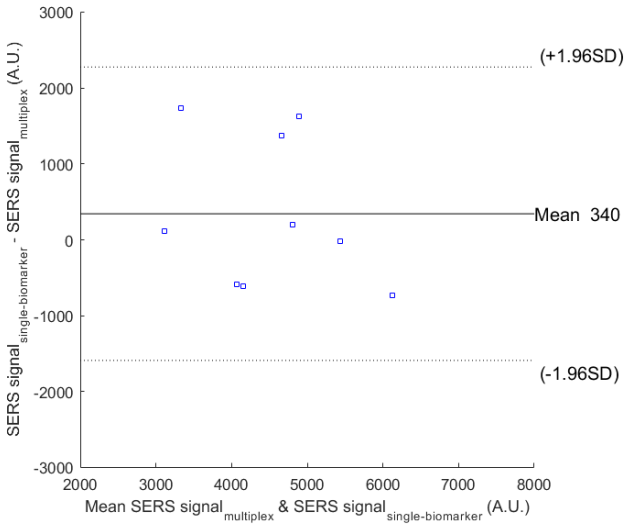

Figure C8. Bland-Altman plot describing the agreement between multiplex detection and single-biomarker detection of copeptin. The ±1.96 SD lines represent limits of agreement in 95% confidence interval.

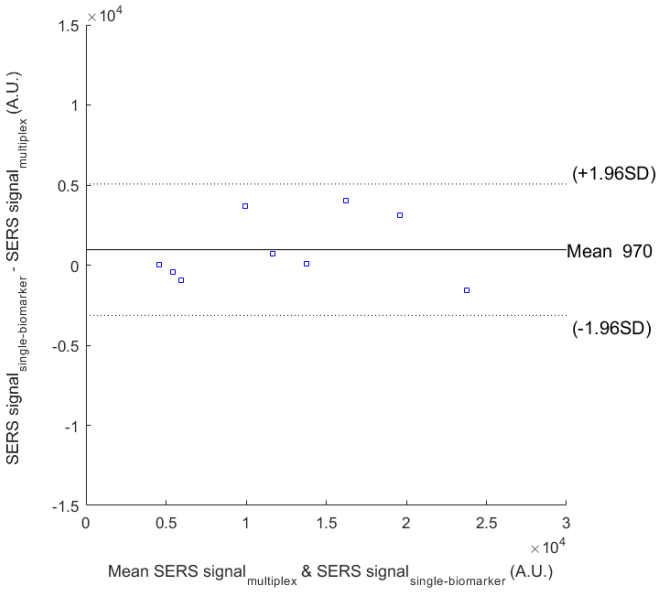

Figure C9. Bland-Altman plot describing the agreement between multiplex detection and single-biomarker detection of h-FABP. The ±1.96 SD lines represent limits of agreement in 95% confidence interval.

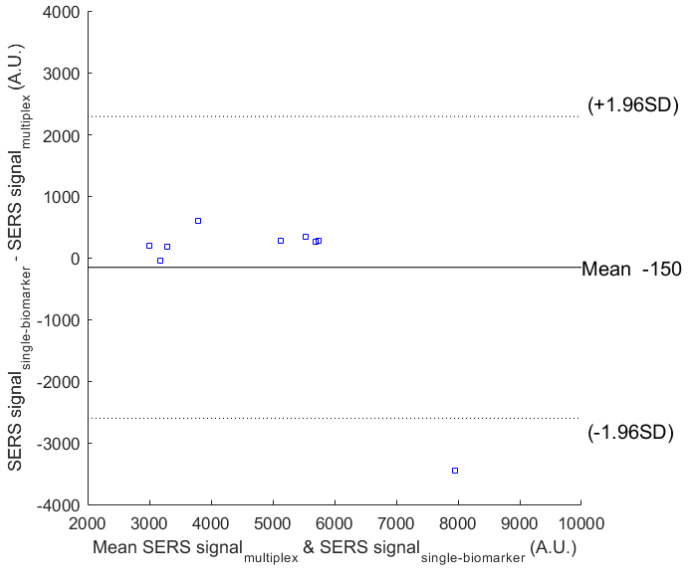

Figure C10. Bland-Altman plot describing the agreement between multiplex detection and single-biomarker detection of cTnI. The ±1.96 SD lines represent limits of agreement in 95% confidence interval.

Bland-Altman plots are generally used to evaluate the agreement of two detection methods [293-295]. Here, Bland-Altman plots (Figure C8-C10) were generated to evaluate the agreement of the SERS signal from the multiplex detection of mixtures and the signals from the single-biomarker detection. In the plots, the ±1.96 SD lines represent limits of agreement in 95% confidence interval. In Figure C8 and Figure C9, all the data points lied inside the limits, which indicates a good agreement between the multiplex detection and single-biomarker detection for copeptin and h-FABP. In Figure C10, one data point fell out of the limits, which was from the data points for 0.1 ng/mL cTnI that showed a large standard deviation in Figure 4.7(b). The rest data points in Figure C10 fell

within the limits, which confirms the good agreement between the multiplex detection and single-biomarker detection for cTnI.